Spin-orbit Torque Driven Magnetization Switching for Non-volatile Memory and Beyond

Submitted in the partial fulfillment of the requirements for

the degree of

Doctor of Philosophy

in

Materials Science & Engineering

Yang Liu

B.Eng., Metallurgical Engineering, University of Science & Technology Beijing
M.S., Materials Science & Engineering, Carnegie Mellon University

Carnegie Mellon University
Pittsburgh, PA

May, 2020

© Yang Liu, 2020
All Right Reserved

Acknowledgements

This research work was funded by the industrial sponsors through the Data Storage Systems Center (DSSC) at Carnegie Mellon University. I'd like to thank the sponsors for their financial support.

I thank my advisor Prof. Jimmy Zhu for his continuous support for both my research and PhD life over the last five years. I benefit a lot from his wisdom and patient guidance. I am grateful that he always gives me the opportunity to explore the research topics I am interested in. And his advice points out the right direction that I should go for. More importantly, the research training and experience under his guidance let me know how to face challenges and come up with solutions to solve them, which is a necessity for becoming an independent researcher.

I also thank my committee members: Prof. David Laughlin, who provides me rich insights in the field of materials science and introduced me into the doctoral program at CMU, Prof. Vincent Sokalski who is a young and promising professor and from whom I learned lots of new physics in spintronics, and Dr. Daniel Worledge who is generous to provide efforts for enhancing my research work.

I also wish to thank my colleague as well as friend Bing Zhou for the fruitful discussions in various research projects. Working with him has been so much fun. I thank the senior researchers in our group: Vara and Masaki (now at Western Digital). They taught me many tricks in improving the experimental methods, which can never be learned from books. I thank Zhengkun Dai (now at Apple) for his help on designing and constructing all the complicated testing equipment. I thank Yuwei Qin for the discussions in magnetism theories and simulations. It was enjoyable to share the experience in raising the lovely cats with him and his girlfriend Tong Mo. I also wish the two new and smart PhD students, Enbo Zhang and Boyuan Yang, to enjoy their PhD life and output

good research results. It was also a nice experience to work with the other lab mates: Xiao Lu, Xi Liu and Abir Shadman.

I take this opportunity to thank the staff members at DSSC and Nanofab. I thank Chloe Mattingly and Pat Grieco for the arrangements of the conference traveling and the room reservations, and Andrew Gamble for the equipment installation and maintenance. All of them work hard to ensure that every year's DSSC reviews run smoothly. I pay special thanks to Matt Moneck, the executive director of the cleanroom. He is an absolute expert in both nanofabrication and research tools. And he is always there to offer help when I encounter problems in device fabrication. I also thank the other two cleanroom staff: Norm Gottron and Mason Risley, both of who make sure the tools are ready for use.

At last, I would like to thank my parents and girlfriend for their unconditional loves. My parents have been giving me good education and teaching me how to be a good person since my childhood. And it's because of their support that I am able to come to CMU for fulfilling my dreams in research. For my girlfriend Yifan Xue, I am so lucky to have her as my best companion and soul mate for the last five years. She never left me when I was weak, and I couldn't have made through all the struggling without her. I have no debt that we will have the further together.

Abstract

Research efforts in discovering and gaining better understanding of various spin-based physical phenomena over the past decades have propelled the innovation and developments of new generations of memory and logic devices. With utilization of non-volatility inherent in magnetism and low-power consumption characteristics, these novel device concepts present new opportunities for future electronics and computers. In recent years, magnetization switching via spin-orbit torques (SOTs) has come out as a promising candidate for advanced memory and computing applications, as it gives the advantages of low power consumption as well as ultrafast writing speed. The underlying mechanisms by which the SOTs induce the magnetization switching, however, turns out to be quite complex. Furthermore, for perpendicularly magnetized systems, i.e., perpendicular MRAM, the SOT driven magnetization switching of the free layer often requires an external in-plane field that significantly hinders the technological viability of commercial implementations.

In this research work, we aim to gain a deeper understanding of the SOTs and their roles in inducing the magnetization switching; in turn, by means of material or device engineering, we can control the SOTs to achieve the desired switching outcomes. We particularly focus our study on the perpendicularly magnetized systems because the high perpendicular magnetic anisotropy (PMA) in these systems makes them appealing for practical applications.

A major part of this research work emphasizes on the elimination of the need for an external magnetic field in the SOT switching of a perpendicular magnet. One strategy to achieve the field-free perpendicular SOT switching is through creating a magnetic field that's localized within the device. The origin of such internal field can come from the interlayer exchange coupling. Based on this idea, we demonstrate robust field-free perpendicular magnetization switching by utilizing the spin Hall effect and interlayer exchange coupling of iridium (Ir). This is the first reported clear experimental demonstration that a heavy metal layer, Ir in particular, is capable of serving as both

a spin current source and an interlayer exchange coupling layer. An additional important characteristic of Ir is that its interface with either Co or FeCoB facilitates strong perpendicular magnetic anisotropy. These combined properties allow us to achieve the SOT driven magnetization switching of a perpendicular Co layer in absence of an external field. Besides the field-free switching of a single layer, we also show that the switching scheme can be well integrated with the MgO-based magnetic tunnel junction (MTJ). We show that the three-terminal MTJ device with the Ir-enabled switching exhibits reliable writing and reading operations at zero external field, moving a step closer to the practical applications of the SOT-related magnetoresistive devices.

In addition to engineering the SOT materials, we provide another solution by altering the device design. The idea is based on the well-known phenomenon that a current carrying wire produces an effective magnetic field around it. Compared to the conventional three-terminal device, our device contains an additional current line orthogonal to the write path, which can generate an in-plane Oersted field during the SOT writing. Facilitated by this Oersted field, reliable SOT switching of the perpendicular MTJs is obtained without applying an external field. The switching characteristic also renders our device unique advantages in terms of preventing the half selecting issue.

In the study of the switching dynamics, we find the switching process in our devices often starts with domain nucleation followed by the domain wall motion (DWM) to expand the reversed domains. This inspires us to dig deeper into the SOT driven DWM and explore the ways in manipulating the DWM so as to control the magnetization state of a perpendicular magnet. In this work, we investigate the DWM in a system with two heavy metal underlayers that have the opposite spin Hall angles. By simply varying the relative thicknesses of these two underlayers, we can manipulate the polarity of the SOTs exerting on the DWs, which further allows us to control the direction of DWM. Based on our findings, we propose a wedge DW device where the SOT driven DWM can effectively give rise to the expansion of reversed domains and thereby realize the magnetization switching.

Lastly, we show the initial experimental works for developing a novel DW device known as mCell, which can be used as the computing unit in non-volatile logic circuit without the integration with CMOS. We develop a magnetic oxide (FeO_x) layer that can serve as the electric-insulating

magnetic layer inserted in between the write path and read path of mCell. The FeO_x insertion layer not only provides sufficient magnetic coupling between the adjacent magnetic layers, but also significantly enhances the DWM in terms of the DW velocity and power efficiency.

Table of content

Acknowledgements ..... **iii**

Abstract ..... **v**

Table of content ..... **viii**

List of Figures ..... **xi**

List of Tables ..... **xx**

Chapter 1 Introduction and Background **1**

1.1 Outline of the dissertation 5

Chapter 2 Spin-orbit effects and Spin-orbit Torques **8**

2.1 Spin-orbit interaction and spin-orbit effects 8

2.1.1 Spin Hall effect 10

2.1.2 Rashba effect 13

2.2 Spin orbit torques 13

2.3 SOT driven magnetization switching 16

2.4 Choice of device geometry for practical applications 20

2.5 Domain wall motion 21

2.6 Applications and devices 24

Chapter 3 Experimental methods **27**

3.1 Film and device fabrication 27

3.1.1 Film deposition 27

3.1.2 Nanopillar device fabrication 28

3.1.3 Domain wall device and Hall-bar device fabrication 36

3.2 Characterization 37

3.2.1 Hysteresis loop measurement 37

3.2.2 Lattice structure characterization 37
3.2.3 Hall-bar device testing 38
3.2.4 Three-terminal SOT device testing 39
3.2.5 Domain wall motion measurement 40
Chapter 4 Field-free Magnetization Switching with Iridium 42
4.1 Material selection 42
4.2 Interlayer exchange coupling and spin Hall effect of Ir 44
4.3 Field-free magnetization switching of a perpendicular Co layer 46
4.4 Switching process 49
4.5 Simulation 53
4.6 SOT Switching with Ir at other thickness 55
4.7 Replacing Ir with other spin Hall materials 55
4.8 Summary 58
Chapter 5 Ir-enabled Field-free Spin-orbit-torque Switching of Perpendicular Magnetic Tunnel Junction Device 60
5.1 Development of p-MTJs 60
5.1.1 MTJ background 61
5.1.2 Experimental development 63
5.2 Experimental development of the field-free three-terminal SOT device 71
5.2.1 Thermal stability of the interlayer exchange coupling via Ir 71
5.2.2 SOT switching of a perpendicular FeCoB layer 73
5.2.3 Field-free SOT switching of p-MTJ device 77
5.3 Summary 86
Chapter 6 Field-free Spin-orbit-torque Switching by Device Engineering 87
6.1 Device design 87
6.2 Results and discussions 88
6.3 Summary 95
Chapter 7 Tailoring the Current-induced Domain Wall Motion by Engineering the Heavy Metal Underlayers 96
7.1 Study of W structure 96

7.2 Film stacks and DW chirality 98
7.3 Current-induced DWM 100
7.4 SHE-induced magnetization switching 103
7.5 Proposed device 105
7.6 Summary 106
Chapter 8 Spin-orbit Torque Driven Domain Wall Motion with a Magnetic Oxide Interlayer for mCell Application 107
8.1 mCell introduction 107
8.1.1 Materials selection for mCell 108
8.2 DWM in Pt/[Co/Ni] wire 109
8.2.1 Annealing effect on current-induced DWM 111
8.3 DWM in magnetic bilayers coupled by a magnetic oxide interlayer 113
8.3.1 Magnetic property 113
8.3.2 Tunneling resistance of the magnetic oxide 115
8.3.3 Current-induced domain wall motion with the magnetic oxide interlayer 116
8.3.4 Discussion 119
8.4 Summary 119
Chapter 9 Conclusion and Future Work 121
9.1 Summary 121
9.2 Suggestions for future work 123
9.2.1 Lowering the power consumption 123
9.2.2 mCell development 126
9.2.3 Engineering the spin current 127
9.3 Exploring new applications 127
Reference 130

List of Figures

Figure 1.1 Magnetization switching by the current-induced spin torques. (a) STT switching, (b) SOT switching. Picture from J. Sinova and T. Jungwirth (2017)[29]. 4

Figure 2.1 (a) Lab frame: the electron orbits around a nucleus. (b) Electron's rest frame: from the electron's view, the nucleus has a relative orbital motion around it, which produces an effective magnetic field on the electron. 9

Figure 2.2 Illustration of the SHE: a horizontal charge current generates a vertical spin current, with the spin polarization orthogonal to both the spin current and charge current. 10

Figure 2.3 (a) Skew scattering where the interaction between the conduction elections and impurities leads to a transverse spin electric field $Espin$. Here, the spin polarization of the electrons is set along the z direction, so the scattering occurs in the transverse direction. (b) Intrinsic mechanism for SHE (Picture from reference [27]). (left) An equilibrium spin texture with spins normal to the momentum at the Fermi surface. (right) With applying a charge current, the Fermi surface shifts in the same direction. The change in the momentum space induces an effect magnetic field that tries to align the spins back to their original positions. The tilting of spins turns out to be opposite at the opposite side of the Fermi surface. 12

Figure 2.4 Rashba effect resulting in the spin accumulation at the interface. 13

Figure 2.5 Relative configurations of (a) the damping-like torque $\boldsymbol{TDL}$ and the field-like torques $\boldsymbol{TFL}$ and (b) their effective magnetic fields. 14

Figure 2.6 Modeling results showing the magnitude of damping-like torque (red line) and field-like torque (blue line) as the function of (a) heavy metal thickness and (b) ferromagnet thickness. Picture from reference [44]. 16

Figure 2.7 Top panel: illustrations of (a) the type-z device, (b) the type-y device and (c) the type-x device. Bottom panel: magnetization trajectories during switching from macrospin simulations. Picture from reference [31]. 17

Figure 2.8 Relative orientations of $\boldsymbol{H}DL$, $\boldsymbol{T}DL$ with (a) up- and (b) down-magnetization. If ignoring the external field $\boldsymbol{H}x$, the up and down states are symmetric with respect to $\boldsymbol{T}DL$ and thus they are identically energetically favorable. Introducing $\boldsymbol{H}x$ breaks the symmetry and, in this case, makes down-magnetization more favorable. 19

Figure 2.9 The two types of DW in perpendicular thin films. (a) the Neel-type DW, shown with the right-handed chirality. (b) the Bloch-type DW. 23

Figure 2.10 Examples of the SOT devices. (a) Three-terminal device with the in-plane MTJ, by LQ. Liu, *et al*. (2012)[19]. (2) Three-terminal device with the p-MTJ, from M. Cubukcu, *et al*. (2014)[64]. (c) Racetrack memory, from IBM[67]. (d) mCell by JG. Zhu[69,70]. 26

Figure 3.1 Process flow of the nanopillar device fabrication. 29

Figure 3.2 SEM images: (a) top view of the 60 nm C/5 nm SiN/ HSQ milling mask and (b) titled angle view of the nanopillars after ion milling. 32

Figure 3.3 (a) The surface of the nanopillar device after planarization. (b) A properly opened top window. 32

Figure 3.4 SEM image of a fabricated three-terminal MTJ device 32

Figure 3.5 Process flow of the Hall-bar device fabrication. 36

Figure 3.6 Optical images of (a) a Hall-bar device consisting of 2-μm-wide current- and voltage-channels and (b) a domain wall device with a 2-μm-wide wire. 37

Figure 3.7 Illustration of the measurement set-up for the Hall-bar device testing. 38

Figure 3.8 Illustration of the three-terminal SOT device testing 39

Figure 3.9 (a) Schematic of the domain wall motion testing. (b) Illustration of the testing procedure. 41

Figure 4.1 The designed device that utilizes IEC to assist the SOT switching of a perpendicular magnet. The heavy metal layer in the middle can provide IEC so that the top perpendicular layer $\boldsymbol{m2}$ experiences an in-plane exchange coupling field $Hlocal$ from the bottom in-plane layer $\boldsymbol{m1}$. The antiferromagnetic coupling is shown in this drawing. 43

Figure 4.2 Antiferromagnetic coupling field as a function of the Ir spacer thickness. Top right: perpendicular M-H loop of Co (1.1 nm)/ Ir (1.35 nm)/ Co (1.1 nm). 44

Figure 4.3 (a) Schematic of the Hall-bar device. (b) Anomalous Hall voltage as a function of the perpendicular field. (c) Anomalous Hall voltage as a function of the current density applied in the current channel of the device w/o an external in-plane field. 46

Figure 4.4 (a) Film stack for field-free magnetization switching, with unit in nanometers. (b) In-plane hysteresis loop of a pure SAF structure with the film stack of substrate/ Ta/ Co(2 nm)/ Ru(0.85 nm)/ Co(2 nm)/ Ta. (c) Schematic illustration of the Hall-bar device for spin-orbit torque measurement. (d) Perpendicular-field-driven anomalous Hall effect loop for the device with the film stack shown in (a). 47

Figure 4.5 Anomalous Hall voltage as a function of injected current density with different external magnetic fields Hx along the current direction. Bottom SAF is set as (a) ⇄, and (b) ⇆. 49

Figure 4.6 Kerr microscope images showing the domain wall propagation during the current-induced magnetization switching process, without external magnetic field. Current is applied in –x (left) and +x (right) directions. Bottom SAF is set as ⇄ . Between image in each column: 100-ns pulse, 1 pulse. 50

Figure 4.7 (a) Schematic illustration of right-handed domain wall structures in Ir/Co system. Red arrows: down-up domain wall. Blue arrows: up-down domain wall. (b) Domain wall structures in presence of the exchange coupling field. 50

Figure 4.8 Schematic of magnetic bubble domain measurement. Solid circle: initial bubble domain. Dashed circle: bubble domain after growth. Black arrow: magnetization at center of DW. (b) Velocity of down-up and up-down domain wall as a function of in-plane magnetic field. The perpendicular field used for growing the bubble domain has the magnitude of Hz = 50 Oe. 52

Figure 4.9 Simulated domain expansion in the perpendicular Co layer in the presence of the in-plane coupling field. The charge current flows along the x-axis. $t_1 < t_2 < t_3 < t_4$ represents the time evolution during the application of current. 54

Figure 4.10 Calculated domain wall moving speed under the SHE generated spin current as a function of the direction cosine of the wall center magnetization along the wall tangent with four different in-plane coupling field strengths. 54

Figure 4.11 Current switching results with a 3-nm Ir. 55

Figure 4.12 Current switching results in W-based device. The switching loops are measured under various external in-plane fields starting from +1000 Oe to -500 Oe 56

Figure 4.13 Current switching results with Pt. (a) The device is first saturated and the switching loop is recorded at Hx = +1000 Oe. Then the field is turned off and switching loop is measured again. (b) Hx is first set as -1000 Oe and then to 0 Oe. 57

Figure 4.14 Calculation of the stray field. The blue rectangle is the in-plane Co layer that's viewed as a single domain. Point A and B are at the two ends of the in-plane layer. Point C denote the center position of the perpendicular layer. Here, $2l$ = 12 μm and d = 2 nm. 58

Figure 5.1 Two resistance states of an MTJ depending on the relative orientations of two ferromagnetic layers 62

Figure 5.2 Hysteresis loops of the bottom FeCoB stacks with (a) 1.2 nm and (b) 2 nm FeCoB layer. 63

Figure 5.3 Effective anisotropy as a function of FeCoB thickness 65

Figure 5.4 Effective anisotropy vs. annealing temperature. 66

Figure 5.5 Hysteresis loops of the MTJ stack with 1 nm MgO. Inserted: small-field perpendicular M-H loop. 66

Figure 5.6 (a) Schematic of the MTJ stack and device. (b) Perpendicular-field-driven TMR loop. Blue dashed line: TMR minor loop. (c) The effect of annealing temperature on TMR. 68

Figure 5.7 (a) RA product vs. MgO thickness. (b) TMR vs. RA product 68

Figure 5.8 M-H loop of a perpendicular SAF showing the antiferromagnetic coupling between two [Co/Pt] multilayer stacks via Ru. 69

Figure 5.9 (a) The film stack of the MTJ with a top SAF. (b) Top: large-field perpendicular hysteresis loop of the films. Bottom: small-field minor loop of the free FeCoB layer. *X* is the number of repetitions of the [Co/Pt] multilayers in the top part of the SAF. 71

Figure 5.10 The effect on annealing on IEC. (a) In-plane exchange coupling in Co (2 nm)/ Ir (1.35 nm)/ Co (2 nm). (b) Perpendicular exchange coupling in Co (1 nm)/ Ir (1.35 nm)/ Co (1 nm) ... 72

Figure 5.11 In-plane hysteresis loop of the film with a bottom IrMn layer. The film is post-annealed at 300 ^{0}C for 10 min in presence of a 5 kOe magnetic field parallel to the film plane. The loop is measured along the annealing field direction. 73

Figure 5.12 (a) Film stack for SOT switching of the coupled bilayers. (b) Small-field perpendicular hysteresis loop of the film. (c) Current-induced switching results measured in the patterned Hall-bar device. 74

Figure 5.13 (a) In-plane M-H loop showing the IEC between FeCoB and Co via the 1.35-nm Ir spacer. (b) M-H loops demonstrating the PMA of FeCoB/ MgO on an Ir buffer layer. 75

Figure 5.14 (a) Film stack for the SOT switching of the perpendicular FeCoB. (b) Small-field perpendicular hysteresis loop of the film. (c) Current-induced switching results measured in the patterned Hall-bar device. 76

Figure 5.15 (a) Left: film stack, unit in nanometer. Right: M-H loops of the film. (b) Left: schematic of the device and testing set-up. Right: Perpendicular-field-driven TMR minor loop of

a device with a 150-nm-diameter MTJ. (c) Cross-section TEM images of the devices with a 50-nm-diameter MTJ and a 150-nm-diameter MTJ. (d) Top-view SEM image of the device. 79

Figure 5.16 (a) Illustration of the testing set-up. (b) Current-induced switching w/o an externally applied field along current direction. The device has a 2.5 μm-width write path and a 150-nm-diameter MTJ. (c) Zero-field switching of the p-MTJs with applying a sequence of positive and negative switching pulses. 80

Figure 5.17 Measured switching current as a function of (a) the width of the write path and (b) the MTJ size. 82

Figure 5.18 (a) Zero-field switching dynamics of the free FeCoB layer in a 240 nm x 240 nm device. Time: $\tau 1 < \tau 2 < \tau 3 < \tau 4$. (b) Comparison of the switching in devices with various sizes. (c) Simulated trend in the switching current as a function of MTJ size. 82

Figure 5.19 (a) Switching current with different pulse width τ. Upper: Switching current is plotted as a function of inverse τ. (b) Simulated switching current as a function of the inverse pulse width. 85

Figure 5.20 (a) Simulated critical current density as a function of the PMA of the free layer. (b) Simulated switching current as function of the pulse width with different perpendicular anisotropy of the free layer (black curves). The blue curve fits the level-off current of each black curve and shows how the switching current changes when considering the heat effect. The red dots correspond to the experimental data. 85

Figure 6.1 (a) Schematic of the field-driven MRAM where two orthogonal current-generated magnetic fields are used to switch to in-plane MTJ. (b) The design of our field-free-switching device where the bottom line is a spin-current source and the top line is responsible for generating an Oersted field. 88

Figure 6.2 (a) Film stack, numbers in nanometer. (b) Hysteresis loops of the annealed film. Inserted in the perpendicular loop: minor loop of the free layer. 89

Figure 6.3 (a) Schematic of the device. (b) Field-driven TMR minor loop of the device. (c) Top-view SEM image of the fabricated device. (d) Cross-section TEM image of the MTJ. 90

Figure 6.4 Current switching results with an external field of (a) Hx=+500 Oe, (b) Hx=0 Oe, and (c) Hx=-500 Oe. No current is applied into the field path during writing. 90

Figure 6.5 (a) Sketch of the device and the current configurations. (b) The testing set-ups with the write current $I1$ applied in opposite directions, where the direction of the field current $I2$ is fixed. (c) Current switching without an external field. Here, the resistance of the write path and field path is 1750 Ω and 30 Ω, respectively. Each resistor connected with the field path is set as 95 Ω. 91

Figure 6.6 The detected MTJ resistance with a sequence of write current $I1=\pm 4.5$ mA where the magnitute of the field current is varied. 92

Figure 6.7 Current switching results in the presence of an in-plane field Hx. Different from Figure 6.4, here the current is sent into both the bottom and top paths. 93

Figure 6.8 Simulation of the Oersted field from the field current. The yellow rectangle is the cross section of the field path that has the dimension 1500 nm × 60 nm. The free layer of the p-MTJ is simplified as a dimensionless point, and it's 50 nm away from the bottom of the field path. The field path is divided into 1 nm × 1 nm grids. The magnetic field $\boldsymbol{Hgrid}$ from the current flowing in each grid is calculated, and all fields are combined to obtain the total effective field. **Courtesy**: Yuwei Qin. 94

Figure 6.9 The switching diagram with respect to $I1$ and $I2$, where the blue regions shows the set of currents that can deterministically select the MTJ state. The black circles are the measured critical switching current. The dashed lines are the fits of the trend of the black circles. 95

Figure 7.1 (a) Illustration of the (top) BCC and (bottom) A15 structures . Compare with BCC structure, A15 structure has two additional atoms on each face. Note that atoms with different sizes illustrated in the A15 structure are only to distinct their atomic positions. In actual, they should be identical W atoms. (b) XRD measurement results for the films with different W thickness. 97

Figure 7.2 Perpendicular and in-plane M-H curves for the stacks with, from left to right, 0.6 nm, 0.8 nm, 1 nm and 1.5 nm W layer. 99

Figure 7.3 Results of the magnetic bubble domain testing obtained from the film with 1 nm W. (a) Schematic of the testing set-up. (b) Examples of the Kerr microscope image showing the shape of bubble domains after applying pulses of perpendicular field H_z = 50 Oe, with and without a static in plane field $H_x = \pm 400$ Oe, Dark circular region in the middle of each image is the size of the bubble domain initially created. Arrows on the domain walls indicate right-handed chirality. (c) Velocity of down-up and up-down domain wall as a function of in-plane magnetic field. 99

Figure 7.4 Current induced domain wall motion for devices with different W layer thicknesses. (a) Kerr microscope images showing the domain wall motion under applied voltage 0.75 V/μm for devices with 0.6 nm and 1 nm W layer. Between images: 20 pulses with 200 ns pulse length. (b) Summary of the domain wall velocity as a function of the W layer thickness. 101

Figure 7.5 Top row: Illustration of injection of the spin currents with opposite signs of spin polarization generated by the two heavy metal layers. Left: W layer < 0.8 nm, Right: W layer > 0.8 nm. Thin red and blue arrows denote the spin directions. Bottom row: Illustration of the SOT DWM in the perpendicularly magnetized FeCoB layer. Blue arrows: magnetization direction. Thin black arrows: damping-like fields from the SOTs exerted on DW magnetization 102

Figure 7.6 (a) Optical image of the device (middle) and schematic of measurement settings. (b) Current-induced switching loops for devices with 0.6nm and 1.5 nm W layer. Top row: in-plane field applied along -x direction and bottom row: field along +x direction. 104

Figure 7.7 Proposed DW device that contains a W wedge. Due to the W thickness variation, the spin currents in the left and right parts of the device have opposite spin polarizations. 106

Figure 8.1 (a) The design of the mCell. (b) Low and high resistance states of a mCell, which is controlled by the SOT-driven DWM. 108

Figure 8.2 (a) Film stack and hysteresis loops of the film. (b) Top: optical image of the DW device and the sketch of the testing set-up. Bottom: DWM images captured by the Kerr microscope. $Jc = 1.5 \times 10^{12}$ A/m^2, 1 pulse between images. (c) DW velocity as the function of current density in Pt.

(d) Velocity of the up-down DW as a function of the in-plane magnetic field Hx, under $Jc = \pm 1 \times 10^{12}$ A/m^2. 110

Figure 8.3 The effect of annealing on (a) the anisotropy field, (b) the effective DMI field, (c) and (d) DW velocity. 112

Figure 8.4 EDS mapping of Pt, Ni, Co and Ta in the films (a) before annealing and (b) after annealing at 300 ^{0}C. 112

Figure 8.5 Normalized (a) perpendicular and (b) in-plane magnetization versus applied field curves for the bilayer stacks with 0.8 nm (red) and 1.2 nm (blue) FeOx insertion layer. 114

Figure 8.6 (a) Schematic of the 3.5 μm-diameter circular device for resistance measurement. (b) Device resistance for stacks with 3 nm, 5 nm FeO_x insertion layer or 5 nm Ta insertion layer. 116

Figure 8.7 (a) Kerr images showing current induced DWM for the bilayer stack with 0.8 nm FeO_x insertion layer under 0.7 V/μm, 100 ns and 2 pulses. (b) Domain wall velocity as a function of voltage per unit wire length for the coupled bilayer stack and the Co/Ni stack. (c) Kerr images showing irregular DWM of the coupled bilayer stack under 1.15 V/μm, 100 ns and 2 pulses. . 118

Figure 9.1 The exchange coupling field as a function of the Pt concentration in $Ir_{(1-x)}Pt_x$. The exchange coupling fields are extracted from the M-H loops of a series of films containing substrate/ Ru(2 nm)/ IrMn (5 nm)/ Co (2 nm)/ $Ir_{(1-x)}Pt_x$ (1.35nm)/ FeCoB (2 nm)/ MgO (2 nm)/ Ta (2 nm). All films are annealed at 300 ^{0}C for 10 min. 125

Figure 9.2 Lowering the critical field current. Here the field path is pre-patterned within the substrate and is below the write path of the device. 125

Figure 9.3 mCell design with the developed field-free switching schemes. (a) Ir-enabled fied-free switching. (b) Field-free switching assisted by the Oersted field. 127

List of Tables

Table 2.1 Survey of the direction of DWM with different combinations of heavy metal and ferromagnet materials 24

Table 3.1 Sputtering conditions for the materials used in our experiments..... 28

Table 3.2 Parameters used in step (b) 33

Table 3.3 Parameters used in step (c) 34

Table 3.4 Parameters for top window opening 34

Table 3.5 Parameters for bottom window opening..... 35

Table 3.6 Parameters for Au deposition and lift-off in top electrode fabrication..... 35

Table 4.1 Summary of the IEC, SHE and PMA of some spin-Hall and RKKY materials..... 44

Table 8.1 The Anisotropy field (Hk), coercivity (Hc) and saturation magnetization (Ms) of the bilayer stack with 0.8 nm FeO_x insertion layer, the Co/Ni stack and the FeCoB stack..... 114

Chapter 1
Introduction and Background

The breakthrough in data storage and processing unit design in the past decades led to an unprecedented boom in artificial intelligence (AI) and big data analysis. However, behind the stunning success of AI and big data are as well stunningly massive amounts of energy that consumed by the supporting hardware at the background, which has started to become a major challenge for future generation of data centers. The continuing fast growth of big data is now yelling for more efficient hardware support that requires revolution in both device and material that being used. Currently, units in memory and CPUs are most realized by utilizing the ability of electrons of carrying charges. This requires power supply to be kept on, even when the unit is not processing any data, thus to keep the information stored, and the unit ready for any incoming computation task. Note that, a functional unit in memory or CPUs spends most of the time on waiting rather than writing information or doing computations, thus it's the persistent demand of power that results in huge amount of power waste. One solution to this problem is thus to develop devices that are nonvolatile.

With that, people notice electrons have another basic characteristic, spin – a quantum magnetic moment, that has the potential in low-power memory and logic applications. This comes with the concept called spintronics[1,2] which refers to the devices utilizing electron spins, instead of electron charges, to store and transfer information. In spintronic devices, information is represented as orientations of spins in magnetic materials with uniaxial easy axis. Since spin states do not intrinsically rely on electrical power supply, it naturally renders spintronic devices the advantage of nonvolatility and hence low power consumption.

The rapid progress in discovering and developing novel spintronics begins with the commercialization of a spin-based device, known as spin valve, that consists of two ferromagnetic layers (iron, nickel, cobalt or their alloys) sandwiching a thin non-magnetic spacer. In the early spin valves, the spacer is usually a metal layer (for instance. copper) and these spin valves can exhibit giant magnetoresistive (GMR) effect[3–5]: the resistance is lowest when the magnetizations of the two ferromagnetic layers are parallel-orientated while highest when magnetizations are antiparallel-orientated. In order to better control the resistance via the alignments of magnetic moments, one of the ferromagnetic layers is often pinned, that is, hard to be switched by moderate magnetic field. The pinning can be achieved by adding the contact with an antiferromagnetic materials or exchange coupled with a synthetic antiferromagnetic (SAF) stack (such as Co/Ru/Co)[6]. The other ferromagnetic layer is free to change orientation, in other words, its magnetization is relatively easier to be rotated by magnetic field. As such, by controlling the exertion of magnetic fields, we can manipulate the relative orientations of the two ferromagnetic layers and thus change the resistance of a spin valve. Note that the magnetoresistance difference between parallel and anti-parallel configurations from GMR effect ranges from 0.5% to 15% at room temperature[7]. The direct application of spin valve is the magnetoresistive detector for probing the change of magnetic moment of a nanomagnet, such as the magnetic nanoparticles in hard disk drives. And it's the scalability of such GMR reader down to tens of nanometers that has enabled dramatic improvement in the storage capacity of hard disk drives in the past decades.

The spin valves with a thin insulating spacer (AlO_x or MgO), known as magnetic tunnel junctions (MTJs), exhibit significantly larger magnetoresistance change compared with GMR effect. It has been reported that the tunnel magnetoresistance ratio (TMR) in AlO_x-based MTJs could reach up to 70%[8] while later developed MgO-based MTJs showed unprecedently over 600% TMR[9] at room temperature. Hence, besides being used as sensors, MTJs with such large TMR open new perspectives for next-generation memory and computing applications. The best-known technology with its core based on MTJs is the magnetoresistive random access memory (MRAM). MRAM is said being able to have the speed of SRAM, the density of DRAM as well as the nonvolatility of hard disk drive[10], which is promising to be the universal memory to be embedded in a computer system. With this being mentioned, however, one should take cautions because there are still lots of technological issues to solve in order to make MRAM applicable and outperform its rivals[11,12].

One of the critical aspects for MRAM to succeed is that it must have a robust writing method as well as fast writing speed. Although several writing methods have been proposed and prototype devices has been demonstrated[13,14], the current-induced spin torque switching turns out to be the most efficient and reliable approach among them. The firstly proposed spin torque switching is via utilizing the so-called spin transfer torque (STT) [15–17]. In STT switching (Figure 1.1(a)), a vertical charge current is passed through the MTJ and subsequently, spin polarized by the pinned ferromagnetic layer. This spin polarized current carries a major type of spins, tunneling through the barrier, and re-orientates the free layer via spin angular momentum transfer. By controlling the direction of the applied current, one can obtain the magnetization of the free layer aligned or anti-aligned with the pinned layer, and thus the MTJ is set as low or high resistance state. The critical current density for STT switching is usually 10^{10}-10^{12} A/m^2 and the overall writing current scales down for smaller devices as fewer amounts of spins are needed for switching tinier magnets. Writing information by STT has been proved to be robust, which can reach the write error rate below 10^{-11} with sufficient applied current[2]. The writing speed of STT-MRAM ranges from 2-30 ns that is faster than most of the common DRAMs. Note that STT-MRAM is regarded as a two-terminal device as the writing and reading share the same current path within the MTJ but they differ in the magnitude of current. Because of the two-terminal design, STT-MRAM often has strict requirements in the MTJ performance. The MTJ not only needs to have low resistance (< 10 $\Omega \cdot \mu m^2$) and large signal (> 150 % TMR) but also able to sustain under the large writing current, which poses challenges in the material selection and fabrication of the MTJ. Meanwhile, sharing the write- and read-paths can also cause unwanted writing if the magnitudes of writing current and read current are not well distinct. Nevertheless, with decades of dedicated industrial development, the STT switching enabling fast and reliable writing may eventually lead to the take-off of MRAM within the next few years.

In efforts to explore more advanced spin torque switching method, people has come up with a three-terminal design for MRAM where the writing current only goes through a spin-polarization layer below the MTJ (Figure 1.1(b)). The spin-polarization layer can be with a heavy metal (Pt[18], Ta[19] or W[20]), antiferromagnet (IrMn[21,22], PtMn[23]), or topological insulator (BiSe[24–26]). By injecting longitudinal charge current into the spin-polarization layer (here is also the write-path), a pure spin current or spin accumulation can be generated via spin Hall effect[27] and/or other spin-orbit coupling phenomena such as Rashba effect[28]. The spin current further diffuses into the

adjacent free layer, then interact with the magnetic moment, and exert torques to switch it. Because the spin current or accumulation is induced by either bulk or interfacial spin-orbit interactions, their resulted torques are referred to as the spin-orbit torques (SOTs) and it associated switching is known as the SOT switching.

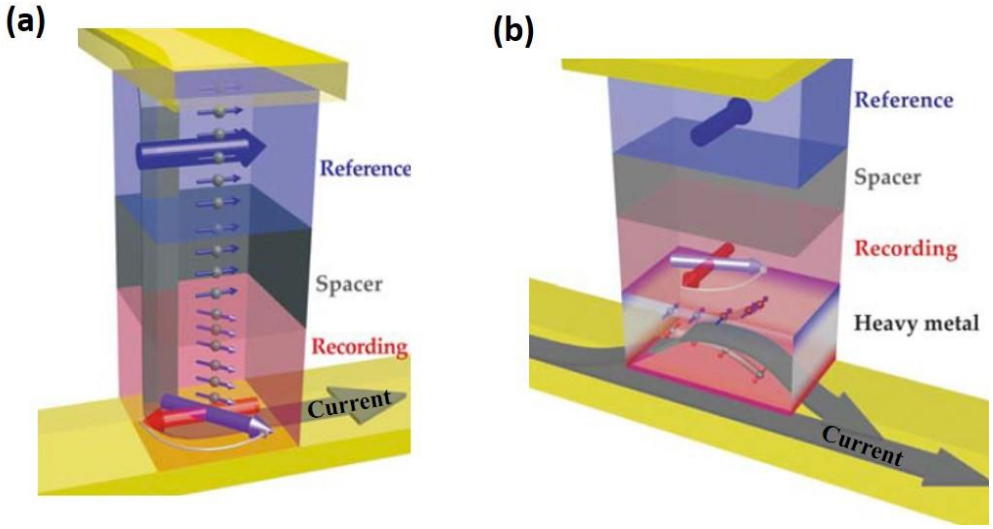

Figure 1.1 Magnetization switching by the current-induced spin torques. (a) STT switching, (b) SOT switching. Picture from J. Sinova and T. Jungwirth (2017)[29].

There are some advantages of the three-terminal devices naturally rendered by its design. The first is that the writing current is passed underneath the MTJ instead of going through it. Such design effectively prevents barrier breakdown issue that sometimes occurs during the writing in the two-terminal device. The separate read and write paths also allow individual optimizations of the reading and writing functions. In terms of the switching, one of the benefits of SOT switching is that it gives surprisingly fast switching speed. We know that in the STT switching the flipping of the magnetization of the free layer begins by thermal fluctuations since the magnetization feels no torque when it's perfectly aligned or anti-aligned[30]. Thus, the magnetization usually precess around its original state for a while, then rotates to the desired direction. The initial precession is a probabilistic process and takes up a large portion of time during the entire switching. The SOT switching, on the other hand, can eliminate the initial incubation time in some switching geometry[31]. As a result, the SOT switching of a perpendicular magnet has been found to be capable of reaching the writing speed within fractions of a nanosecond[32,33], faster than the STT switching. Another beneficial feature of SOT switching is that the switching condition is

determined by current density. It makes the current scalable for nanoscale devices. Although the threshold current density is also 10^{11}-10^{12} A/m^2, the write path is usually very thin (2-10 nm), thus making the switching current small for nanoscale devices.

There are also some challenges and unsolved problems in SOT switching, particularly for the perpendicularly magnetized systems. First, the mechanisms by which the SOTs switch the magnetic moment or move the domain walls in a perpendicular magnet are rather complex. Several bulk and interfacial spin-orbit coupling phenomena can act together to cause the experimental observations. In order to control the SOTs for magnetization switching, it's important to understand those effects individually, and to be able to tune those effects via material or device engineering. Another issue arises from the in-plane spin polarization of spin current. The transversely polarized spin current causes SOTs to be good at effectively switching an in-plane magnetized layer[19,20,31]. For perpendicularly magnetized systems, i.e. the perpendicular MTJs, however, an in-plane field has to be applied for assisting the switching of the perpendicular free layer[18,31]. But applying an external magnetic field significantly hinders the technological viability of SOT devices for commercial applications. So it's vital to find ways to eliminate the need for the external field in the perpendicular SOT switching.

1.1 Outline of the dissertation

In **Chapter 1**, we briefly surveyed the history of spintronics as well as the application areas where spintronics can be useful. We introduced the concept of SOT switching and its advantages, as well as states the challenges in SOT switching that motivate this our research work. In **Chapter 2**, we will discuss the physical origins of two important spin-orbit effects, the spin Hall effect and the Rashba effect, and their associated SOTs. We will analyze the mechanisms by which the SOTs affect the magnetic state and dynamics in the perpendicularly magnetized heavy metal/ ferromagnet/ oxide heterostructures. We will also review some previous experimental results by other research groups. In **Chapter 3**, we will provide the complete fabrication recipes of the various SOT devices used in our work. We will describe the fabrication process for patterning the nanoscale magnetoresistive device with the size of MTJ pillar down to 50 nm. The fabrication recipes have been proven to be reliable and repeatable based on many cycles. Furthermore, we will cover the characterization techniques for examining the switching profiles of the SOT devices.

Although the SOT switching of a perpendicular magnet can give ultrafast switching speed down to hundreds of picoseconds, an in-plane magnetic field is required to break the symmetry for obtaining the deterministic switching. Applying an external in-plane field for the perpendicular SOT switching is the common solution in many research experiments but it poses realistic technical difficulties for practical applications. In **Chapter 4**, we will describe a strategy to produce a naturally existed in-plane field that's localized in each individual device, so that the need for applying an external field is eliminated. We will demonstrate the heavy metal material, iridium (Ir) in particular, can serve for the dual functions: create a local in-plane field via interlayer exchange coupling and provide a spin current by spin Hall effect. It's also found that Ir can promote strong perpendicular magnetic anisotropy (PMA) with Co and Co-based alloys. Facilitated by these properties of Ir, we achieve the deterministic SOT switching of a perpendicular Co layer in absence of an external field.

Beside the switching of a single perpendicular layer, we'd like to extend the Ir-enabled field-free switching scheme to work on the magnetoresistance device. So in **Chapter 5**, we will show the experimental development of the three-terminal magnetoresistance device that utilizes Ir for the SOT writing. To get functional three-terminal device, we first study and develop the storage unit that's the perpendicular MTJ (p-MTJ). After having the switchable and readable p-MTJ, we then combine the p-MTJ with the Ir switching method to construct nanoscale three-terminal devices. We will present the writing and reading operations in those devices.as well as analyze their switching characteristics.

In the study of the field-free SOT switching, we also attempt to achieve the goal by engineering the device design. We notice that from Ampere's law a current carrying wire can produce an effective magnetic field. With using this principle, in **Chapter 6** we will make a simple modification in the design of the conventional three-terminal SOT device so that it contains an additional current line to generate an in-plane Oersted field. We will show that this in-plane Oersted field can effectively assist the SOT switching of p-MTJs. The new design also renders the device some beneficial features in terms of avoiding the half-select problem.

In addition to inducing the magnetization switching, the SOTs are also capable of moving the magnetic domain walls (DWs). For the SOT switching in the device larger than the width of a

DW, our observations suggest that the switching should take place by domain nucleation followed by the expansions of the reversed domains. The SOT driven domain wall motion (DWM) turns out to be an interesting topic that contains the interplay of several spin-orbit effects. It would be desirable if we figure out how to control the SOT DWM efficiently and to utilize it to manipulate the magnetization state of a perpendicular magnet. In **Chapter 7**, we will show the experimental investigation of the DWM driven by the competing spin currents from two heavy metal underlayers. We will demonstrate a simple way to control the direction of DWM. Based on our results, we propose a wedge device where the DWM is controlled in purpose to realize the field-free perpendicular SOT switching.

Continuing the study of the SOT DWM, we will then explore a novel DWM-based device called mCell. The mCell is a four-terminal magnetoresistive device proposed by our group, which can be used for non-volatile logic circuit without the integration with CMOS. In **Chapter 8**, we will show some initial works for mCell development that focus on the DWM writing. Specifically, we will talk about the experimental development of a magnetic oxide interlayer that fits the mCell design.

In **Chapter 9**, we will summarize the key results obtained in our research work and provide suggestions for future research in this area. We will also discuss some potential applications of the SOT device that's beyond the non-volatile memory.

Chapter 2
Spin-orbit effects and Spin-orbit Torques

In this chapter, we first review two important phenomena accounting for the generation of a spin current: the spin Hall effect (SHE) and the Rashba effect. Both of them originate from the spin-orbit interactions, and their resulted spin current can interact with the magnetic moment of the adjacent ferromagnet by exerting spin-orbit torques (SOTs). We then conduct our analysis in the SOTs within the scope of the heavy metal/ ferromagnet/ oxide heterostructures that's the most studied structure for investigating the SOTs. We discuss how the SOTs affect the orientation of the magnetic moment and alter the magnetization dynamics, which can further lead to the magnetization switching and domain wall motion (DWM).

2.1 Spin-orbit interaction and spin-orbit effects

The spin-orbit interaction describes the relativistic interaction between an electron's spin angular momentum and orbital angular momentum. The spin-orbit interaction is of tremendous importance because it's not only at the root of various magnetic properties such as magnetocrystalline anisotropy, magnetoresistance and magnetic resonance damping but also contribute to some important transport phenomena including SHE and Rashba effect.

Here, we first describe the spin-orbit interaction in a simple form, i.e., an atomic nucleus with one electron, where the magnetic field from the electron's orbital motion can affect the orientation of the spin. As shown in Figure 2.1, in the lab frame, the electron orbits around the nucleus with velocity $\boldsymbol{v}$, and experience a Coulomb field from the nucleus $\boldsymbol{E} = \frac{1}{4\pi\epsilon_0}\frac{Ze}{r^2}\hat{r}$. While in the electron rest frame, the electron sees the positive nucleus to orbit around it. The relative motion of the nucleus produces a magnetic field

$$\boldsymbol{B} = \frac{\mu_0 I}{2r}\hat{z} = \frac{\mu_0}{2r}\frac{Zve}{2\pi r}\hat{z} = \frac{\mu_0 Ze}{4\pi r^3}(\boldsymbol{r}\times\boldsymbol{v}) = -\frac{1}{c^2}(\boldsymbol{v}\times\boldsymbol{E}) \qquad \text{Equation 2.1}$$

acting on the electron. By considering the definition of the orbital angular momentum $\boldsymbol{L} = \boldsymbol{r}\times\boldsymbol{p} = m_e(\boldsymbol{r}\times\boldsymbol{v})$, the magnetic field from the orbital motion is further expressed as $\boldsymbol{B} = \frac{\mu_0 Ze}{4\pi m_e r^3}\boldsymbol{L}$. The magnetic spin moment, on the other hand, is $\boldsymbol{\mu_s} = -\frac{e}{m_e}\boldsymbol{S}$. Therefore, the potential of the spin moment in the magnetic field is written as

$$E_{SOC} = -\boldsymbol{\mu_s}\cdot\boldsymbol{B} = \frac{\mu_0 Ze^2}{4\pi m_e^2 r^3}(\boldsymbol{S}\cdot\boldsymbol{L}) \qquad \text{Equation 2.2}$$

which describes the interaction energy for the coupling of the electrons orbital and spin angular momentum. The interaction energy in Equation 2.2 suggests that spin-orbit coupling can changes electron energy levels and cause shifting to the atomic spectra. The effect on the energy shift in hydrogen atom has been experimentally observed and studied extensively[34]. The coefficient in Equation 2.2 also implies that the spin-orbit effect is stronger in heavier atoms, as indicated by the atomic number Z.

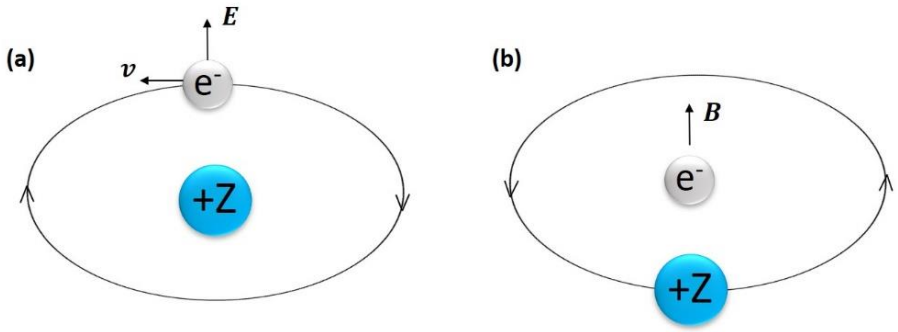

Figure 2.1 (a) Lab frame: the electron orbits around a nucleus. (b) Electron's rest frame: from the electron's view, the nucleus has a relative orbital motion around it, which produces an effective magnetic field on the electron.

In spintronics, the spin-orbit effects in heavy metals, ferromagnetic materials and their interfaces are investigated as they are the host of the deflection of the electrons depending on their direction of the spin and momentum[27,28,35,36]. In the materials with strong spin-orbit interaction, the prominent spin-dependent deflection of conduction electrons can create a spin current or spin accumulation that's transverse to the charge current. The microscopic mechanisms, however, can be quite complicated, where both bulk scattering in materials and effects associated with the

interfaces can act together to contribute to the spin current generation. In the following sections, we will discuss two possible origins: the bulk SHE and the interfacial Rashba effect. In our research, we primarily study the heavy metal/ ferromagnet heterostructures where the SOTs from the SHE dominate in the magnetization switching.

2.1.1 Spin Hall effect

SHE is often found to exist in the non-magnetic heavy metals that have strong spin-orbit couplings[19,20]. Recent research findings also suggest the existence of SHE in antiferromagnetic materials[37] and topological insulators[24,26]. As shown in Figure 2.2, in SHE a longitudinal charge current ($\boldsymbol{J_c} \parallel \boldsymbol{x}$) in heavy metal generates a vertical spin current ($\boldsymbol{J_s} \parallel \boldsymbol{z}$) due to the asymmetric spin-dependent electron scattering. The spin polarization of the spin current is orthogonal to the directions of both the charge current and the spin current, and thus pointing in the transverse direction ($\mathbf{s} \parallel \boldsymbol{y}$). The conversion of the charge current into the spin current can be written as $\boldsymbol{J_s} = \frac{\bar{h}}{e}\theta_{SH}(\boldsymbol{J_c} \times \boldsymbol{s})$, where $\bar{h}$ is the Plank's constant, e is the unit charge, $\theta_{SH} \propto \frac{J_s}{J_c}$ is the spin Hall angle charactering the how efficient the charge current converts into the spin current.

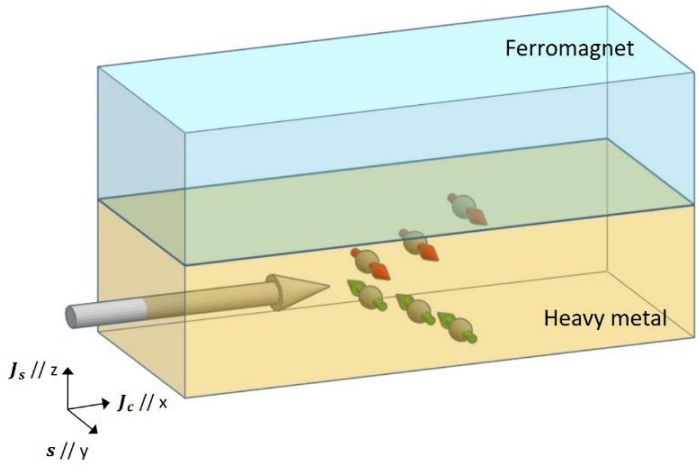

Figure 2.2 Illustration of the SHE: a horizontal charge current generates a vertical spin current, with the spin polarization orthogonal to both the spin current and charge current.

The essential mechanisms for SHE is still a subject of considerable debate, which can be classified into extrinsic and intrinsic mechanisms[27,38,39]. The extrinsic mechanism describes how the spin-orbit interactions with the impurities lead to the asymmetric spin-dependent electron

scattering. It can be further categorized into skewing scattering and side-jump mechanisms. In skew scattering, the spin-orbit interaction between the flow of charge current and the impurities create an effective "spin electric field" transverse to charge current direction (Figure 2.3(a)). Analogous to the action on positive and negative charges by an electric field, the spin electric field can be attractive or repulsive given the sign of the spin polarization. It causes the asymmetric deflection of the electrons in the transverse direction, producing a pure spin current. For side-jump scattering, the electrons change their momenta during the collision with the impurities. The momentum change gives rise to an electric field that displace the electron motion, and the displacement is dependent on the spin polarization. On average of many scattering events, there forms a transverse motion of conductions electrons, which causes a net spin current. The intrinsic mechanism, on the other hand, only relies on the spin-dependent band structure of the material. In Equation 2.2, we saw that the electron's energy levels can be perturbed by spin-orbit coupling. It turns out that the electronic bands near the Fermi surface can also be perturbed via spin-orbit coupling, which results in the intrinsic spin Hall effect. As shown in Figure 2.3(b), when the charge current flows into the material, the electric field displace the Fermi surface along the same direction as the charge current. Due to the move in momentum space, an effective spin-orbit field is generated in order to regain the alignment. In response to such current-induced field, the spins tilt away from their original orientation, where the tilting occurs along the opposite directions with opposite spin polarization, and thereby results in a transverse spin current. The ab initio calculations suggested that the intrinsic spin Hall effect is stronger in the materials with more electronic bands connected by the spin-orbit coupling at the Fermi level[40].

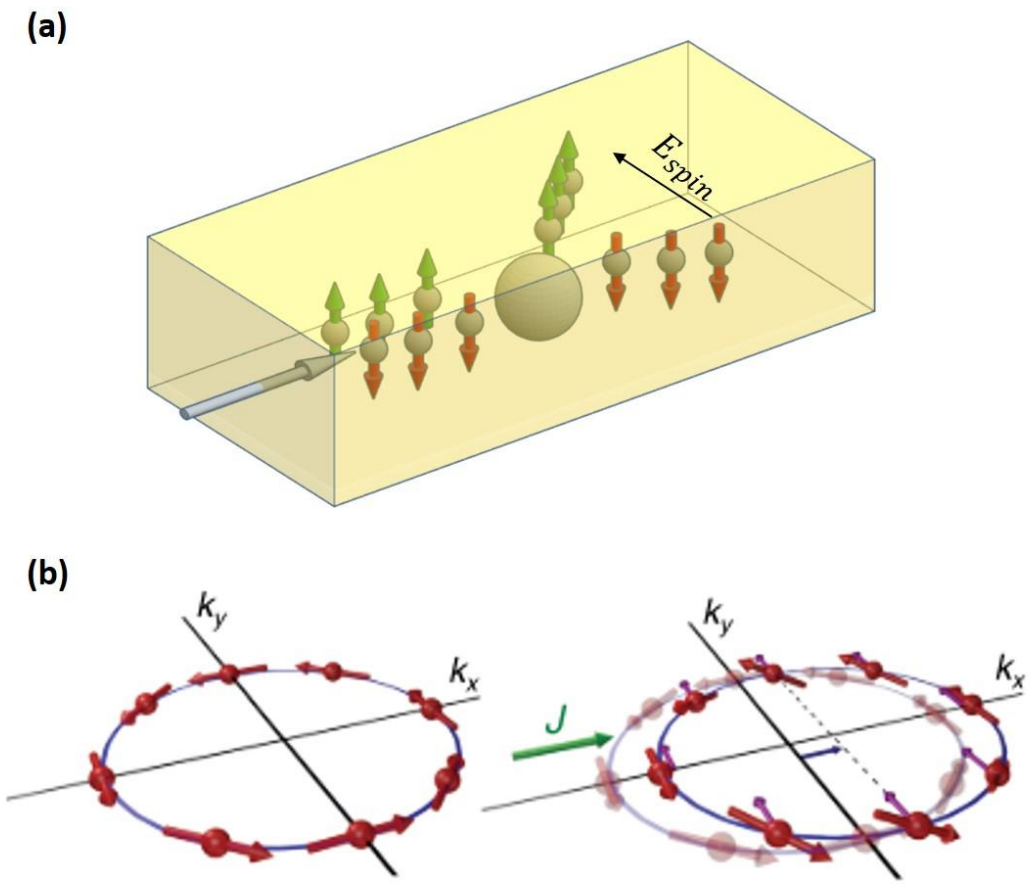

Figure 2.3 (a) Skew scattering where the interaction between the conduction elections and impurities leads to a transverse spin electric field E_{spin}. Here, the spin polarization of the electrons is set along the z direction, so the scattering occurs in the transverse direction. (b) Intrinsic mechanism for SHE (Picture from reference [27]). (left) An equilibrium spin texture with spins normal to the momentum at the Fermi surface. (right) With applying a charge current, the Fermi surface shifts in the same direction. The change in the momentum space induces an effect magnetic field that tries to align the spins back to their original positions. The tilting of spins turns out to be opposite at the opposite side of the Fermi surface.

2.1.2 Rashba effect

In Rashba effect[28,41], there exists an internal electric field $\boldsymbol{E}$ along the $\mathbf{z}$ direction at the broken-symmetry interfaces of the heavy metal/ ferromagnet/ oxide structures. As a charge current ($\boldsymbol{J_c} \parallel \boldsymbol{x}$) flows into the heavy metal, similar to the relativistic effects mentioned earlier in Equation 2.1, the electrons experience an effective magnetic field in the direction of $(\boldsymbol{v} \times \boldsymbol{E}) \,||\, \boldsymbol{y}$. This effective magnetic field is known as the Rashba effective field $\boldsymbol{H_R}$. The interaction energy between the electron's spin moment and the Rashba effective field can be written as $E_R = -\boldsymbol{\mu_s} \cdot \boldsymbol{H_R} \propto \boldsymbol{\sigma} \cdot (\boldsymbol{p} \times \boldsymbol{E})$, where $\boldsymbol{\sigma}$ is the spin angular momentum and $\boldsymbol{p}$ is the moving momentum of the conduction electrons. The result of the Rashba effect is that the magnetic spin moment is polarized towards the $\boldsymbol{y}$ direction at the interface, leading to a spin accumulation of a majority type of spin.

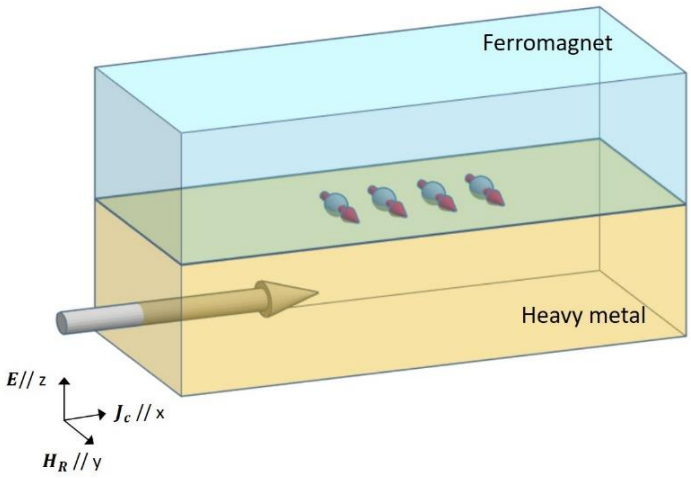

Figure 2.4 Rashba effect resulting in the spin accumulation at the interface.

2.2 Spin orbit torques

The spin current generated by the spin-orbit effects can be absorbed by a nearby ferromagnetic layer, interacts with the magnetic moment via exerting magnetic torques. Those torques are called spin-orbit torques (SOTs) so as to underline their direct relation to the spin-orbit interaction. Regardless of the source of the spin current (SHE or Rashba effect), the SOTs exerted on the magnetic moment consists of two orthogonal components: the field-like torque and the damping-like torque (or called the Slonczewski torque). The general form of the SOTs can be expressed as

$$\boldsymbol{T} = \tau_{FL}\boldsymbol{m} \times \boldsymbol{\sigma} + \tau_{DL}\boldsymbol{m} \times (\boldsymbol{m} \times \boldsymbol{\sigma}) \qquad \text{Equation 2.3}$$

where the first and second term on the right side features the field-like torque $\boldsymbol{T}_{FL}$ and damping-like torque $\boldsymbol{T}_{DL}$, respectively. $\boldsymbol{m}$ is the magnetization vector of the ferromagnet, $\boldsymbol{\sigma}$ is the spin polarization, and τ_{FL}, τ_{DL} are dimensionless values characterizing the contributions from $\boldsymbol{T}_{FL}$ and $\boldsymbol{T}_{DL}$. In our case, the spin polarization is in y direction. So Equation 2.3 can be rewritten as

$$\boldsymbol{T} = \tau_{FL}\boldsymbol{m} \times \boldsymbol{y} + \tau_{DL}\boldsymbol{m} \times (\boldsymbol{m} \times \boldsymbol{y}) \qquad \text{Equation 2.4}$$

Figure 2.5 depicts the relative orientations of the torques and magnetization.

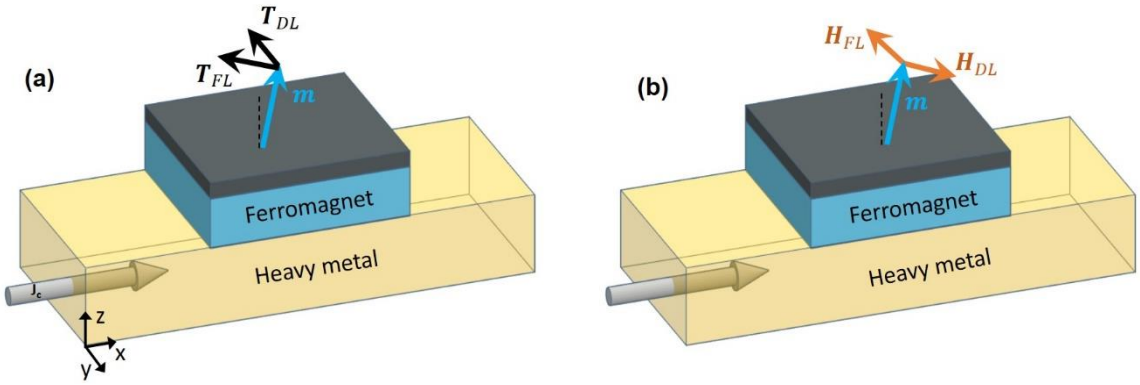

Figure 2.5 Relative configurations of (a) the damping-like torque $\boldsymbol{T_{DL}}$ and the field-like torques $\boldsymbol{T_{FL}}$ and (b) their effective magnetic fields.

As mentioned earlier, SOTs can result from the SHE and/or the Rashba effect, and these two effects often act simultaneously. Thus, it's hard to disentangle them from experiment results since the obtained data includes the combination of two effects. With this being mentioned, however, it's still useful to point out some key differences between them in order to gain more physical understanding that can be helpful for future material selection and device engineering in manipulating the SOTs.

The SHE-induced SOTs arise from the spin angular momentum transfer from the spin current to the magnetic moment. It resembles STT except that the spin polarizer is a non-magnetic heavy metal rather than a fixed-magnetization layer. In analogy to STT, the major component of the SHE-induced SOTs is the damping-like torque $\boldsymbol{T}_{DL}$. To extract $\boldsymbol{T}_{DL}$ (or τ_{DL}) experimentally, the ferromagnetic resonance (FMR) measurement can be performed to probe the change of the

damping constant due to the SHE-induced SOTs [18,19]. As mentioned above, one should treat it with caution because those experimental results can contain additional effects, including Rashba effect and other possible spin-orbit coupling[42,43]. Moreover, in order to model τ_{FL} and τ_{DL} in the case of SHE only, P.M.Haney, *et al*[44] proposed a simple drift-diffusion approach in the presence of spin-orbit coupling. It computes the spin current generated by the charge current in the heavy metal and propagates towards the ferromagnet. The spin accumulation at the heavy metal/ ferromagnet interface is characterized by the spin mixing conductance $G^{\uparrow\downarrow}$ and matches between the HM and FM. It's obtained that $\tau_{FL} \propto \theta_{SH} G_i^{\uparrow\downarrow}$ and $\tau_{DL} \propto \theta_{SH} G_r^{\uparrow\downarrow}$ where $G_i^{\uparrow\downarrow}, G_r^{\uparrow\downarrow}$ are the imaginary and real part of the spin mixing conductance $G^{\uparrow\downarrow}$.

Rashba effect, on the other hand, can be viewed as a phenomenon where a charge current gives rise to an effective in-plane magnetic field, the effective Rashba field $\boldsymbol{H}_{RE} \parallel \boldsymbol{y}$. It is analogous to the magnetic Oersted field generated by electric current. As a result, the dominant torque of Rashba effect is the field-like torque $\boldsymbol{T}_{FL}$ that makes the magnetization vector precess around the $\boldsymbol{H}_{RE}$. Furthermore, Rashba effect can only be induced in the systems that are lack of the inversion symmetry, such as the heavy metal/ferromagnet and ferromagnet/ oxide interfaces[28]. Some materials, like the antiferromagnetic GaMnAs, also have unit cell with broken inversion symmetry and thereby can induce the Rashba effect. It has been reported that Rashba effect SOTs can successfully the trigger magnetization switching in GaMnAs[45].

Figure 2.6 shows the numerical results of τ_{FL} and τ_{DL} in the case of pure SHE, pure Rashba effect and combined effects[44]. As can be seen, the major component of SOTs from pure SHE is the damping-like torque whereas pure Rashba results in SOTs primarily field-like. When both effects act in parallel, either damping-like or field-like torques can dominate, which depends on the selection of materials and thickness of the heavy metal and ferromagnet.

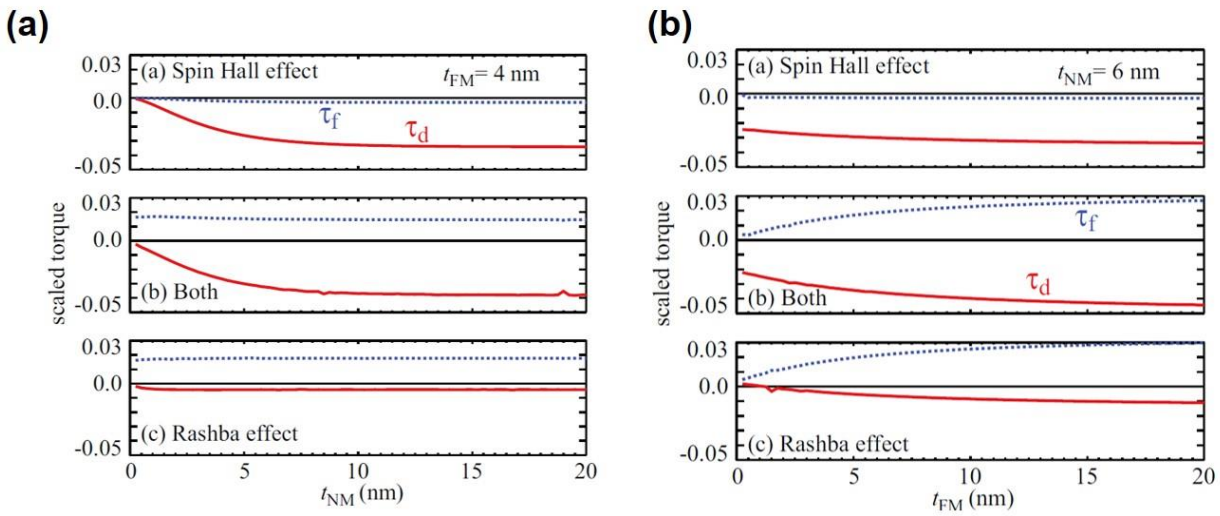

Figure 2.6 Modeling results showing the magnitude of damping-like torque (red line) and field-like torque (blue line) as the function of (a) heavy metal thickness and (b) ferromagnet thickness. Picture from reference [44].

Equivalently, the torques described above can be regarded as the effective magnetic fields $\boldsymbol{H}_{FL} = \tau_{FL}\boldsymbol{y}$ and $\boldsymbol{H}_{DL} = \tau_{DL}\boldsymbol{m} \times \boldsymbol{y}$, as illustrated in Figure 2.5(b). Thus, Equation 2.4 can be subsequently expressed as

$$\boldsymbol{T} = \boldsymbol{m} \times \boldsymbol{H}_{FL} + \boldsymbol{m} \times \boldsymbol{H}_{DL} \qquad \text{Equation 2.5}$$

The purpose of the introducing effective magnetic fields is that they can be directly analyzed in parallel with the external magnetic field $\boldsymbol{H}_{ex}$ applied in the experiments. Such formulation turns out to be convenient when dealing with the SOT-driven magnetization switching and domain wall motion in the presence of $\boldsymbol{H}_{ex}$, as will be discussed in the following sections.

2.3 SOT driven magnetization switching

In this section, we discuss the mechanisms of the SOT-driven magnetization switching in three major types of devices depending on the direction of the easy axis of the ferromagnetic layer. As shown in Figure 2.6, the magnetic easy axis of the ferromagnet can point in x, y or z direction (namely, referred to as the type-x, -y or -z device) by controlling the geometry of the device and/or the thickness of the magnetic layer.

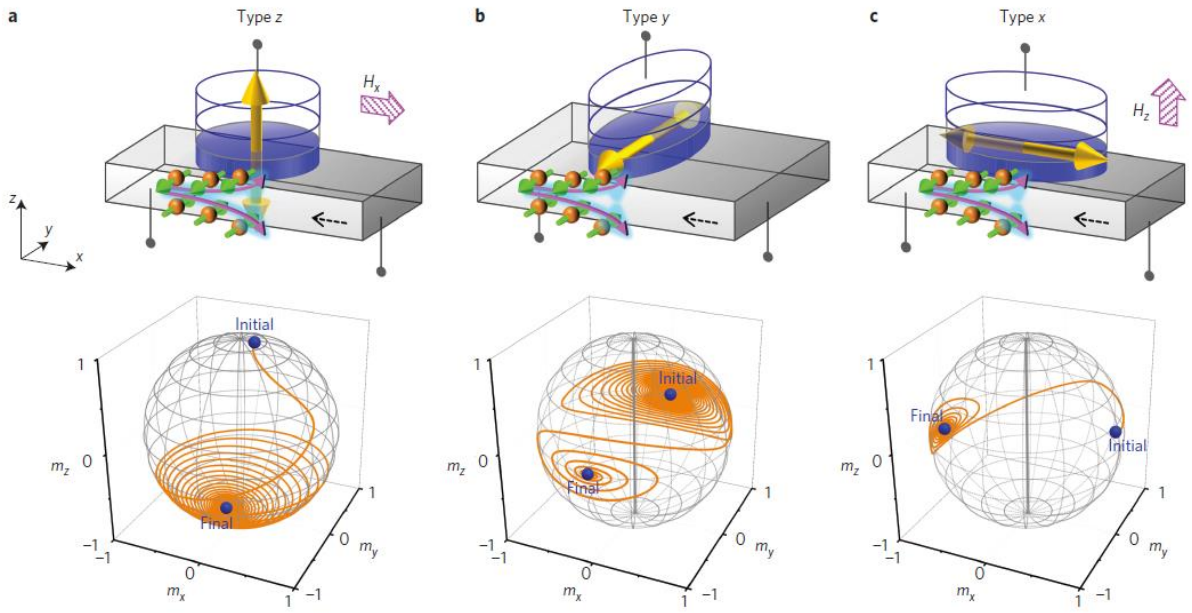

Figure 2.7 Top panel: illustrations of (a) the type-z device, (b) the type-y device and (c) the type-x device. Bottom panel: magnetization trajectories during switching from macrospin simulations. Picture from reference [31].

We showed that the damping-like torque $\boldsymbol{T}_{DL}$ generated by the SHE (and the Rashba effect) lie in the film plane parallel to the y axis. $\boldsymbol{T}_{DL}$ being in $+y$ or $-y$ direction can be controlled by the polarity of the applied current. Hence, it's naturally capable of driving the magnetization reversal of the type-y devices via direct spin angular momentum transfer, without any assistance from external field or other torques. The SOT switching in type-y devices was demonstrated by LQ. Liu (2012)[19] and CF. Pai (2012)[20] by utilizing the SHE of Ta and W. The switching process resembles the STT switching scheme of an in-plane magnet, and thus the critical current density for switching is given by[19]:

$$J_c^* = \frac{2e}{\bar{h}} \frac{M_S t \alpha}{\theta_{SH}} \left(H_C + \frac{H_{eff}^{out}}{2}\right) \qquad \text{Equation 2.6}$$

where $\bar{h}$ is the Dirac constant, M_s is the saturation magnetization, t is the thickness of the magnetic layer, α is Gilbert damping constant, θ_{SH} is the spin Hall angle, H_C is the in-plane coercive field and H_{eff}^{out} is the out-of-plane anisotropy field.

For type-z devices, however, the switching process turn out to be more complex because the spin polarization $\boldsymbol{\sigma}$ is orthogonal to the easy axis. For convenience, let's analyze the switching

scheme in the effective field formulation. First, we have the effective field-like field $\boldsymbol{H}_{FL} = \tau_{FL}\boldsymbol{y}$ lying along the y direction. $\boldsymbol{H}_{FL}$ can tilt the magnetization towards the y-axis upon applying the current pulse. Then the magnetization relaxes back to the easy axis position due to the perpendicular magnetic anisotropy. The returning to up or down state is a stochastic process rather than a deterministic process, so $\boldsymbol{H}_{FL}$ is not able to determine the magnetization state between $+z$ and $-z$ direction. The effective damping-like field $\boldsymbol{H}_{DL} = \tau_{DL}\boldsymbol{m} \times \boldsymbol{y}$, on the other hand, is always orthogonal to the magnetization regardless of the magnetization direction. It may rotate the magnetic moment from up to down state (if $\boldsymbol{H}_{DL}$ is large enough), but then also be able to let the magnetic moment return back to the original up state. In other words, the up and down magnetization states are equally energetically favorable under $\boldsymbol{H}_{DL}$, which is the consequence of the symmetric configuration of up and down states with respect to the transverse spin polarization $\boldsymbol{\sigma}$. Hence, the symmetry must be broken in order to realize the deterministic switching. A common way to achieve it is to apply an external magnetic field $\boldsymbol{H}_x$ along the current direction, as shown in Figure 2.8. Now when $\boldsymbol{H}_x$ is parallel to $\boldsymbol{H}_{DL}$, they both tend to tilt the magnetization away from its original orientation. The magnetization state won't be stable until it's rotated to the position where $\boldsymbol{H}_x$ and $\boldsymbol{H}_{DL}$ are compensated (antiparallel). In Figure 2.8(b), when both the current and $\boldsymbol{H}_x$ are applied along the +x direction, $\boldsymbol{H}_{DL}$ is anti-aligned with $\boldsymbol{H}_x$ at down state and therefore down state is more favorable than the up state. Changing the current polarity will give $\boldsymbol{H}_{DL}$ in opposite direction, and accordingly, the up state will become more favorable. In such way, the bipolar switching can be obtained with the assistance of $\boldsymbol{H}_x$. In addition, an opposite $\boldsymbol{H}_x$ can also lead to a reversed switching outcome. In other words, the favorable magnetization state is determined by the relative orientation of the charge current and $\boldsymbol{H}_x$. For types-z devices, the critical current density for switching is given by[46]

$$J_C^* = \frac{2e}{\hbar}\frac{M_S t}{\theta_{SH}}\left(\frac{H_K}{2} - \frac{H_x}{\sqrt{2}}\right) \qquad \text{Equation 2.7}$$

where H_K is the effective anisotropy field of the ferromagnet.

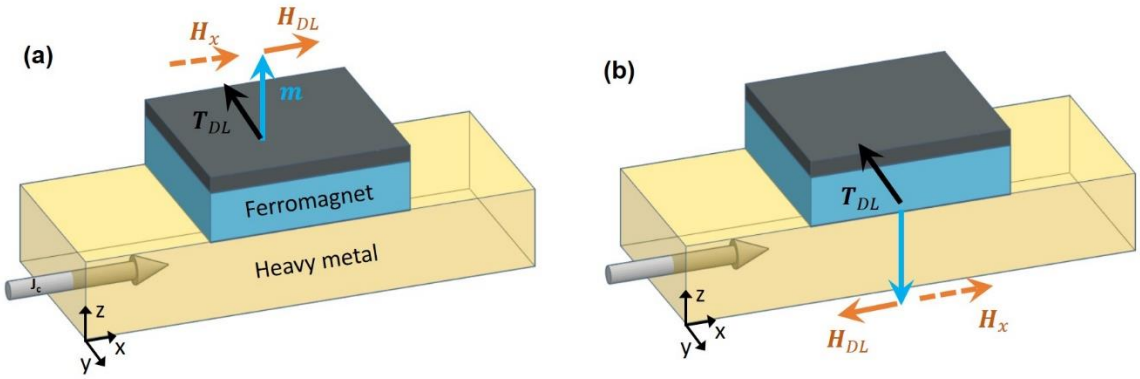

Figure 2.8 Relative orientations of $\boldsymbol{H}_{DL}$, $\boldsymbol{T}_{DL}$ with (a) up- and (b) down-magnetization. If ignoring the external field $\boldsymbol{H}_x$, the up and down states are symmetric with respect to $\boldsymbol{T}_{DL}$ and thus they are identically energetically favorable. Introducing $\boldsymbol{H}_x$ breaks the symmetry and, in this case, makes down-magnetization more favorable.

The switching dynamics of type-x device is analogous to that of type-z device that a perpendicular external field H_z is necessary for breaking the symmetry in order to achieve the deterministic switching.

Figure 2.7 also shows the trajectories of magnetization during the switching process. For type-y devices, the magnetization first precess a lot around its original state upon the exertion of the torque, then flips to the desired direction. But for type-z and type-x devices, the magnetization changes polarity instantly as the torques are exerted. This implies type-z and type-x devices may be more desirable in terms of faster switching speed, although an external field is needed to assist the switching. Experimental evidence shows that type-z device can reach the writing speed of few hundreds of picoseconds[33,47] whereas type-y device usually has the writing speed in the range of few nanoseconds[48].

By far, it looks like that the field-like torque (or the effective field-like field) does not participate in the switching process. This statement holds for the type-y devices because the switching mainly follows the STT switching scheme. But it's not true for the switching in the type-z and type-x devices. S. Fukami[31] conducted macrospin simulations for these two types of devices, and showed that the field-like torque actually plays a role in altering the magnetization trajectory during switching, which makes the switching process become more efficient. The

simulation results suggest that the existence of the field-like torque reduces the critical current density needed for the switching significantly, by a factor of more than 3.

2.4 Choice of device geometry for practical applications

Different from type-z and type-x devices, type-y device can be directly switched by current-induced SOTs without an externally applied field, which may appear to be a good choice for real applications. One issue for type-y devices, however, is that the switching speed is slower than the other two devices, which can limit the use for the ultra-fast switching spintronic devices. The other issue, which hinders type-y devices from being widely adopted, lies in low thermal stability as the size of the devices gets small. To determine whether the magnetization of a device would be thermally stable for long enough time (namely, whether the information can be stably stored), the thermal stability factor $\Delta = K_{eff}V/k_bT$ is often used, where K_{eff} is the effective anisotropy, V is the volume of the magnet, k_b is the Boltzmann's constant and T is the temperature. Usually devices with stable magnetization > 10 years require $\Delta > 40$. As the device size becomes smaller, Δ decreases due to reduced volume of the magnetic layer. For type-y devices, K_{eff} primarily comes from the shape anisotropy determined by the device geometry. But the shape anisotropy is often not large enough to support $\Delta > 40$, leading to poor data retention in the type-y devices. Additionally, the geometry of the device determining the shape anisotropy becomes harder to control in the device fabrication when the device size gets down to tens of nanometers.

The type-z device stands out for the better thermal stability resulting from the high perpendicular magnetic anisotropy at the material interfaces[49] or from the crystal lattice[50]. The large interfacial perpendicular anisotropy in perpendicular MTJs is able to give Δ=85 for sub-50 nm device[51], sufficient for keeping the information thermally stable for a long time. With the thermal stability issue solved, another critical aspect to make type-z devices viable for commercialization is to eliminate the need for applying an external field. To achieve zero-field switching, people have come up with several tricks. One approach is by creating geometric asymmetry, for instance, by making a wedge structure of the ferromagnetic layer, so that the effective field associated with the SOTs could contain some perpendicular components[52,53]. But this approach suffers the scalability issue because the geometry becomes more difficult to control as the device size become smaller, which diminishes the advantage of the type-z device in scaling

down. Another way in the field-free SOT switching is via introducing a local in-plane field by exchange bias or interlayer exchange coupling. It has been reported that an antiferromagnetic layer, such as PtMn[23] and IrMn[21,22], is able to generate spin current as well as add a horizontal field to the neighbor perpendicularly magnetized layer by exchange bias so as to assist the switching. An interesting phenomenon in this scheme is that the magnetization changes in an analogue manner with increasing magnitude of the current. Such behavior opens a new direction for potential memristive applications. The detailed mechanisms, however, is not fully understood including SHE of antiferromagnetic materials as well as the origins of the analogue behavior. YC Lau *et al*.[54] obtained field-free perpendicular magnetization reversal by introducing an effective in-plane field via interlayer exchange coupling with an in-plane magnetized layer. The magnitude as well as the polarity of effective in-plane field can be adjusted by tuning the thickness of the exchange coupling layer (in this case, the Ru spacer layer). But one major issue of this approach is that one cannot further integrate magnetoresistive stacks because the exchange coupling layer and spin Hall layer are separated, which greatly limits its usage for practical applications.

2.5 Domain wall motion

Till now we have only analyzed the magnetization switching in the single domain model. The switching dynamics can be explained by the schemes demonstrated above if the size of devices is less than the width of domain wall (DW). But in many cases, the device size ranges from hundreds of nanometers to μms so that the device can contain multiple magnetic domains. Instead of switching via spin precession and rotation, the magnetization reversal in those devices is more likely to takes place by nucleation and expansion of reversed domains. Since SOTs can effectively drive the motion of DWs, here we would also like to discuss the mechanisms accounting for the SOT-driven domain wall motion (DWM).

Before digging into the details of DWM, let's first introduce another spin-orbit effect that plays a critical role in enabling SOT-driven DWM in perpendicularly magnetized systems, which is the so-called Dzyaloshinskii-Moriya interaction (DMI). DMI refers to the asymmetric exchange coupling between two neighbor spins, and its associated energy is given by

$$E_{DMI} = \boldsymbol{D}_{ij} \cdot (\boldsymbol{S_i} \times \boldsymbol{S_j}) \qquad \text{Equation 2.8}$$

where $\boldsymbol{D}$ is the DMI vector. Notice that Equation 2.8 looks similar to the Heisenberg exchange interaction $E_{ex} = J \cdot (\boldsymbol{S_i} \cdot \boldsymbol{S_j})$ where J is the Heisenberg exchange constant. There are two major differences between DMI and Heisenberg exchange interaction. The first is that $\boldsymbol{D}$ is a vector in DMI whereas J is a dimensionless value. So in the crystals with inversion symmetry, DMIs cancel with each other between the inversion-symmetric locations because the DMI vectors have opposite signs. Therefore, the necessary condition for the existence of DMI is that the system must have broken inversion symmetry. The interface between two dissimilar materials naturally satisfies this condition. The second difference is that Heisenberg exchange interaction favors parallel or antiparallel spin configurations depending on the sign of J whereas DMI results in neighbor spins being canted with each other. Although the strength of DMI is relatively small compared with Heisenberg exchange interaction, experimental evidence shows that DMI can effectively determine the DW structure in perpendicularly magnetized heavy metal/ferromagnet/oxide heterostructure, such as Pt/ Co/ AlO_x[55,56], W/ FeCoB/ MgO[57] and Ta/ FeCoB/ MgO stacks[58]. In particular, the DMI is capable of stabilizing the Neel-type DWs with a given chirality (right- or left-hand) over the Bloch-type DWs. A simple way to picture it is that the DMI generates an effective magnetic field $\boldsymbol{H}_{DMI}$ normal to the DW, and the interaction between $\boldsymbol{H}_{DMI}$ and the DW magnetization makes the Neel-type DWs become more energetically favorable than Bloch-type DWs. The chirality of Neel-type DWs is determined by the sign of $\boldsymbol{D}$ (or the direction of $\boldsymbol{H}_{DMI}$), which can be controlled by the engineering the interfaces.

To see why the existence of DMI, especially the stabilized Neel-type DWs, is critical for the SOT-driven DWM, we shall analyze how the SOTs act on the DW magnetization. In general, to get DWs to move, the effective fields associated with SOTs must be aligned along the domain magnetization (either up or down). Figure 2.9 schematically shows the cross section of the two types of DWs in a perpendicular magnetic strip. Let's first examine the effect of the field-like torque $\boldsymbol{T}_{FL}$. The associated effective field $\boldsymbol{H}_{FL}$, as introduced earlier, always points along the y direction, which does not align with any of the domain magnetization (up or down). So it's not able to induce DWM regardless of the type of DWs. For the damping-like torque, it turns out to have different effects depending on the DW structure. For Neel-type DWs, the effective damping-like field acting on the center DW magnetization is $\boldsymbol{H}_{DL} \propto \boldsymbol{m} \times \boldsymbol{y} = \boldsymbol{x} \times \boldsymbol{y}$ that's in the perpendicular direction. Consequently, it will rotate the DW magnetization and drive the DW to

move away from the domain whose magnetization is aligned with $\boldsymbol{H}_{DL}$, so that the aligned domain expands. In this case, the damping-like field effectively triggers the movement of Neel-type DWs. For Bloch-type DWs, however, the effective field on the center DW magnetization $\boldsymbol{H}_{DL} \propto \boldsymbol{y} \times \boldsymbol{y}$ should be zero and thus can't induce any DWM. In other words, SOT-driven DWM only occurs with the DWs having the Neel-type structure.

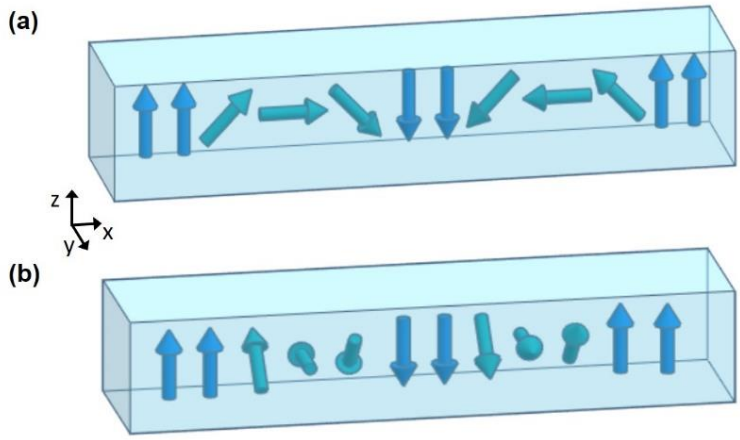

Figure 2.9 The two types of DW in perpendicular thin films. (a) the Neel-type DW, shown with the right-handed chirality. (b) the Bloch-type DW.

One important characteristic of the DMI-stabilized Neel walls is that all DWs have the identical chirality within a given material system. It means that the up-down DW and down-up DW will have the center DW magnetization pointing in opposite directions so that their DW chirality is the same. An example is shown in Figure 2.9(a). The consequence is that, due to the fixed chiral structure, the SOTs drive all the DWs within a magnetic strip along the same direction regardless of the up-down or down-up forms. Accordingly, since the two DWs surrounding an opposite domain travel in the same direction, what we should observe in the SOT-DWM experiment is that the opposite domain shifts its position in the direction of DWM while the size of the domain remains unchanged[58,59]. Furthermore, we notice that the direction of DWM is determined by the driving force $\boldsymbol{H}_{DL}$ whose direction is defined by the cross product of spin polarization $\boldsymbol{\sigma}$ and DW magnetization. We know that $\boldsymbol{\sigma}$ and the DW structure are governed by the SHE and DMI, respectively. Thus, to control the direction of DWM within a magnetic strip, either same as or against the direction of applied current, we can select the heavy metals with different

the sign of spin Hall angles (positive or negative) or manipulate the DMI by engineering the interface. A brief summary of the direction of DWM resulting from different combinations of spin Hall angle and DW chirality is listed in Table 2.1.

Table 2.1 Survey of the direction of DWM with different combinations of heavy metal and ferromagnet materials

Heavy metal	Spin Hall angle	Ferromagnet	DW chirality	DWM direction
Pt	0.07	FeCoB[58], Co[60], Co/Ni[55,56]	Left-handed	Same as current
W	-0.03	FeCoB[57]	Right-handed	Same as current
Ta	-0.15	FeCoB[57,58]	Left-handed	Against current
Hf	-0.2	FeCoB[57]	Left-handed	Against current

We mentioned that the SOTs drive the DWs in the same direction and cause domain shifting if all DWs are within the magnetic strip. But if one just traps a single DW within the strip, the magnetization reversal of the strip can be obtained via SOT-driven DWM. In this case, the DW device is patterned so that it consists a center wire with two large pads on the sides (Figure 3.9). An opposite domain is initiated within the pad region by an external field or current-induced oersted field. Then the opposite domain expands by the external field so that only one DW is pushed into the wire. After that, charge current pulses are applied into the device. Because the wire is much narrower that the side pad, only the current density within the wire is above the threshold to induce the SOT-DWM. As such, the magnetization state of the wire can be controlled by moving the DW from one side to the other. Beside the full magnetization reversal, different magnetization stages can be achieved with positioning the DW at different locations along the wire, which is useful for logic and neuromorphic computing[61–63].

2.6 Applications and devices

The benefits of low power and ultra-fast operation speed of SOT switching encourage people to design and develop novel memory and logic architectures. Three-terminal devices with in-plane MTJs of the type-*y* geometry was first demonstrated by LQ. Liu(2012)[19] and afterwards, M. Cubukcu(2014)[64] incorporated perpendicular MTJs where the switching of the free layer is assisted by an external in-plane field. The write path in these devices is usually a heavy metal layer with large spin Hall angle, such as Ta or W, which allows low operation power consumption down

to 300 pJ as well as ultra-fast reversal time down to 210 ps in state-of-art SOT-MRAM (by Imec, see https://www.imec-int.com/en/articles/imec-demonstrates-manufacturability-of-state-of-the-art-spin-orbit-torque-mram-devices-on-300mm-si-wafers). On the other hand, adopting the topological insulator as the writing layer[26,65], although it's still in the preliminary research stage, shows stunningly giant spin Hall angle (up to 52.2) and thus has potentials in further lowering the critical current density. Nevertheless, such high performance of SOT switching makes SOT-MRAM competitive to STT-MRAM and viable to replace low-level caches. Analysis of hybridization of SOT-MRAM with SRAM also shows significant reduction in power consumption and moderate improvement in areal density as well as performance[66].

In addition, SOT-driven DWM also gives rise to some smart device designs. One of the well-known examples is the racetrack memory proposed by IBM[67]. In the racetrack memory, information is stored in a series of magnetic DWs within a nanostrip. Writing the information is simply by moving the DWs via injecting short current pulses into the nanostrip. The velocity of DWM in the stack designated for racetrack memory has been shown capable of approaching nearly 1000 m/s[68]. Future development for racetrack memory includes efficient method in detecting DWs and packing denser DWs with high thermal stability.

On the other hand, our group [69,70] proposed a novel four terminal DW device, called mCell, for nonvolatile logic computing. As shown in Fig. 2.8(d), the write-path of mCell consists of a heavy metal layer and a neighbor perpendicular magnetic layer with a trapped domain. A pulse current is used to generate SHE SOTs and thus move the DW to switch the magnetic state. The read path contains an MTJ with a top reference layer and a bottom free layer. The free layer of the read path needs to be magnetically coupled to the write-path such that the switch of write path via current-induced DWM will reverse the magnetization orientation of the free layer. Meanwhile, the interlayer between the write- and read-paths is designed to be electric insulating to prevent mixing of writing and reading current. Such magnetic-coupling electric-insulating interlayer can be a magnetic oxide whose experimental development will be demonstrated in Chapter 8.

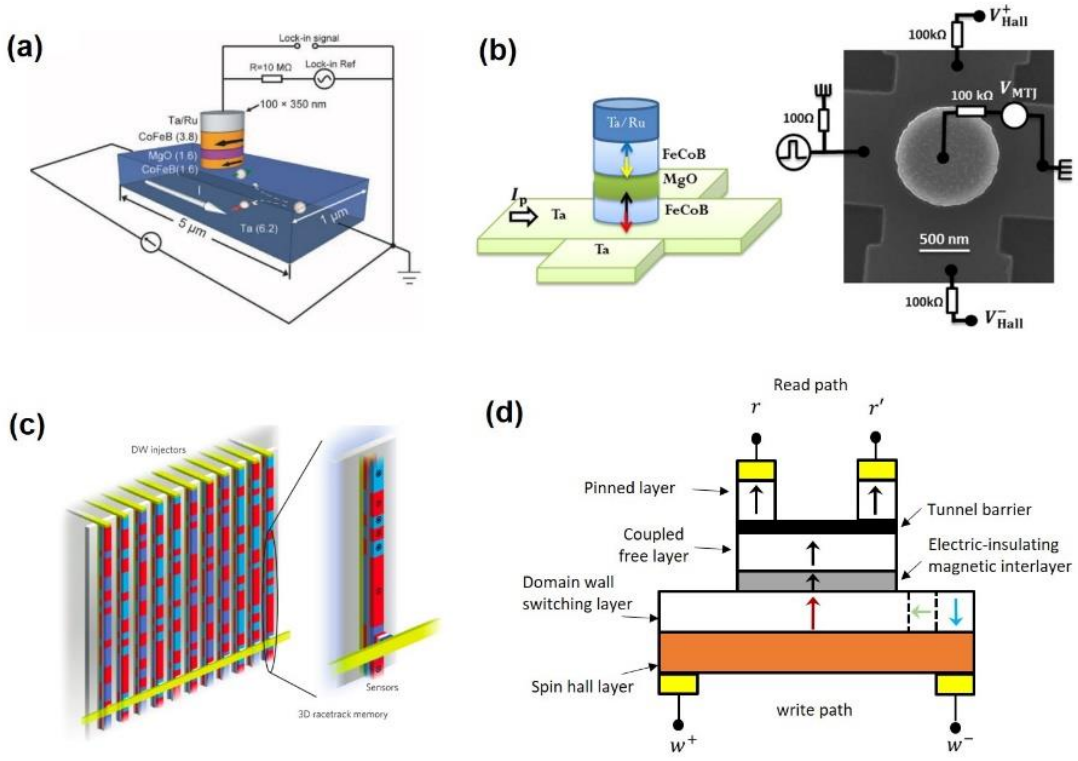

Figure 2.10 Examples of the SOT devices. (a) Three-terminal device with the in-plane MTJ, by LQ. Liu, *et al*. (2012)[19]. (2) Three-terminal device with the p-MTJ, from M. Cubukcu, *et al*. (2014)[64]. (c) Racetrack memory, from IBM[67]. (d) mCell by JG. Zhu[69,70].

Chapter 3
Experimental methods

In this chapter, we present the experimental methods in fabricating and testing the SOT devices. The fabrication of nanoscale devices includes a wide variety of nanofabrication techniques such as film deposition, ion beam etching, reactive ion etching, photolithography, and e-beam lithography. All fabrication recipes are developed at CMU, and haven been proven to be reliable and repeatable after many patterning cycles. The characterizations involve the evaluations of the magnetic property, structural property as well as electrical property.

3.1 Film and device fabrication

3.1.1 Film deposition

All films used in our experiments are deposited by a physical vapor deposition technique called magnetron sputtering. In the magnetron sputtering process, the sputtering chamber is first pumped down to low pressure from 10^{-7} to 10^{-9} mTorr and then an inert gas, such as Ar gas, is introduced into the chamber at pressure in mTorr range. Next, a bias voltage is applied between target (cathode) and substrate (anode), which ionizes Ar atoms thus generating a plasma consisting of ions and electrons. Electrons are accelerated towards the anode, during which they collide with other Ar atoms and so more ions and electrons are generated to sustain plasma. On the other hand, Ar ions are accelerated towards the target (cathode) and bombard with it. Such bombardment releases target atoms all over the chamber, some of which are deposited on the substrate thus forming a thin film. One distinguished feature of magnetron sputtering is that there are magnets underneath the target. The magnetic flux from these magnets causes electrons to travel in spiral trajectory as well as concentrates them near the target. The advantages are that (1) electrons could

travel in longer distance to get more Ar atoms ionized so that plasma is more stable and (2) plasma is confined close to the target thus having higher sputtering efficiency. Depending on the power supply used, the sputtering can be classified into DC or RF sputtering. DC sputtering is the simplest method that's commonly used to sputter conductive materials such as metals. For sputtering insulators, however, DC sputtering can cause positive charges to build up on the target surface and thus prevent further knocking off target atoms. Therefore, RF sputtering is used for insulators where positive and negative voltages are switched at MHz frequency to avoid charge built-up on the target surface.

Most of our film depositions are done in the AJA 8-target sputtering system and the Nanofab sputtering systems. Table 3.1 lists the sputtering parameters for the various materials used in our work.

Table 3.1 Sputtering conditions for the materials used in our experiments.

Material	Power type	Power	Gas & Pressure	Deposition rate	Tool
Ta	DC	50 W	Ar, 1.5 mT	0.04 nm/s	AJA 8-target sputtering system
W	DC	15 W	Ar, 7 mT	0.011 nm/s	AJA 8-target sputtering system
Ir	DC	25 W	Ar, 3 mT	0.02 nm/s	AJA 8-target sputtering system
Pt	DC	25 W	Ar, 3 mT	0.035 nm/s	AJA 8-target sputtering system
Ru	DC	25 W	Ar, 3 mT	0.018 nm/s	AJA 8-target sputtering system
FeCoB	DC	100 W	Ar, 3 mT	0.031 nm/s	AJA 8-target sputtering system
Mn	DC	50 W	Ar, 3 mT	0.037 nm/s	AJA 8-target sputtering system
Fe	DC	50 W	Ar, 5 mT	0.024 nm/s	AJA 8-target sputtering system
Co	DC	50 W	Ar, 5 mT	0.019 nm/s	AJA 8-target sputtering system
Ni	DC	50 W	Ar, 5 mT	0.028 nm/s	AJA 8-target sputtering system
MgO	RF	120 W	Ar, 10 mT	0.015 nm/s	AJA 8-target sputtering system
Fe_3O_4	RF	150 W	Ar, 10 mT	0.004 nm/s	AJA 8-target sputtering system
C	DC	150 W	Ar, 5 mT	0.039 nm/s	Nanofab sputtering system #4
SiN	RF	300 W	2 Ar:1 N_2, 5 mT	0.065 nm/s	Nanofab sputtering system #4
Ti	DC	50 W	Ar, 2.5 mT	0.119 nm/s	Nanofab sputtering system #1
Au	DC	25 W	Ar, 2.5 mT	0.267 nm/s	Nanofab sputtering system #1

3.1.2 Nanopillar device fabrication

Here we show the nanopillar device fabrication recipe developed at CMU. This recipe can be used to fabricate nanopillar devices including the three-terminal SOT device and two-terminal STT/oscillator devices. To best of our knowledge, this recipe has been used for years by our group

and turns out to be an efficient and robust process based on CMU's facility. Figure 3.1 illustrates the process flow. The major steps associated with the recipe are as following:

(a) deposit magnetic and non-magnetic films, then deposit C/ SiN hard mask,
(b) electron-beam lithography (e-beam) defines HSQ nanopillars, followed by reactive ion etching (RIE) to etch through the hard mask, then ion milling to etch the metallic layers,
(c) lithographically pattern the bottom electrode, ion milling to etch into the substrate,
(d) deposit a SiN passivation layer
(e) low-angle ion mill to planarize the chip
(f) etch SiN so that C is exposed,
(g) etch C to open the top window,
(h) open the bottom windows by lithography and SiN etching,
(i) fabricate top electrodes to make the contact.

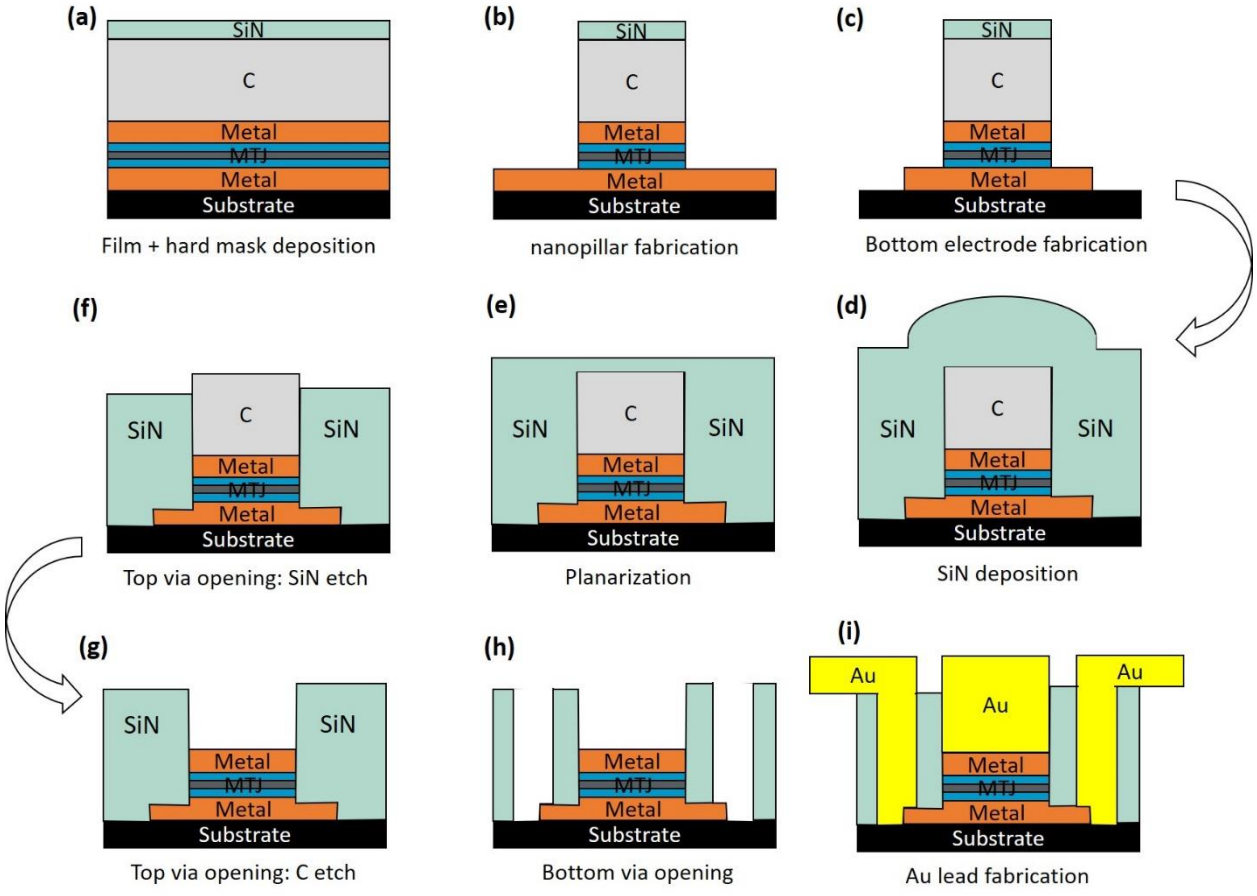

Figure 3.1 Process flow of the nanopillar device fabrication.

In step (a), multilayers of magnetic and non-magnetic films are deposited at room temperature by magnetron sputtering on Si substrate with thermally grown oxide. Next, a hard mask consisting of 60 nm C/ 5 nm SiN is deposited. The hybrid hard mask is chosen for two reasons: (1) they have much lower milling rated compared with the metallic films so they can be used to define the nanopillar during the ion milling, and (2) C and SiN can be selectively etched in RIE, which will be critical in opening the top window.

Because the nanopillar we fabricate often has the size smaller than 200 nm, e-beam lithography with negative resist HSQ is used to pattern the nanopillar. Here, HSQ is a high-resolution resist and it converts into SiO_2 after exposure. After HSQ pillar is defined, RIE with CH_4/CHF_3 gas is used to etch away the thin SiN layer, and then RIE with O_2 gas to over-etch the C layer. In this way, we create a C/ SiN/ HSQ milling mask. Some sample images of the milling mask are shown in Figure 3.2(a). Note that to prevent oxidation of the metallic stack during the C etching, a Pt capping layer is recommended for the metallic stack. Ru capping can also be used. Next, we transfer the pattern into the metallic layers by ion milling. To ensure the etching stops right at the desired layer, the in-situ secondary ion mass spectroscopy (SIMS) system is used for end-point detection. During the etching, the flux of etched materials can be generated at different angles and some of them will be re-deposited onto the sidewall of the nanopillars. The re-deposition will eventually short the nanopillar device, especially for MTJ devices. So it's critical to clean the re-deposition after pillar etching. Hence, after etching to the bottom electrode, we use grazing-angle milling so that most of the ion beam bombard the side wall to etch away the redeposited materials. Figure 3.2(b) shows the fabricated pillars. The diameters of the final pillars are found to be 10-20% larger than the ones of the C/ SiN/ HSQ milling masks, which is caused by tilted angle etching in ion milling. The pillar height t_{pillar} is recorded. The parameters used in step (b) are listed in Table 3.2.

The photolithography tool at CMU has the resolution limited to 2 μm. So in step (c), if the design of the bottom electrode has the width larger than 2 μm, we use photolithography with AZ 4210 resist to pattern the bottom electrode; otherwise we use e-beam lithography with maN 2405 resist for narrower bottom electrode. Ion milling is then to etch away all materials except for the materials below the resist so that the bottom electrode will be patterned.

After stripping the resist, a passive SiN layer of thickness t_{SiN} = 120 nm-150 nm is deposited. To planarize the chip, we use grazing-angle ion milling that can flatten the top surface of the nanopillar. The planarization time ranges from 15 min – 25 min depending on the pillar height t_{pillar}. Taller pillars often require longer time for desired planarization. Figure 3.3(a) shows the device surface after planarization. The etching rate of SiN at 85^0 grazing angle is about 2 nm/min. The thickness of etched SiN Δ_{SiN} can be calculated by ($etching\ rate\ \times\ etching\ time$).

In step (f), to open the top window, we first etch the SiN so that the C on top of the pillar will be exposed. This SiN etching step needs to be controlled carefully because it is critical to the success in opening the top window. Under-etch will cause inaccessible top window that eventually leads to the open device while over-etch will expose the side wall of the pillars and results in device shorting. To our experience, the SiN thickness to be etched that gives the best yield can be calculated from $\Delta_{SiN}' = t_{SiN} - t_{pillar} - \Delta_{SiN} + 20$ (nm). The last term is an additional 20 nm margin to ensure that the C is exposed. After that, we use RIE with O_2 gas to etch away all the remaining C sitting on the metallic pillar, as shown in step (g). Figure 3.3(b) shows a properly opened top window surrounded by a bright ring. The bright ring corresponds to the SiN that's higher than the other part due to the previous imperfect planarization.

Next, we open the bottom windows via photolithography with AZ4110 resist followed by SiN etch in RIE. After cleaning the resist, the final steps are to pattern the top electrodes by photolithography with AZ 4210, Ti/Au deposition and lift-off. Figure 3.4 shows the sample image of a fabricated three-terminal MTJ device.

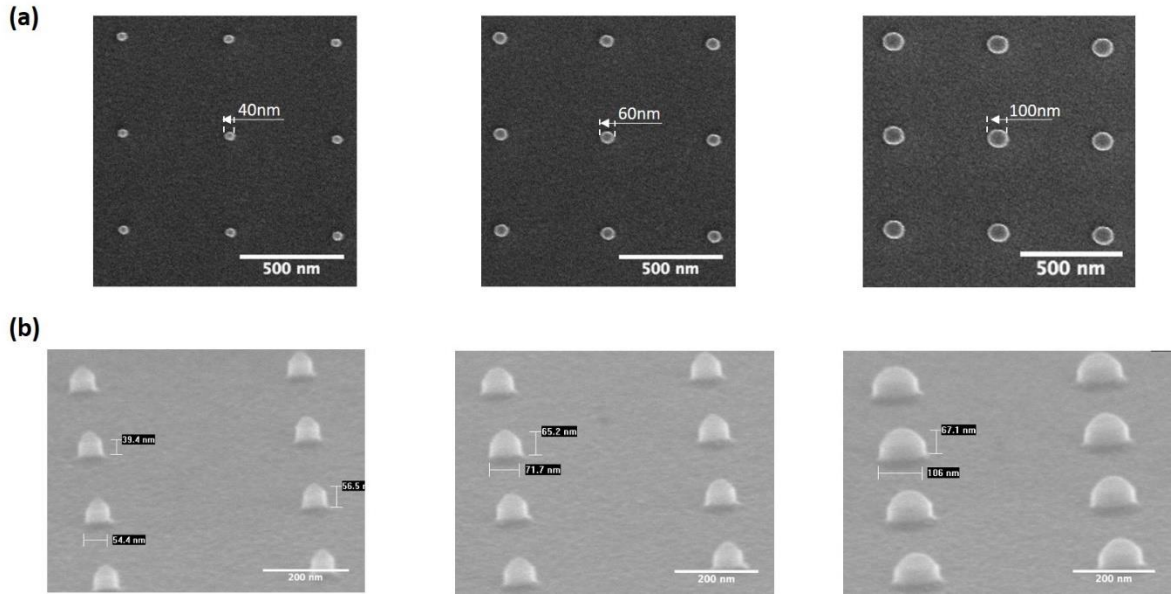

Figure 3.2 SEM images: (a) top view of the 60 nm C/5 nm SiN/ HSQ milling mask and (b) titled angle view of the nanopillars after ion milling.

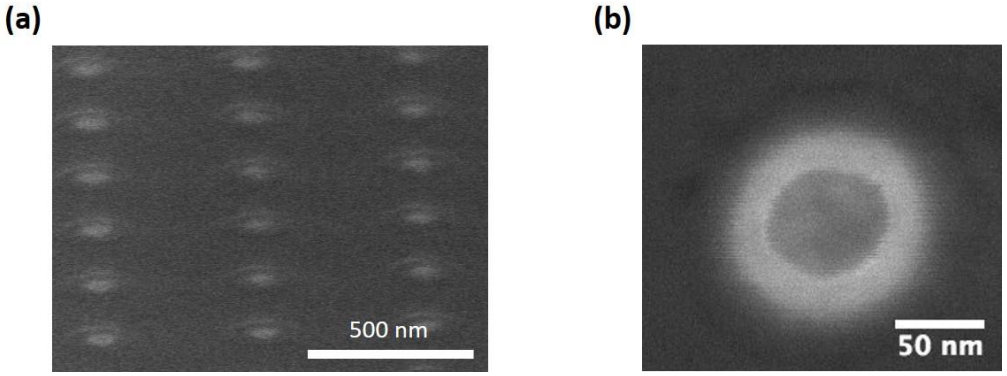

Figure 3.3 (a) The surface of the nanopillar device after planarization. (b) A properly opened top window.

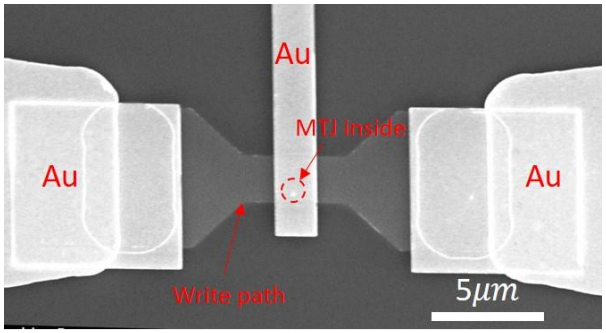

Figure 3.4 SEM image of a fabricated three-terminal MTJ device

Table 3.2 Parameters used in step (b)

Process	Parameters	Tool
E-beam lithography defining HSQ pillar	Resist: HSQ Spin coat: • dynamic dispensing: 1000 rpm, 6s • spreading: 4000 rpm, 45s Baking: 190 ^{0}C, 1 min Exposure: • beam condition: 100 kV, 1nA • pillar dose: 7000 μC/cm^2 • alignment mark dose: 2000 μC/cm^2 Develop: • developer: MF CD-26 • time: 50 s	Elionix ELS-G100 Electron Beam Lithography System
Hard mask etching	SiN etching: • gas: 14 CF_4: 6 CHF_3, pressure: 10mT • power: 25 W • time: 1 min C etching: • gas: 14 Ar: 6 O_2, pressure: 10mT • power: 25 W • time: 6 min	Plasma-Therm 790 RIE
Pillar fabrication	Pillar etching by ion milling: • angle: 22.5 degree from surface normal • power: 500 V, 40 mA • time: end-point detection from SIMS Side wall trimming by ion milling: • angle: 85 degree from surface normal • power: 500 V, 40 mA • time: 28 s	Commonwealth Scientific Ion Mill #1

Table 3.3 Parameters used in step (c)

Process	Parameters	Tool
Photolithography for the bottom electrode with width > 2 μm	Resist: AZ 4210 Spin coating of HMDS adhesion layer and AZ 4210: • static dispensing: 600 rpm, 6s • spreading: 4000 rpm, 45 s Baking: 95 ^{0}C, 4 min Exposure: • power: 5 mW • time: 70 s Develop: • developer: AZ 400K • time: 1.8 min	Karl Süss MA6/BA6 Contact Aligner
E-beam lithography for the bottom electrode with width < 2 μm	Resist: maN 2405 Spin coating of HMDS adhesion layer and AZ 4210: • static dispensing: 600 rpm, 6s • spreading: 4000 rpm, 30 s Baking: 95 ^{0}C 1.5 min Exposure: • beam condition: 100 kV, 1nA • dose: 1000 μC/cm^2 Develop: • developer: MF CD-26 • time: 1.2 min	Elionix ELS-G100 Electron Beam Lithography System
Ion milling defining bottom electrode	• angle: 45 degree from surface normal • power: 500 V, 40 mA • time: end-point detection from SIMS	Commonwealth Scientific Ion Mill #1
Resist stripping	• Sonication in NMP for 20 min and then in Acetone for 20 min	

Table 3.4 Parameters for top window opening

Process	Parameters	Tool
SiN etching	• gas: 14 CF_4: 6 CHF_3, pressure: 10mT • power: 25 W • time: 1 min • etch rate: 0.267 nm/s	Plasma-Therm 790 RIE
C etching	• gas: O_2, pressure: 10mT • power: 25 W • time: 6 min	Plasma-Therm 790 RIE

Table 3.5 Parameters for bottom window opening

Process	Parameters	Tool
Photolithography for bottom window opening	Resist: AZ 4110 Spin coating of HMDS adhesion layer and AZ 4110: • static dispensing: 600 rpm, 6s • spreading: 4000 rpm, 45 s Baking: 95 ^{0}C, 4 min Exposure: • power: 5 mW • time: 55 s Develop: • developer: AZ 400K • time: 1.2min	Karl Süss MA6/BA6 Contact Aligner
SiN etching	• gas: 14 CF_4: 6 CHF_3, pressure: 10mT • power: 25 W • time: 1 min • etch rate: 0.267 nm/s	Plasma-Therm 790 RIE
Resist stripping	• Sonication in Acetone for 20 min	

Table 3.6 Parameters for Au deposition and lift-off in top electrode fabrication

Process	Parameters	Tool
Ti/Au deposition	Sputter etch: • gas: Ar, 5 mT • power: RF 200 W • time: 2 min Ti/Au deposition: • gas: Ar, 2.5 mT • power: DC 50 W for Ti, DC 25 W for Au • time: 42s for Ti, 300 s for Au	Nanofab sputtering system #1
Lift off	Soak in Acetone overnight and then sonication for 30 min	

3.1.3 Domain wall device and Hall-bar device fabrication

Although the domain wall device and Hall-bar device have different shapes, both are composed of channels that have a length of tens of μms and a width of 1-5 μm. After deposition of the magnetic stack, they share the same two-step patterning procedure:

(a) define the device structure by lithography and ion milling,
(b) make the Au contact with the device using lithography and lift-off.

Figure 3.5 illustrates the process for patterning the Hall-bar device. First, AZ 4110 resist is spin-coated onto the surface of the chip. Then the chip is exposed by photolithography, and then developed by AZ 400K developer to form a mask for etching of the device structure. If the width of the channel is less than 2 μm, e-beam lithography with maN 2405 resist and MF CD-26 developer will be used. Next, the chip is processed with ion milling to etching away all materials except for the ones under the resist, thereby the device pattern with the magnetic stack is formed. After stripping the resist, the chip goes through a second photolithography process with AZ 4210 resist to define the contact pattern. Finally, Au is deposited on the chip followed by a lift-off process. Figure 3.6 shows some sample images of the Hall-bar device and the domain wall device.

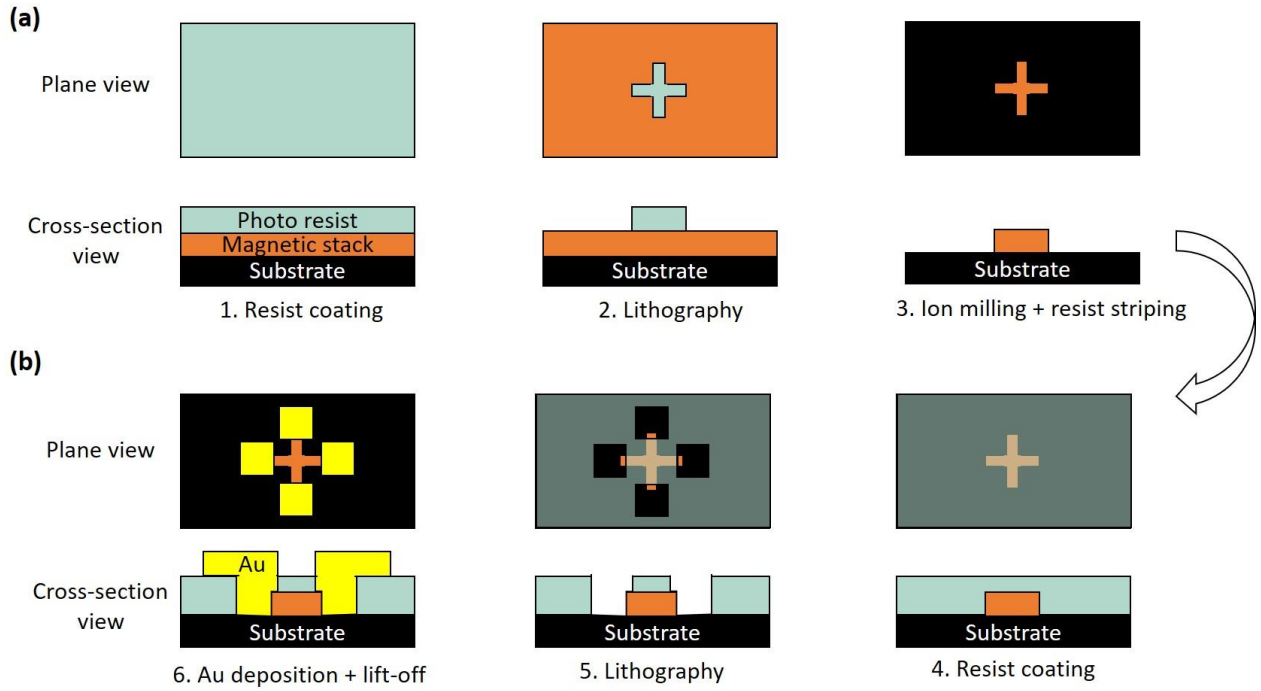

Figure 3.5 Process flow of the Hall-bar device fabrication.

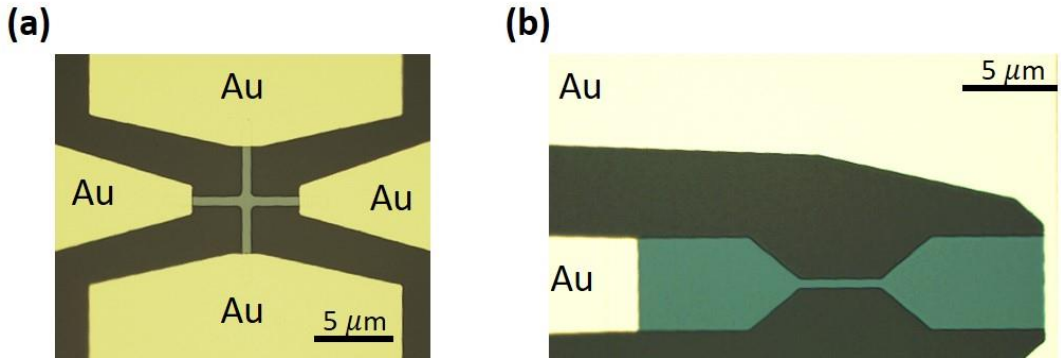

Figure 3.6 Optical images of (a) a Hall-bar device consisting of 2-μm-wide current- and voltage-channels and (b) a domain wall device with a 2-μm-wide wire.

3.2 Characterization

3.2.1 Hysteresis loop measurement

We use the Alternating Gradient Force Magnetometer (AGFM) to measure the magnetic moment of a magnetic film. The main components of the AGFM are gradient coils, vibrating rod and piezoelectric sensor (or force sensor). During measurement, the sample is attached to the end of the vibrating rod between gradient coils. The coils then generate a static field with a small alternating field to create a field gradient. When a magnetic sample with moment m is subjected to a field gradient, the force on the sample is given by $F = \mu_0 m \frac{dH}{dx}$ where μ_0 is the permeability of the vacuum, $\frac{dH}{dx}$ is the spatial field gradient. The displacement of the sample due to this force is detected by the piezoelectric sensor. Because the amount of displacement depends on the force acting on the sample that's further proportional to magnetic moment, in this way the sample moment can be measured. The sensitivity of AGFM is at the magnitude of 10^{-8} emu, suitable for the magnetic property characterization of thin films.

3.2.2 Lattice structure characterization

We use X-ray diffraction (XRD) to characterize the lattice structure of the films. In the XRD measurement, a W filament is first heated to generate streams of electrons. The electrons are then accelerated by an electrical field towards a metal target, for instance, a Cu target. When the target is being hit by electrons, its inner shell electrons are excited to higher energy level and then relax

back to the origin state, during which X-rays with specific wavelengths are generated. For our study, X-rays are from Cu K_α radiation with wavelength of 1.54 A. When X-rays interact with the sample, there is constructive inference if incident and diffracted X-rays beams have phase difference of $2n\pi$. It occurs when relative geometry of incident X-rays and lattice planes satisfies the Bragg's law given by $2dsin\theta = n\lambda$, where d is the lattice spacing, θ is the incident angle and λ is the wavelength of X-rays. Such constructive interference gives rise to high-intensity diffracted X-rays, which appears as peaks in the Intersity-Two theta diagram. From this diagram, we can extract structural information including the lattice constant, lattice type and expitaxy.

3.2.3 Hall-bar device testing

The Hall-bar device testing is used to measure the vertical component of the perpendicular magnetization via anomalous Hall effect. Figure 3.7 schematically shows the testing set-up. In field switching measurement, the chip sits between two electromagnets with the applied field normal to the chip surface. As a field-sweeping sequence is initiated by the controlling software, a 100 μA DC current from Keithley 2400 sourcemeter is applied into the current channel while the anomalous Hall voltage across the transverse voltage channel is detected. The anomalous Hall voltage is collected as a function of the applied field, which exhibits the existence of PMA of the magnetic stack. In current switching measurement, the chip is rotated by 90 degree so that a constant in-plane field can be applied parallel to the chip surface. A sequence of DC writing current pulses in 100 μs duration at mA level are sent into the current channel. The anomalous Hall voltage is measured with 100 μA current after each write pulse. The switching loop is recorded to determine the SOT property of the spin Hall layer.

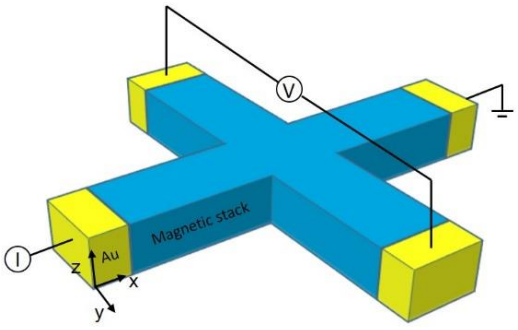

Figure 3.7 Illustration of the measurement set-up for the Hall-bar device testing.

3.2.4 Three-terminal SOT device testing

The three-terminal SOT device testing is done to determine the resistance state of the MTJ given the applied current in the write path. The testing set-up is illustrated in Figure 3.8. The AVTECH (model E1-B-W3) pulse generator or Keithley 2400 sourcemeter is used to send current pulses. The AVTECH pulse generator is capable of applying pulses with 1 ns – 5 μs duration at 1-20 V. If the pulse generator is used, a 50 Ω resistor needs to be connected in parallel with the write path to minimize the impendence mismatch. To avoid the high spike voltage across the MTJ during writing, a 10 MΩ resistor is connected in series with the MTJ. The MTJ resistance is monitored by SR830 lock-in amplifier. If an external in-plane field is needed, the chip is placed between two electromagnets which can generate magnetic field ranging from -10 kOe to 10 kOe.

During testing, DC current pulses are applied into the write path. The current value sweeps from positive to negative, then back to positive again. To monitor the MTJ resistance state, a 0.1 V AC reference signal at 2 kHz is applied across the MTJ and the 10 MΩ resistor, and then the voltage on the MTJ is read back by the lock-in amplifier. The current switching loop is recorded and used to analyze the characteristics of the SOT switching.

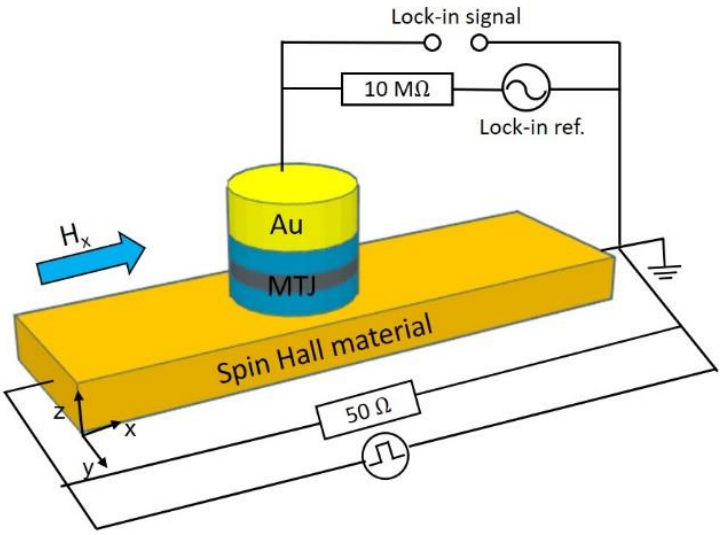

Figure 3.8 Illustration of the three-terminal SOT device testing

3.2.5 Domain wall motion measurement

A typical domain wall motion device consists of a center wire with two large pads on both sides. The end of the pads connects with Au electrodes for electrical probe contact. Prior to the testing, an artificial defect region is created on the pad area of the device by pulsing 300 ns beams at 5 kV and 1 nA in a focus ion beam system (FIB). The testing set-up is shown in Figure 3.9. The chip is placed on the sample stage below which there's a perpendicular electromagnet that can apply a magnetic field normal to the chip surface. The device is connected with an AVTECH (model E3-B-W1) pulse generator that can send 50-200 ns pulse at 1-100 V. A 50 Ω resistor is added in parallel to the device to match the output impendence of the pulse generator. The Kerr microscope with a 100X objective lens is used to perform the real-time difference imaging of the domain walls.

During the testing, a large out-of-plane field is applied to saturate the device, and then a small opposite field is applied to nucleate a domain surrounding the artificial defect. The field is turn off after the opposite domain expands into the wire. Another way to create opposite domains is by applying a large current pulse to the device. The significant joule heating can sometimes cause multiple random domain nucleation within the wire. Next, by sending moderate pulses into the wire, domain wall motion is induced and monitored by the Kerr microscope. The direction and speed of the domain wall motion are controlled by the polarity and magnitude of the applied voltage. Sequential images are taken and used to determine the velocity of domain wall motion.

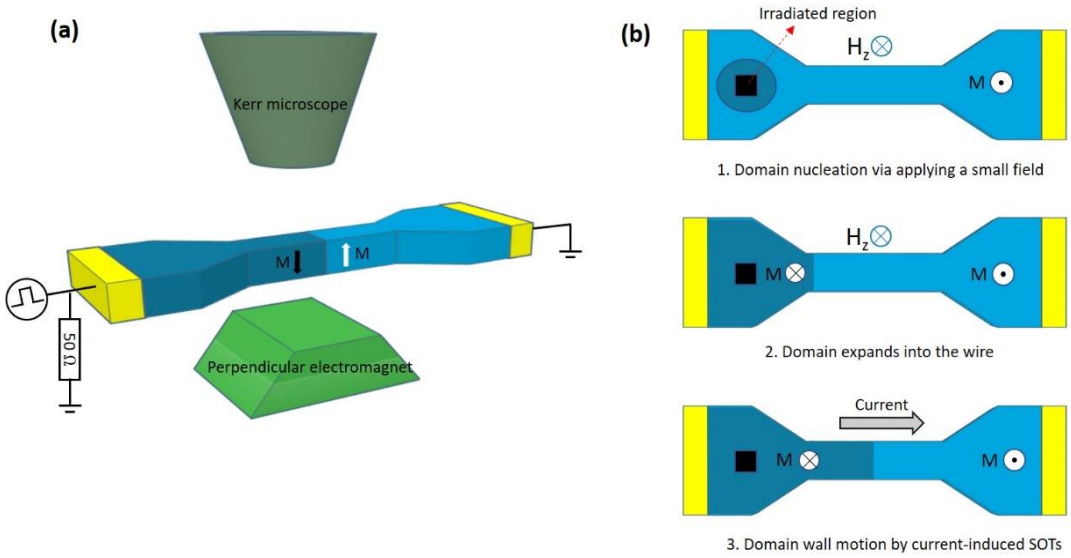

Figure 3.9 (a) Schematic of the domain wall motion testing. (b) Illustration of the testing procedure.

Chapter 4
Field-free Magnetization Switching with Iridium

Switching a perpendicular nanomagnet via spin Hall effect (SHE) induced spin orbit torques (SOTs) requires an in-plane field to break the symmetry[18,71]. Apply an *external* in-plane field, however, is not desirable for practical applications of SOT devices. Here we attempt to eliminate the need for an external field by engineering the SOT materials. In particular, we demonstrate that the field-free switching of a perpendicular magnet can be achieved by utilizing an iridium (Ir) layer. The Ir layer not only provides SOTs via SHE but also induce a local in-plane field through interlayer exchange coupling (IEC) with an in-plane magnetic layer, combined of which gives rise to the perpendicular SOT switching that doesn't require an external field. Experimental observations also show that the SOT driven field-free magnetization reversal in the micron-size devices takes place as domain nucleation and expansion. In addition, micromagnetic modeling is carried out to provide in-depth understanding of the SOT driven perpendicular magnetization reversal process in the presence of the in-plane exchange coupling field.

4.1 Material selection

The idea here in achieving the external-field-free SOT switching lies in replacing the external field with a "local" in-plane field that's naturally existed in the SOT device. One approach to have such local field is via utilizing the interlayer exchange coupling (IEC), i.e. RKKY interaction. Figure 4.1 shows the designed SOT device that makes use of the IEC to assist the SOT switching of a perpendicular magnet. Compared to the conventional SOT device, there is an additional in-plane layer placed underneath the heavy metal layer. The heavy metal layer is designed to be a RKKY material so that it exchange couples the magnetic layers below and above it. As a result, the top perpendicular layer experiences a local in-plane field deriving from the IEC

with the bottom in-plane layer. When SHE-induced SOTs are exerted on the top layer, the local in-plane field can facilitate the SOTs to flip the magnetic moment and thus lead to deterministic magnetization switching. For this device to work, it's necessary to select a heavy metal material that satisfies the following requirements:

(a) it's capable of providing adequate IEC to couple the adjacent ferromagnetic layers,

(b) it's able to generate large enough spin current for inducing SOT magnetization switching,

(c) in order to have the potential in integrating with perpendicular MTJs, it should promote, or at least not degrade, the perpendicular magnetic anisotropy (PMA) of the adjacent Fe/Co-based magnetic layers.

The survey of some common spin-Hall and RKKY materials is listed in Table 4.1. The widely used spin-Hall materials, such as Ta and W, have good spin Hall properties but don't supply enough IEC. The strong RKKY material Ru, on the other hand, doesn't show clear evidence of SHE. Eventually, we discover that Ir has well balanced properties in terms of both SHE and IEC. Additionally, Ir can form strong PMA with the ultra-thin Co and FeCoB/ MgO layers. These combined characteristics make Ir a desirable candidate in order to achieve the field-free SOT switching of a perpendicular magnet.

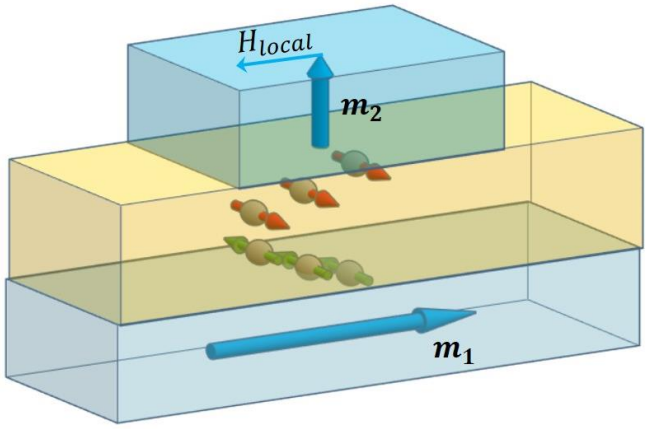

Figure 4.1 The designed device that utilizes IEC to assist the SOT switching of a perpendicular magnet. The heavy metal layer in the middle can provide IEC so that the top perpendicular layer $\boldsymbol{m_2}$ experiences an in-plane exchange coupling field H_{local} from the bottom in-plane layer $\boldsymbol{m_1}$. The antiferromagnetic coupling is shown in this drawing.

Table 4.1 Summary of the IEC, SHE and PMA of some spin-Hall and RKKY materials

Material	IEC	SHE	PMA with Co	PMA with FeCoB/ MgO
Ta	Very weak	Yes	No	Yes
W	Very weak	Yes	No	Yes
Pt	Weak	Yes	Yes	No
Ru	Yes	No	No	No
Cr	Yes	No	No	Weak
Ir	Yes	Yes	Yes	Yes

4.2 Interlayer exchange coupling and spin Hall effect of Ir

To study the IEC of Ir, we fabricate a series of films that consists of substrate/ Co (1.1 nm)/ Ir (t_{Ir})/ Co (1.1 nm)/ Ta (2 nm), where t_{Ir} ranges from 0.6 nm to 1.65 nm. All films show well-defined PMA originating from the Ir/Co interfaces. The measured perpendicular hysteresis loops are used to determine the strength of IEC via the Ir spacer. Figure 4.2 shows the exchange coupling field as a function of the Ir thickness. Note that only antiferromagnetic coupling is included in Figure 4.2. The first antiferromagnetic coupling peak of Ir locates at 0.6 nm, which gives quite strong coupling field of 9 kOe. The magnitude of exchange coupling field (strength) decays dramatically from the first peak to the second peak locating at 1.35 nm. The exchange coupling field via the 1.35 nm Ir is around 850 Oe.

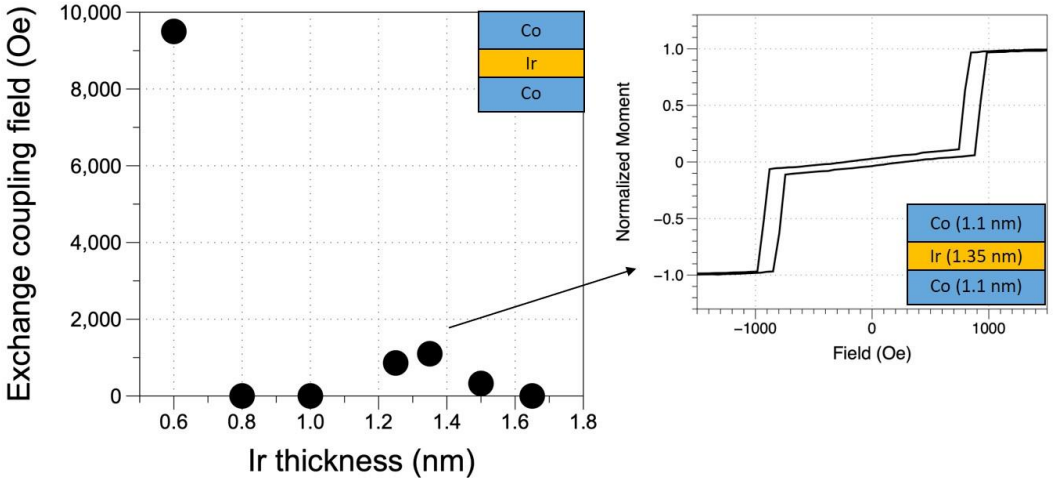

Figure 4.2 Antiferromagnetic coupling field as a function of the Ir spacer thickness. Top right: perpendicular M-H loop of Co (1.1 nm)/ Ir (1.35 nm)/ Co (1.1 nm).

To explore whether Ir can generate sufficient spin current for inducing magnetization switching, we perform the SHE-induced switching experiments. The film stack for this study is substrate/ Ta(0.5 nm)/ Ir(3 nm)/ Co(1.2 nm)/ Ta(2 nm). The film is patterned into Hall-bar devices with 4-μm wide current channel and 1-μm wide voltage channel utilizing e-beam lithography, optical lithography and ion beam etching. Figure 4.3(b) shows the perpendicular-field-driven anomalous Hall effect (AHE) loop, confirming that the PMA of the Co layer preserves after device fabrication. In current-induced switching measurement, current pulses are injected along the current channel with each pulse length of 100 μs. The amplitude of the current at milliamp (mA) level sweeps from negative to positive values and back to negative again. The anomalous Hall voltage is measured after each write pulse with a read current of 100 μA. An external in-plane field H_x is applied ranging from 100 Oe to -100 Oe. Figure 4.3(c) shows the measured anomalous Hall voltage as a function of current density in the Ir layer with or without an externally applied in-plane field H_x. Bipolar magnetization switching occurs in the presence of H_x while no sign of switching is observed without H_x. This agrees with the 'symmetry' argument for the SOT perpendicular magnetization switching, as discussed in Chapter 2, that an in-plane field is required to assist the switching. Furthermore, the switching loop has flipped shape as the direction of H_x reverses. The direction of H_x determining the switching behavior is also a typical evidence of SHE-induced switching of a perpendicular magnet. Hence, our results have proven that Ir has strong enough SHE to generate sufficient SOTs for switching a perpendicular Co layer. Note that the actual spin Hall angle of Ir is still under debate for that different research groups reported different values depending on their fabrication and measurement techniques[72–75]. From our other experiments, the current density needed for switching a perpendicular Co layer by Ir is found to be about 30-35% higher than that by Pt, which gives a rough estimate of Ir's spin Hall angle to be 2/3 of Pt. With that being mentioned, however, our main interest in the study of Figure 4.3 lies in whether Ir can produce enough spin current for inducing SOT switching rather than investigating the fundamental physical property of Ir.

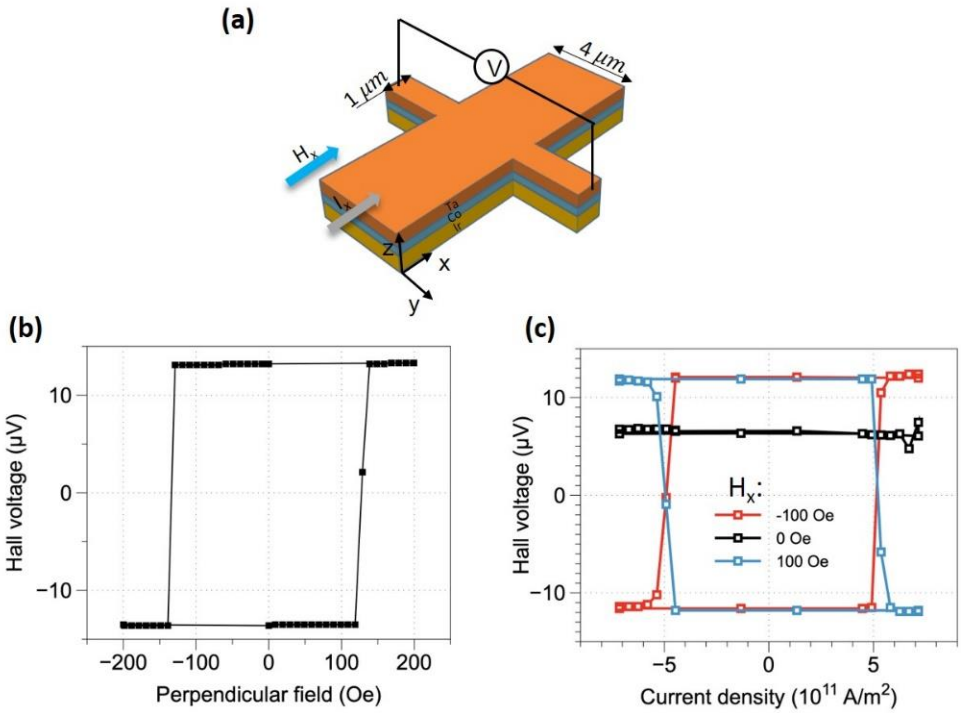

Figure 4.3 (a) Schematic of the Hall-bar device. (b) Anomalous Hall voltage as a function of the perpendicular field. (c) Anomalous Hall voltage as a function of the current density applied in the current channel of the device w/o an external in-plane field.

4.3 Field-free magnetization switching of a perpendicular Co layer

Now that we've obtained clear signs of IEC as well as SHE of Ir, we'd like to harness these properties to realize the field-free SOT switching of a perpendicular magnet. The key is to be able to provide a local in-plane exchange field for the perpendicular layer from its coupled in-plane layer via Ir. For this purpose, the film stack for field-free magnetization switching is designed to be substrate/ Co(2)/ Ru(0.85)/ Co(2)/ Ir(1.35)/ Co(1.2)/ Ta(2), with unit in nanometers. The top thin Co layer is naturally perpendicularly magnetized due to the interfacial PMA arising from the interface with the Ir layer. The thickness of the Ir layer is chosen corresponding to the second antiferromagnetic coupling peak in Figure 4.2. The reasons for not using the thickness of the first coupling peak are that (1) the exchange coupling at the first peak (via 0.6 nm Ir) is too strong so that the coupled perpendicular Co layer will be pulled to in-plane direction (2) 0.6 nm thickness can be harder to control experimentally and thereby inconsistent from time to time. The Co/Ru/Co below the Ir layer is a flux-matched in-plane synthetic antiferromagnetic (SAF) structure where the upper Co layer is designated to serve as the source of the local exchange coupling field. The

reasons for using the SAF instead of a single in-plane Co layer is that the zero net moment of the SAF minimizes the effect of the in-plane stray field from the in-plane Co layers and thus if there is any sign of a local in-plane field, we will know that it can only derive from the IEC. Figure 4.4(b) shows the in-plane hysteresis loop of the SAF. Unlike the double switching in antiferromagnetically coupled perpendicular layers (for example, as shown in Figure 4.2 top right), the hysteresis loop of the in-plane SAF only shows gradual change in the magnetic moment. This is because the exchange coupling via 0.85 Ru is quite strong, and so the in-plane Co layers behave like single domain within the isotropic film plane. In such case, when the moment of one Co layer rotates within the film plane, the moment of the other Co layer is forced to rotate simultaneously by the strong exchange coupling field. At zero field, the two Co layers are anti-aligned along the direction normal to the applied magnetic field. Hence, what we observe is the gradual change in the magnet moment.

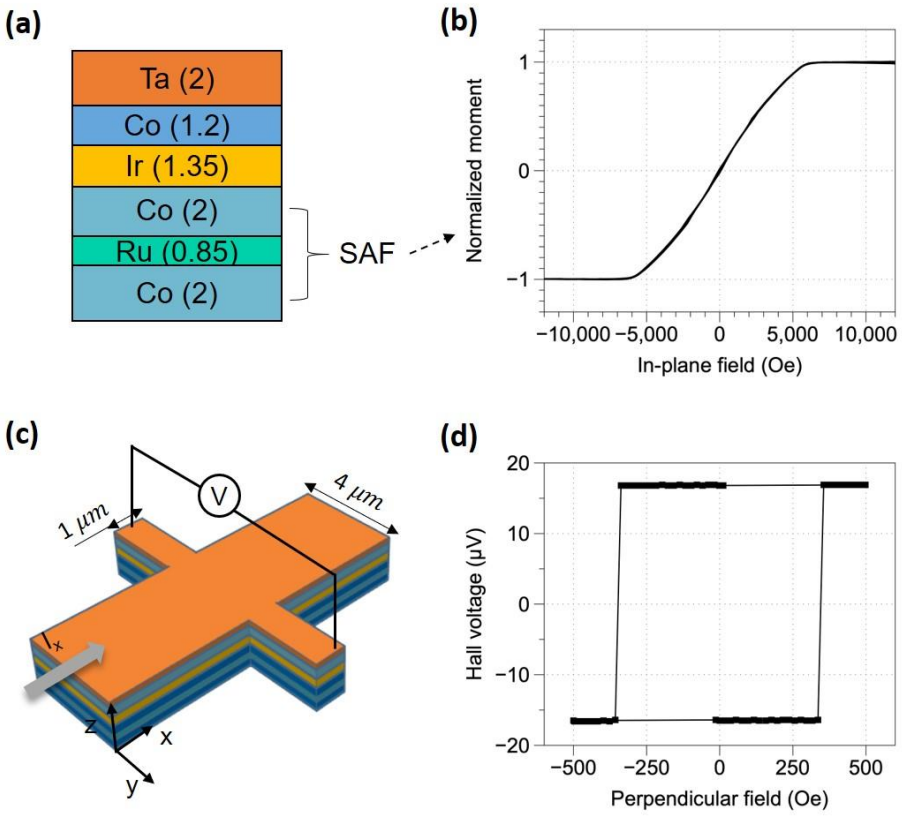

Figure 4.4 (a) Film stack for field-free magnetization switching, with unit in nanometers. (b) In-plane hysteresis loop of a pure SAF structure with the film stack of substrate/ Ta/ Co(2 nm)/ Ru(0.85 nm)/ Co(2 nm)/ Ta. (c) Schematic illustration of the Hall-bar device for spin-orbit torque measurement. (d) Perpendicular-field-driven anomalous Hall effect loop for the device with the film stack shown in (a).

The film is then lithographically patterned into cross-shape Hall-bar devices with 1-μm voltage channel and 4-μm current channel. Figure 4.4(d) shows the measured Hall voltage arising from anomalous Hall effect (AHE) with varying external perpendicular fields. The squared shape of the AHE loop indicates clear perpendicular magnetic anisotropy of the top Co layer at device level.

Next, we perform current-induced magnetization switching measurements. Figure 4.5(a) shows the anomalous Hall voltage as a function of current density with a series of external in-plane fields H_x, applied along the current direction. For H_x > 200 Oe, well defined switching loops are obtained with positive and negative saturation values corresponding to the two perpendicular magnetization states. At H_x = 200 Oe, the switching hysteresis loop collapses, indicating no magnetization switching occurs. At zero external field, the switching completely recovers, however, with flipped loop shape. The same switching loops are maintained for H_x < 0. Figure 4.5(b) shows the similar measurement sequence with the reversed magnetization of the bottom SAF structure (from $\rightleftarrows$ to $\leftrightarrows$). In contrast to that shown in Figure 4.5(a), the collapse of the switching hysteresis loop now occurs at H_x = -200 Oe instead.

It is our interpretation that when charge current flows into the Ir layer, pure spin current is generated due to SHE and then injected to the top perpendicular Co layer. This pure spin current drives the observed magnetization reversals provided there exists an in-plane magnetic field. At zero applied field, this in-plane field arises from the IEC between the perpendicular Co and in-plane Co layers above and below the Ir interlayer via the RKKY interaction. When the externally applied field cancels the coupling field in magnitude and direction exactly, magnetization reversal no longer occurs. Our evidence suggests this in-plane coupling field has a magnitude of 200 Oe. It should be noted that the 200 Oe coupling field shown in the devices is significantly smaller than that measured at film level, which is around 850 Oe.

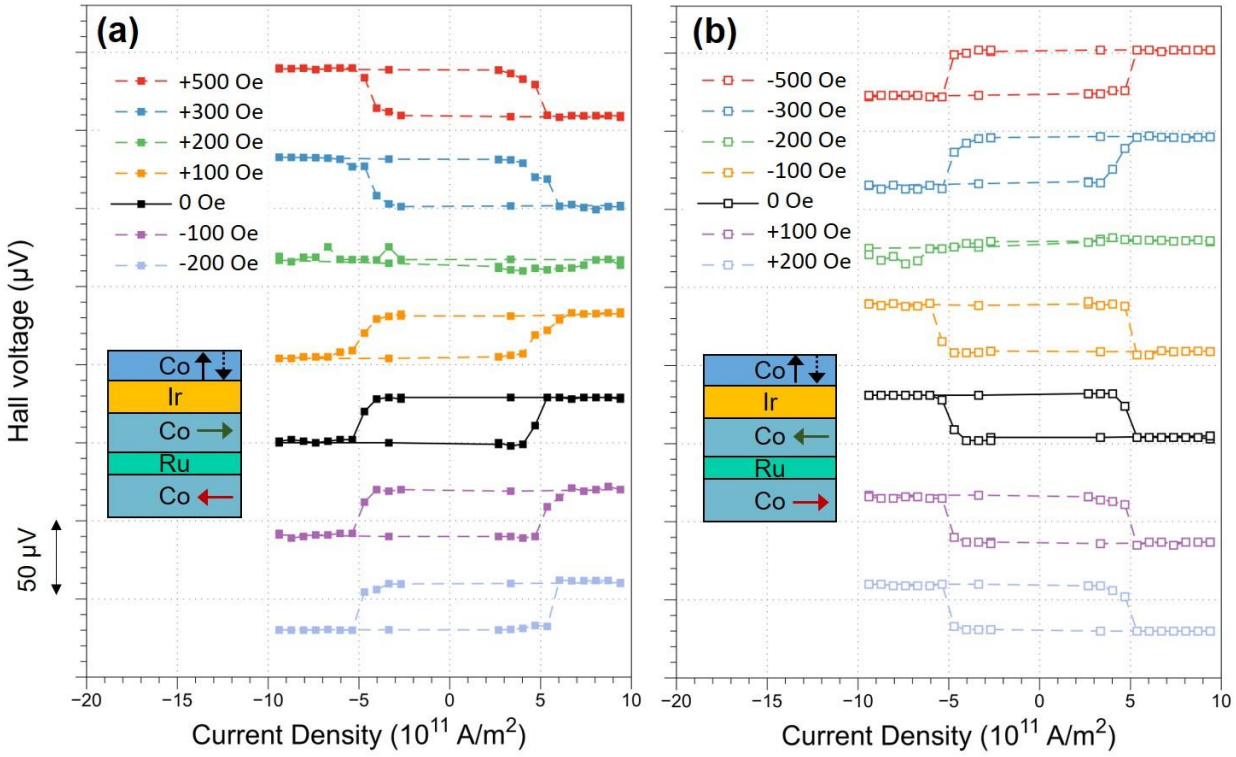

Figure 4.5 Anomalous Hall voltage as a function of injected current density with different external magnetic fields H_x along the current direction. Bottom SAF is set as (a) ⇄, and (b) ⇆.

4.4 Switching process

To understand the nature of the current-induced magnetization switching in the presence of the in-plane coupling field in our devices, Kerr microscopy is utilized to visualize magnetization reversal process. In this measurement, a sequence of 100-ns current pulses is applied into the current channel of the device, and Kerr images are taken after each pulse. As shown in Figure 4.6(a), it's observed that small opposite domains nucleate at the beginning of the reversal. The nucleation sites mostly locate around the device edge which is likely due to the degradation of perpendicular anisotropy possibly caused by the etching process during device fabrication. Continued application of subsequent current pulses results in the expansion of the reversed domains in all directions. With sufficient number of current pulses, the region along the current pulses can be mostly reversed. We should note that there are always some small residual domains located sparsely along the current path that are difficult to eliminate, even with perpendicular magnetic field.

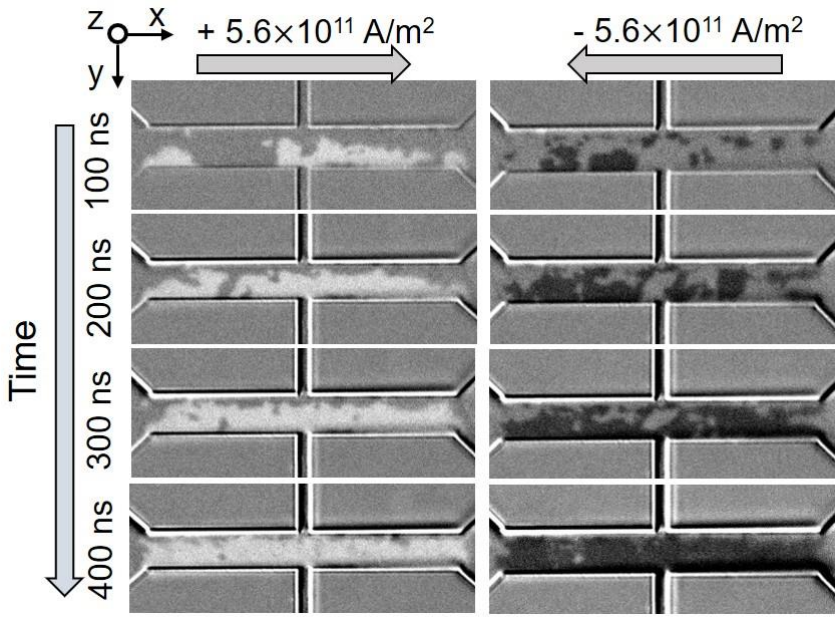

Figure 4.6 Kerr microscope images showing the domain wall propagation during the current-induced magnetization switching process, without external magnetic field. Current is applied in –x (left) and +x (right) directions. Bottom SAF is set as ⇄ . Between image in each column: 100-ns pulse, 1 pulse.

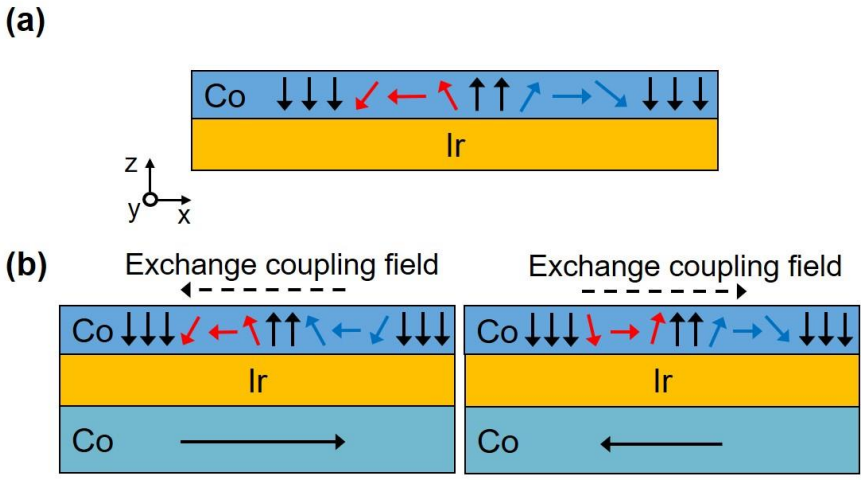

Figure 4.7 (a) Schematic illustration of right-handed domain wall structures in Ir/Co system. Red arrows: down-up domain wall. Blue arrows: up-down domain wall. (b) Domain wall structures in presence of the exchange coupling field.

It has been observed that SHE can induce domain wall motion (DWM) in heavy metal/ ferromagnet systems[35,59,76,77]. One of the keys to enable the SHE-induced DWM is the Dzyaloshinskii-Moriya interaction (DMI) at heavy metal/ ferromagnet interface that not only makes Neel-type domain walls (DWs) more energetically favorable than Bloch-type ones but also introduces chirality to the domain wall structure. Normally, up-down and down-up DWs of an

opposite domain possess the same chirality (either left- or right-handed), as shown in Figure 4.7(a). These DWs move in the same direction when receiving the SOTs from the neighboring heavy metal layer and thus domains can only shift forwards or backwards. With applying external in-plane field that's larger than the effective DMI field, up-down and down-up DWs can turn into different chiral structures. They travel in the opposite directions when interacting with SOTs. As a result, a domain can either expand or shrink depending on the direction of injected current, which further leads to deterministic magnetization switching.

In our case, we measured the effective DMI field as well as DW chirality at Ir/Co interface by measuring the growth of magnetic bubble domains. The mechanism of this measurement is schematically demonstrated in Figure 4.8(a). During the measurement, a magnetic bubble domain (Figure 4.8(a), solid circle) is first initiated. Then perpendicular-field pulses are applied to grow the bubble domain, with or without the presence of an in-plane field. If no in-plane field is applied, the bubble domain should grow symmetrically regardless of the DW structure. When perpendicular-field pulses are exerted with an in-plane field present, the bubble domain will grow faster at one side where its center DW magnetization lies parallel to the in-plane field. A naïve way to understand it is that the in-plane field assists the precession of DW magnetizations in their travelling direction. As for the DW with magnetization anti-aligned to the in-plane field, the growing speed is suppressed. Accordingly, the bubble domain exhibits asymmetrical growth (Figure 4.8(a), dashed circles on the left and right). Note that this can only occur in the case of Neel-type DWs stabilized by DMI. The chirality of Neel-type DW as well as the effective DMI field can be determined by DW velocity curve as a function of the in-plane field. The results for our film with Ir(3 nm)/ Co(1.2 nm) are shown in Figure 4.8(b). As a small positive in-plane field H_x is applied, we observe up-down DW moves faster while down-up DW moves slower. Since higher DW velocity is the result of parallel configuration of H_x and DW magnetization, we infer that DW chirality at Ir/Co interface is right-handed. In addition, the velocity of down-up DW reaches a minimum at $H_x = +90$ Oe . Similarly, another minimum is observed for up-down DW at H_x = -90 Oe. These minima occur when H_x exactly cancel with the effective DMI field that stabilizes Neel-type DWs, which implies the effective DMI field has the magnitude of 90 Oe. As H_x further increases, it's able to flip the anti-aligned DW magnetization and thus DW velocity starts to increase.

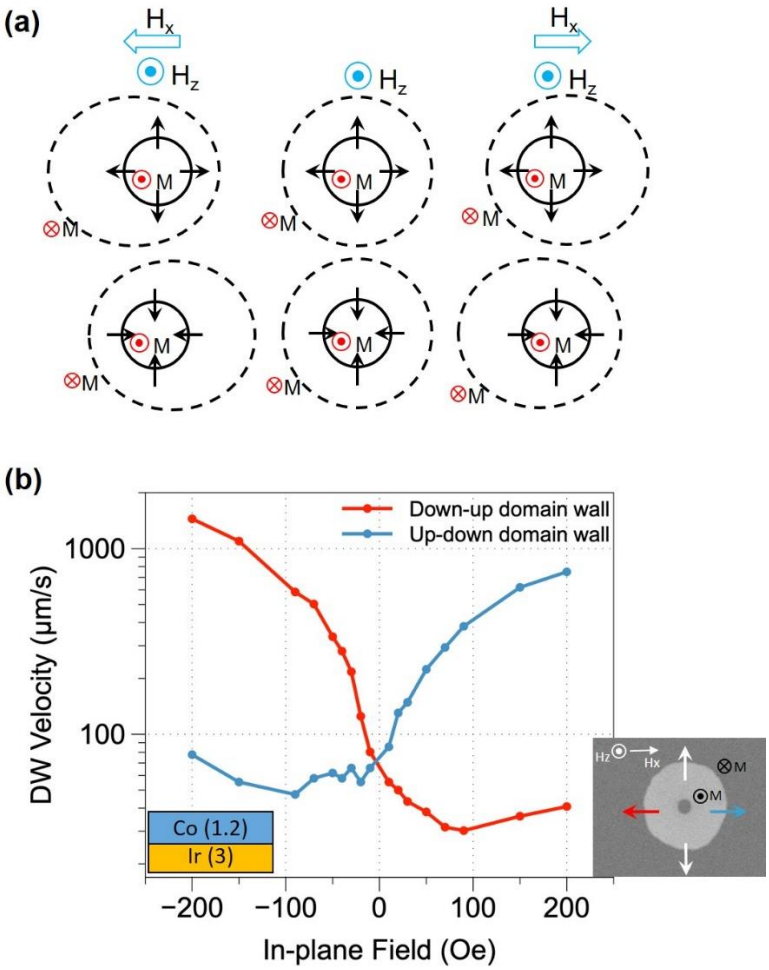

Figure 4.8 Schematic of magnetic bubble domain measurement. Solid circle: initial bubble domain. Dashed circle: bubble domain after growth. Black arrow: magnetization at center of DW. (b) Velocity of down-up and up-down domain wall as a function of in-plane magnetic field. The perpendicular field used for growing the bubble domain has the magnitude of H_z = 50 Oe.

With the effective DMI field being characterized as 90 Oe, the exchange coupling field (200 Oe) in our devices is able to overcome the effective DMI field and give rise to the domain walls with opposite chirality (Figure 4.7(b)). Hence, based on our observations, it's the two types of domain walls moving in opposite directions that enables field-free magnetization switching. Therefore, the magnetization switching process in our devices can be interpreted as domain nucleation followed with thermally assisted SHE-driven DWM till the expansion of reversed domains produces full reversal.

Recently, CB Seung-heon, *et al*.[43] reported that spin current generated by the interface of non-magnetic metal/ in-plane magnetized ferromagnet can contain some perpendicular

polarization. Such perpendicular component of the spin current further gives rise to the SOTs that can achieve field-free magnetization switching. This mechanism can't be applied to explain our observations since the spin diffusion length of Ir is only 0.5 nm[78]. Therefore, even if such spin current is generated at Ir/ in-plane Co interface it can't travel through the 1.35 nm-thick Ir layer to reach the top perpendicular Co layer.

4.5 Simulation

To provide further understanding of the magnetization reversal process, the effect of pure spin current on the perpendicular Co layer is modeled by Slonczewski spin transfer torque included Landau-Lifshitz-Gilbert damped gyromagnetic equation of motion. The full stack is modeled with the bottom SAF structure set as ⇄. The IEC strength between the perpendicular Co layer and the inplane Co layer sandwiching the Ir layer is varied throughout the study. The top perpendicular Co layer is assumed to have 2 nm thickness with interfacial perpendicular uniaxial anisotropy of K_s = 4 x 10^{-3} J/m^2 and saturation magnetization M_s = 1.2 T. The two Co layers in the Co/Ru/Co SAF are assumed to be flux-matched without perpendicular anisotropy and to have antiparallel exchange coupling of $\sigma_{ex,SAF}$= -1.0x10^{-3} J/m^2. The film stack is meshed laterally with each mesh cell of 2 x 2 nm^2 size. The exchange stiffness constant A = 1.6 x 10^{-11} J/m is assumed for all three Co layers. A spatially uniform pure spin current with spin polarization along the positive y-direction is assumed corresponding to a charge current density of J_c= 10^{12} A/m^2 and a spin Hall angle of 0.1. The top Co layer of the SAF is always magnetized along the positive x-direction with essentially uniform magnetization. Zero DMI is assumed for simplification.

The modeling is carried out by initially creating a reversed domain, or domains, in a perpendicularly saturated top Co layer. Figure 4.9 shows sets of time evolution of domain configurations during the expansion of the initial reverse domains under the pure spin current. It is found that the reversed domains expand in all directions. Domain walls that are parallel to the IEC field (as in the top left) move as fast as those orthogonal to the field (top right). It is interesting to note that as the reverse domains expand, the wall fronts often become curved during their motion (except when the wall front is perpendicular to the exchange field, as the case of top right in the Figure 4.9 shows.). This is because the wall moving speed is correlated with the orientation of magnetization component at the center of the wall. Figure 4.10 shows the wall speed as a function

of the along-wall projection of the magnetization at the center of the wall with varying IEC strength. The simulation results suggest that the wall moves faster when the magnetization at the center of the wall becomes more parallel to the tangent of the wall. Furthermore, it can also be seen that not only the speed of DWM but also the slope of the speed angular dependence increases with higher IEC field.

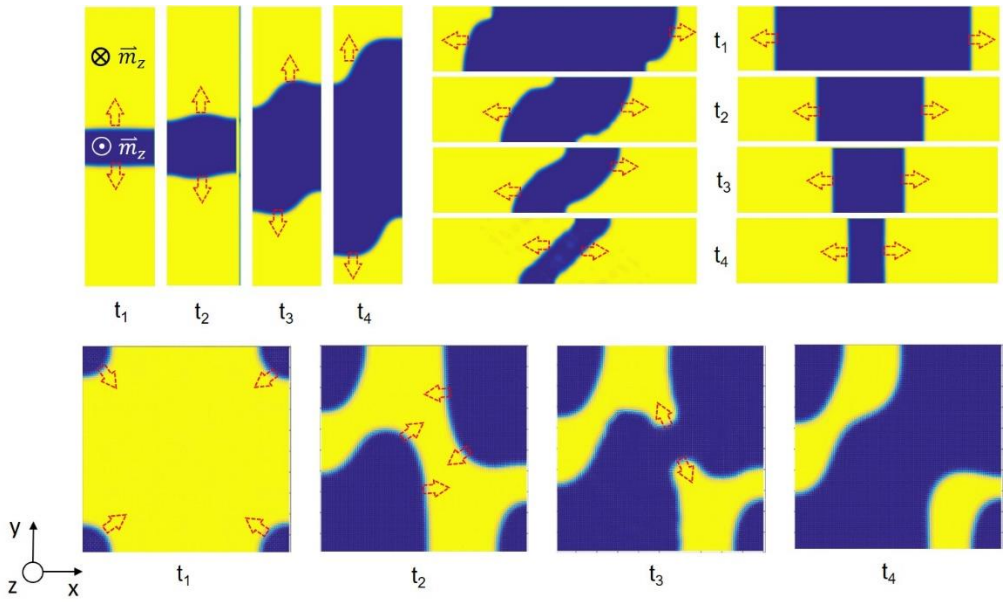

Figure 4.9 Simulated domain expansion in the perpendicular Co layer in the presence of the in-plane coupling field. The charge current flows along the x-axis. $t_1 < t_2 < t_3 < t_4$ represents the time evolution during the application of current.

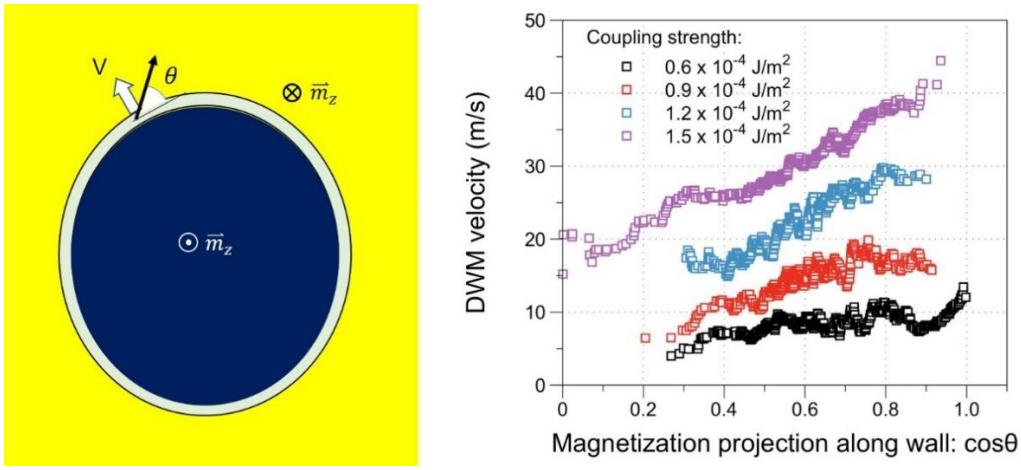

Figure 4.10 Calculated domain wall moving speed under the SHE generated spin current as a function of the direction cosine of the wall center magnetization along the wall tangent with four different in-plane coupling field strengths.

4.6 SOT Switching with Ir at other thickness

The SOT switching with Ir at other thickness is also investigated. All fabrication and measurement parameters are kept the same as previously used except that the Ir thickness is changed to 3 nm. Now the device contains the film stack of substrate/ Co(2)/ Ru(0.85)/ Co(2)/ Ir(3)/ Co(1.2)/ Ta(2), with unit in nanometers. With the 3 nm Ir layer, the strength of the IEC should decay to nearly zero. Current switching results in Figure 4.11 show that the magnetization reversal takes place in the presence of an external in-plane field while negligible moment change is observed at zero field. The switching results clearly differs from the ones with the 1.35 nm Ir, which further verifies that the IEC plays an important role in realizing the field-free SOT magnetization switching.

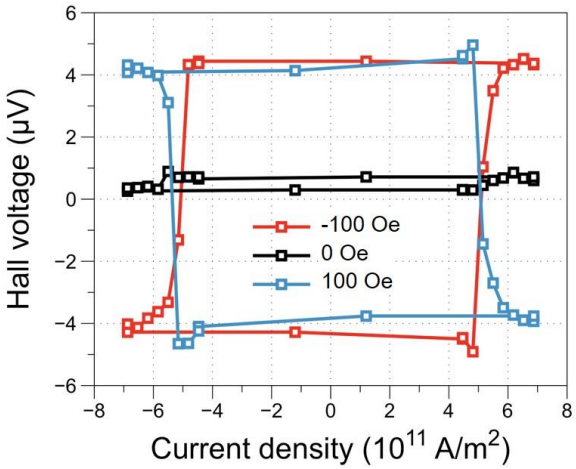

Figure 4.11 Current switching results with a 3-nm Ir.

4.7 Replacing Ir with other spin Hall materials

Instead of IEC, it was suggested that the magnetic stray field from the in-plane layer underneath the spin Hall layer might be able to assist the perpendicular SOT switching[79,80]. Here, we examine this concept by using two heavy metal materials, Pt or W, that are known to have prominent SHE but weak IEC.

For the study with W, the film stack consist of substrate/ Ta(0.5 nm)/ Co(2 nm)/ W(2 nm)/ FeCoB(1.2 nm)/ MgO(2 nm)/ Ta(2 nm). In order to promote the PMA of the FeCoB layer, the film is post-annealed at 300 ^{0}C for 10 min with a 5 kOe field applied normal to the film surface. Figure

4.12 shows the current switching results under different external in-plane fields measured in the Hall-bar device. As we can see, the in-plane Co layer is first saturated at H_x = + 1000 Oe, and under this field full SOT switching of the perpendicular FeCoB layer is observed. As H_x decreases to +100 Oe, the switching becomes incomplete, which is indicated by the reduced range of the anomalous Hall voltage. The switching loop further shrinks with smaller H_x and eventually flattens at H_x = +25 Oe. At zero field, partial switching occurs with the change in anomalous Hall voltage only 27% of that at H_x = + 1000 Oe. We notice that the shape of the switching loop changes from anti-clockwise at $H_x \geq 50$ Oe to clockwise at zero field, indicating the net field acting on the perpendicular Co layer changes its sign. This can be the evidence of the magnetic stray field pointing in $-x$ direction because the stray field acting on the top perpendicular layer should be antiparallel to the magnetization of its source that's the bottom in-plane Co layer. The switching loop recovers when a negative field is applied. The switching range at H_x = -100 Oe is slightly larger than that at H_x = +100 Oe, which further confirms the existence of the in-plane stray field.

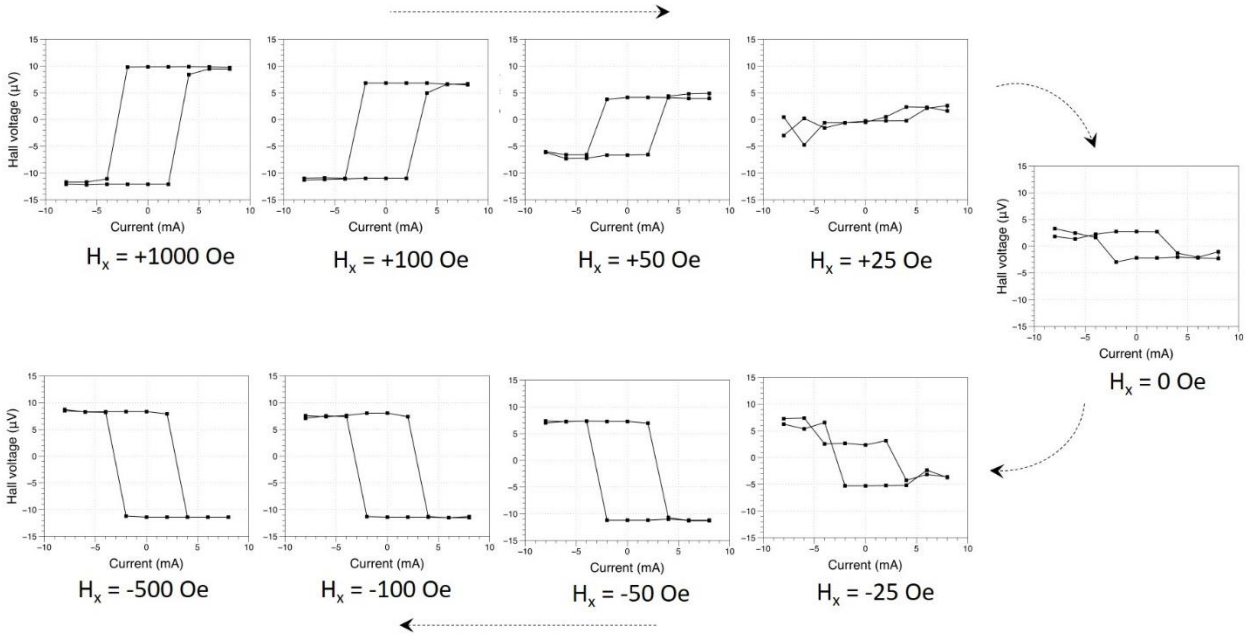

Figure 4.12 Current switching results in W-based device. The switching loops are measured under various external in-plane fields starting from +1000 Oe to -500 Oe

More experiments are conducted with Pt to be the spin Hall material. Here the film stack is Ta(0.5 nm)/ Co(2 nm)/ Pt(2 nm)/ [Co(0.3 nm)/Ni(0.6 nm)] x2.5/ Ta(2 nm). The perpendicular component is the Co/Ni multilayer stack. Figure 4.13 shows the current switching in the patterned

Hall-bar device. In this case, very small proportion of the perpendicular moment can be switched without an external field. Interestingly, it's found that the switching polarity at zero field is the same as that at a large external field, suggesting there's a ferromagnetic coupling across the 2 nm Pt, although the coupling is quite weak. In this case, the coupling field and the stray field are in opposite directions, countering each other's effect, and thus the switching range at zero field appears to be quite small.

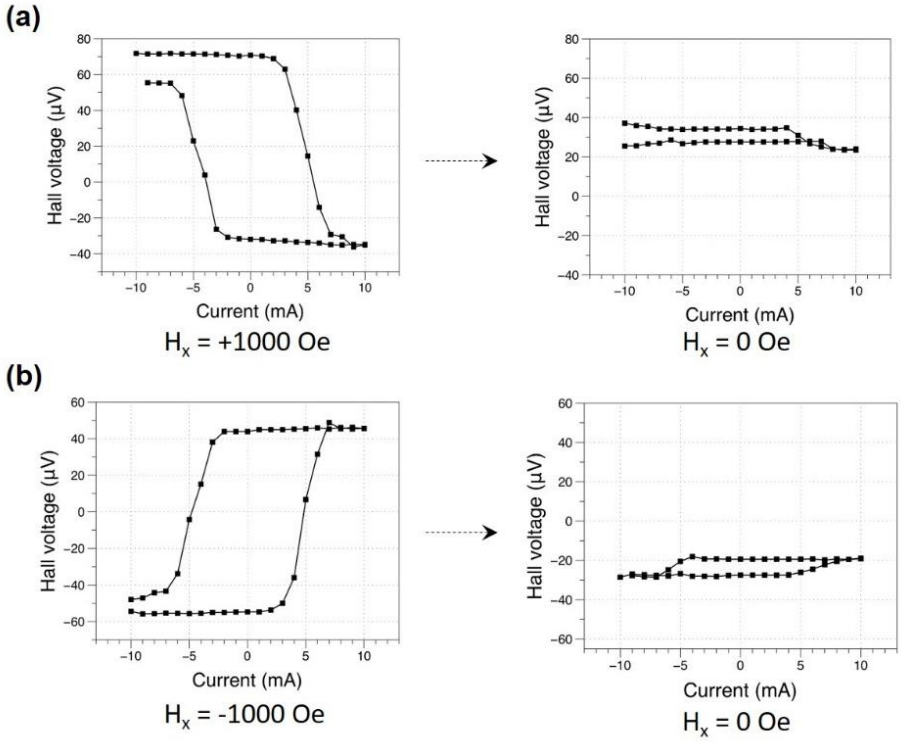

Figure 4.13 Current switching results with Pt. (a) The device is first saturated and the switching loop is recorded at H_x = +1000 Oe. Then the field is turned off and switching loop is measured again. (b) H_x is first set as -1000 Oe and then to 0 Oe.

We can also estimate the stray field from the 2 nm in-plane Co layer mathematically. In Figure 4.14, the in-plane Co layer is simplified as a single domain. Point A and B are at the two ends of the in-plane Co layer while point C is at the center of the perpendicular layer. We would like to calculate the stray field H_C at point C due to the magnetic flux coming out from point A and B. Now the field from point A is given by $H_A = \frac{\mu_0 m_A}{4\pi r^2} = \frac{\mu_0 m_A}{4\pi(d^2+l^2)}$ where m_A is the magnetic strength at point A. Similarly, the field from point B is $H_B = \frac{\mu_0 m_B}{4\pi(d^2+l^2)}$. From the geometry shown

in Figure 4.14, we have $H_C = H_A cos\theta + H_B cos\theta$. Because $m_A = m_B$ and $cos\theta = \frac{l}{\sqrt{d^2+l^2}}$, by rearranging the equation we can get

$$H_c = 2H_A cos\theta = \frac{\mu_0 m_A 2l}{4\pi(d^2+l^2)^{3/2}} = \frac{\mu_0 M}{4\pi(d^2+l^2)^{3/2}} \approx \frac{\mu_0 M}{4\pi l^3} \qquad \text{Equation 4.1}$$

where M is the moment of the in-plane Co layer. On the other hand, the moment of the in-plane Co layer can be calculated by $M = M_s V$ where M_s is the saturation magnetization of Co and V is the layer volume. By plugging the experimental parameters, we get H_c = 0.46 Oe, which is almost negligible. Clearly, such small field can't cause the complete SOT switching of the perpendicular Co layer. With this being mentioned, however, it should be noted that the stray field can be prominent at the two ends of the perpendicular layer due to much smaller l value in Equation 4.1. So there can be some domain expansions at the two ends of the perpendicular layer.

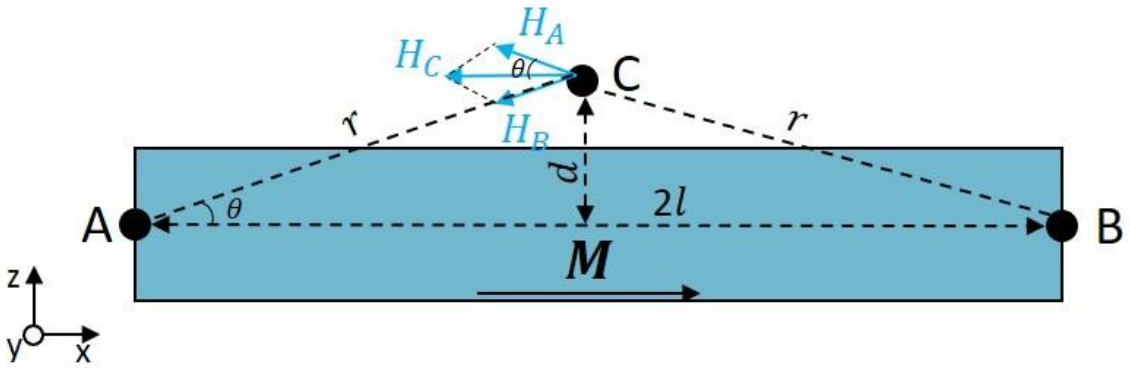

Figure 4.14 Calculation of the stray field. The blue rectangle is the in-plane Co layer that's viewed as a single domain. Point A and B are at the two ends of the in-plane layer. Point C denote the center position of the perpendicular layer. Here, $2l$ = 12 μm and d = 2 nm.

Both our experimental and calculation results show that the stray field from an in-plane layer is not adequate for inducing complete perpendicular SOT switching. Therefore, using the stray field is not an ideal approach to realize the field-field perpendicular SOT switching.

4.8 Summary

In this chapter, we demonstrated that Ir is capable of acting as both a spin-current source via SHE as well as a local field mediator by IEC. With these properties combined, we were able to obtain the robust field-free SOT switching of a perpendicular magnet in absence of an external

field. The switching process in the fabricated micron-size devices was found to be dominated by SHE-induced DWs propagation to achieve the full expansion of reserved domains. The role of the in-plane exchange coupling field in the DWM is that it overcomes the effective DMI field and alter the chiral structures of the DWs. Modeling study shows that in the presence of the in-plane coupling field, the nucleated domains can expand in all directions and the higher the coupling field, the higher the expansion speed of the reversed domains. The domain wall speed also increases when the magnetization at the center of the wall becomes more parallel to the wall during the motion. It's noteworthy that the film stack we used is easy to be built up with magnetoresistive layers on the top. Meanwhile, the device size should be able to scale down to the dimension of tens of nanometers, which shows its potential for practical applications in memory and logic.

Chapter 5
Ir-enabled Field-free Spin-orbit-torque Switching of Perpendicular Magnetic Tunnel Junction Device

In this chapter, we continue to explore the potential of the Ir-enabled field-free switching scheme. We would like to combine the switching scheme with the perpendicular MTJs (p-MTJs) and build the three-terminal MTJ device that doesn't require an external field to operate. This chapter is divided into two parts: the first part focuses on the experimental development of p-MTJs; in the second part, the p-MTJ is directly integrated with our Ir-enabled field-free switching scheme, where we experimentally demonstrate the field-free spin-orbit-torque (SOT) switching of p-MTJs via utilizing Ir as the material of a dual-function: generation of SOT along with mediating an in-plane field. The device we use adopts the usual three-terminal device design and doesn't require special engineering in device shape or inserting other functional layers. We show that the Ir-enabled field-free device exhibits reliable writing and reading operations, moving a step closer to the practical applications of SOT-related magnetoresistive devices.

5.1 Development of p-MTJs

Although lots of works have been reported in the p-MTJ development, to our experience we notice that the optimal parameters in fabricating MTJ can vary from facilities to facilities. Hence, here we show the process for developing the basic p-MTJs. The purpose is to be able to fabricate usable p-MTJs serving as the storage unit in the SOT device as well as to get deeper understanding of the characteristics of p-MTJ.

5.1.1 MTJ background

An MTJ consists of an insulating tunnel barrier sandwiched by two conductive ferromagnetic layers. When tunnel barrier is thin enough (usually few angstroms to few nanometers), electrons could tunnel through it due to the nature of their wave characteristics[10]. The conductance of an MTJ depends on the relative orientation of magnetizations of two ferromagnetic layers, which is expressed as

$$G(\theta) = \frac{1}{2}\left(G_p + G_{AP}\right) + \frac{1}{2}(G_P - G_{AP})cos\theta \qquad \text{Equation 5.1}$$

where G_P and G_{AP} are the conductance when magnetizations of two ferromagnetic layers are parallel and antiparallel, respectively. θ is the angle between two magnetization orientations. An MTJ has the lowest resistance when two magnetizations are parallel while having the highest resistance when two magnetizations are antiparallel (Figure 5.1). The tunneling magnetoresistance (TMR) ratio, which measures the difference between lowest and highest resistance states, is given by

$$TMR = \frac{G_P - G_{AP}}{G_{AP}} = \frac{R_{AP} - R_P}{R_P} \qquad \text{Equation 5.2}$$

where R_P and R_{AP} are the resistance when magnetizations of two ferromagnetic layers are parallel and antiparallel, respectively. In an MTJ, one of the ferromagnetic layers is usually magnetically harder (by controlling the thickness or coupling with other magnetic layers) than the other one. Due to difference in magnetic anisotropy, two orientation states, and hence two resistance states, could be obtained by applying magnetic field or current-induced spin torques.

TMR originates from the difference in the electron density states at Fermi level of majority and minority spins[10,81]. Because electron spins are conserved during tunneling, electrons can only tunnel into the sub-band of the same spin orientation. If majority-spin electrons are available for tunneling and corresponding sub-band on the other side of barrier is also majority, the resistance is low. And if the sub-band on the other side of barrier is minority instead, it results in high resistance.

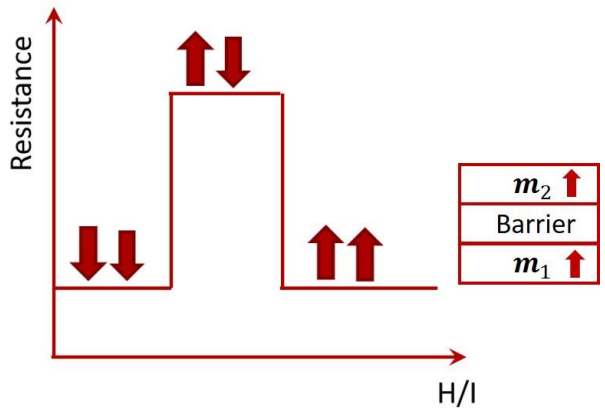

Figure 5.1 Two resistance states of an MTJ depending on the relative orientations of two ferromagnetic layers.

The first room-temperature MTJ was experimentally demonstrated in 1991 with amorphous aluminum oxide barrier, which has 2.7% TMR[82]. People later reported higher TMR up to 70% by using ferromagnetic electrodes with larger polarization factors, such as Fe[83], Co[84] and FeCoB[8]. In 2001, it was theoretically predicted that MTJ with MgO barrier with (001) Fe electrodes could have TMR exceeding 1000% [85][86], which was experimentally realized in 2004 with TMR over 200%[87,88]. Later, TMR over 600% was achieved in FeCoB/MgO/FeCoB stacks in which magnetization of FeCoB has in-plane direction[9]. In recent years, the MgO-barrier MTJ with perpendicular magnetic anisotropy (PMA) stands out due to the high thermal stability and good scalability[89][90], which allows for high-density memory and logic applications.

The simplest film stack of p-MTJ consists of an insulating MgO layer sandwiched by two FeCoB layers, surrounded by boron absorption layers such as Ta layers. For as-deposited MTJ films, FeCoB layers grow in amorphous phase while MgO grows in [001] direction perpendicular to the substrate. As-deposited MTJ usually has in-plane magnetization due to the shape anisotropy (demagnetization) of the film. Then the film is processed for post annealing at 250-400 ^{0}C for a period of time up to several hours. During annealing, interstitial boron diffuses out from FeCoB and is absorbed by the adjacent Ta layer due to the lower chemistry potential. It makes the leftover FeCo start to crystallize coherently based on the template provided by the (001) MgO, which results in the <001>[110]MgO || <001>[100]FeCo orientation relationship. Such coherent crystallization not only gives rise to the interfacial perpendicular anisotropy but also results in the

spin-dependent match between evanescent states within the MgO barrier and electronic states of FeCo that leads to the giant magnetoresistance.

5.1.2 Experimental development

We begin with investigating and optimizing the film properties, where the effects of FeCoB thickness and annealing temperature on the perpendicular magnetic anisotropy (PMA) are explored. Next, we fabricate the devices with the basic trilayer MTJ stacks, and study the TMR and RA properties as well as their relationship with the MgO thickness. After that, we integrate a perpendicular synthetic antiferromagnet (SAF) structure to pin the top FeCoB layer of the MTJ.

5.1.2.1 Effect of FeCoB thickness on perpendicular magnetic anisotropy (PMA)

To get perpendicular FeCoB layers, we first study the FeCoB thickness dependence of magnetic anisotropy. The FeCoB layers below and above the MgO layer are studied separately. The film stacks are substrate/ Ta(10 nm)/ FeCoB(1-2 nm)/ MgO(1 nm)/ Ta(2 nm) (denoted as the bottom FeCoB stack) and substrate/ Ta(10 nm)/ MgO(1 nm)/ FeCoB(1.2-2.1 nm)/ Ta (10 nm) (denoted as the top FeCoB stack). The films are then processed for post-annealing at 300 ^{0}C for 10 min. An external field of 5 kOe is applied during post-annealing, which is normal to the film surface. Hysteresis loops are measured by AGFM. Figure 5.2 shows the examples of hysteresis loops of the films with 1 nm and 2 nm bottom FeCoB layers. It can be seen that the film with the thinner FeCoB layer has a perpendicular easy axis while the other one has the easy axis lying in the film plane.

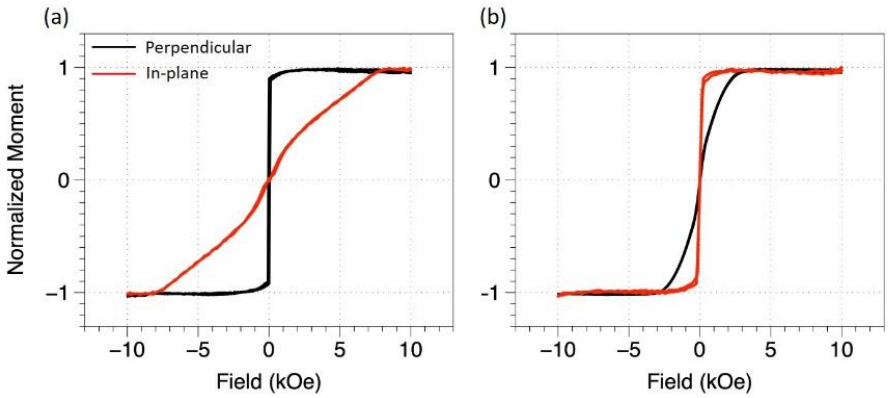

Figure 5.2 Hysteresis loops of the bottom FeCoB stacks with (a) 1.2 nm and (b) 2 nm FeCoB layer.

From the hysteresis loops of the stacks with the varying FeCoB thickness, we can evaluate the effective anisotropy of the FeCoB layers. We calculate the effective anisotropy of FeCoB layers by $K_{eff} = \frac{H_k M_s}{2}$, where H_k is the anisotropy field determined from the saturation field in the hard-axis loop and M_s is the saturation magnetization. Here, H_k is a positive (negative) value for the perpendicular (in-plane) films. M_s of FeCoB is measured to be 585.4 emu/cc. Figure 5.3 shows the thickness dependent effective anisotropy K_{eff} of both the bottom and top FeCoB layers. In general, the two K_{eff} curves follow the similar trend but the curve of the top FeCoB stacks is right shifted compared with that of the bottom FeCoB stacks. It was reported that such difference is due to that top and bottom FeCoB layers have different thicknesses of the so-called "magnetic dead layer"[89]. Such magnetic dead layer is formed due to the high concentration of boron near the FeCoB/ Ta interface, thus making part of the FeCoB layer non-magnetic. One evidence of the dead layer in our films is that we observe no magnetic signal when the FeCoB layer thickness is below some critical value, i.e. 0.6 nm–0.8 nm. Figure 5.3 implies that dead layer in top layer should be 0.1-0.2 nm thicker than that in bottom layer. In addition, we observe that K_{eff} is initially positive and increases with FeCoB layer thickness to reach a peak, and then drops to a negative value.

In our case, K_{eff} consists of the three terms as

$$K_{eff} t_{FeCoB} = K_u t_{FeCoB} - 2\pi M_s^2 t_{FeCoB} + K_s \qquad \text{Equation 5.3}$$

where the first term is the magnetocrystalline anisotropy, the second term is the shape anisotropy and the last term is the interfacial perpendicular anisotropy. Here, K_u is negligible because FeCo has a BCC lattice structure that is isotropic along all primitive axes. Shape anisotropy results from the demagnetization and it pulls the magnetization into the film plane. K_s arises from the FeCoB/MgO interface and more specifically, from the hybridization of 3d orbital of Co/Fe with 2p orbital of O at the interface[89][91][92]. When the FeCoB layer is very thin, the in-plane demagnetization is small while the interfacial perpendicular component dominates. The initial increase in K_{eff} with thicker FeCoB should result from the better developed FeCo/ MgO interface that results in more Fe/Co-O bonds. As the FeCoB layer becomes thicker, shape anisotropy gradually overcomes interfacial anisotropy and thus the easy axis leans towards the in-plane direction. Above some threshold thickness (1.7-1.9 nm), the FeCoB layer becomes totally in-plane.

From Equation 5.3, we can estimate K_s by getting the y-intercepts of the thickness dependence curves, which give us $K_s = 1.2$ ergs/cm^2.

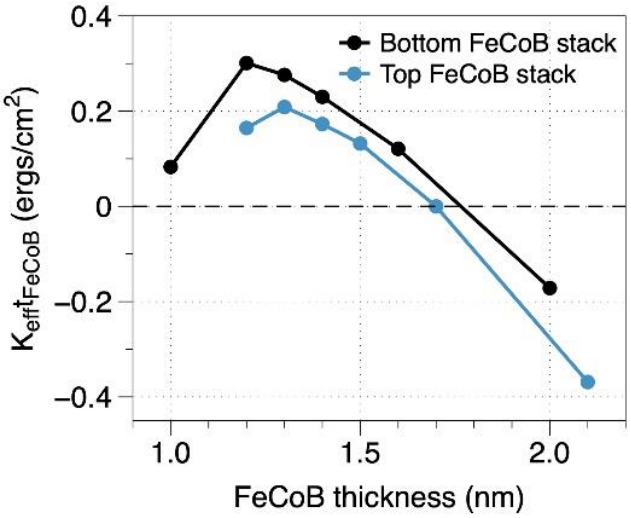

Figure 5.3 Effective anisotropy as a function of FeCoB thickness.

5.1.2.2 Effect of annealing temperature

Next, the top and bottom FeCoB stacks with the highest K_{eff} are selected for the annealing temperature study. They are annealed at different temperatures ranging from 250 ^{0}C to 375 ^{0}C. Figure 5.4 shows the change of K_{eff} as a function of the annealing temperature. We can see that moderate annealing (200^{0}C – 325^{0}C) significantly enhances K_{eff}. It's reasonable because the annealing helps boron diffuse out of FeCo into the Ta layer and thus FeCo coherently crystalizes from the interface with MgO, resulting in a sharper FeCo/MgO interface that increases the PMA. As shown in Figure 5.4, K_{eff} of the bottom FeCoB stack reaches a peak at 300^{0}C while the top FeCoB stack at 325^{0}C. The difference may be due to that the top FeCoB stack is slightly thicker than the bottom stack and thus needs higher temperature for the full boron diffusion. After annealing at the temperature above 350 ^{0}C, the sharp decrease in K_{eff} of both the top and bottom stacks is observed. Such drop can be explained by that the interdiffusion between the FeCoB and MgO layers becomes significant at high temperature and gives non-uniform interface. Additionally, Ta has also been observed to be able to penetrate through the FeCoB layer and travel into the MgO layer[93], substantially reducing the interfacial perpendicular anisotropy.

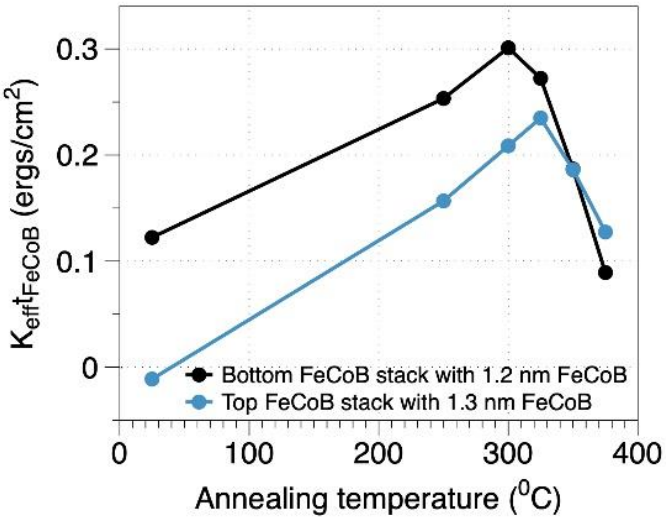

Figure 5.4 Effective anisotropy vs. annealing temperature.

5.1.2.3 Basic MTJ stack

After characterizing the top and bottom FeCoB layers individually, here we combine them and deposit the basic MTJ stack consisting of Ta(10 nm)/ FeCoB(1.2 nm)/ MgO(1 nm)/ FeCoB(1.3 nm)/ Ta(10 nm). The magnetic property is shown in Figure 5.5. As can be seen, the film demonstrates well-defined PMA. The small-field perpendicular loop contains two switching steps corresponding to the two FeCoB layers. We also observe a slope change in the in-plane curve, with one starting from 10 kOe and the other one from 6 kOe, which correspond to the H_k of bottom and top FeCoB layers, respectively.

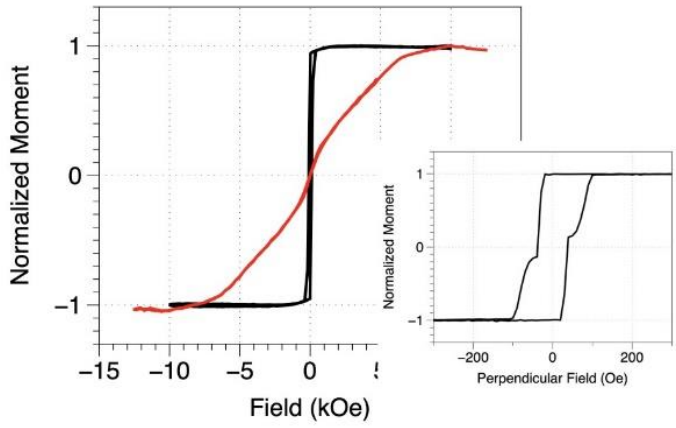

Figure 5.5 Hysteresis loops of the MTJ stack with 1 nm MgO. Inserted: small-field perpendicular M-H loop.

Now let's move on to the TMR and RA properties of the MTJ. We fabricate the two-terminal MTJ devices. The electrical measurement results in Figure 5.6(b) show how the junction resistance changes as a function of the perpendicular magnetic field of a 100-nm-diameter MTJ annealed at 300 ^{0}C. Clear low- and high-resistance states are demonstrated with TMR of around 92%. We also notice that the coercive field in the TMR loop is much larger than that in the film hysteresis loop, which can be due to the suppression of domain formation in the nanoscale devices. The blue dashed line in Figure 5.6(b) is the TMR minor loop of the free layer. The minor loop is not symmetric but shifts to the left by 400 Oe. Such shifting in the free layer switching is caused by the fringing field from the other magnetic layer[94].

In addition, we characterize TMR at difference post-annealing temperatures, as shown in Figure 5.6(c). The TMR value first increases with higher annealing temperature, reaches the peak of 92% at 300 ^{0}C, and degrades afterwards. The degradation is likely to be caused by the diffusion of low spin-polarization elements (such as Ta and B) into the MgO layer at high temperature.

RA is also an important property for evaluating the performance of MTJ. Since the main contribution to RA comes from the MgO barrier, MTJ devices with different MgO thickness are then fabricated in order to investigate the RA. Figure 5.7(a) shows the RA of the junction as a function of MgO thickness. The RA increases exponentially with MgO thickness, indicating a typical tunneling behavior[88]. Figure 5.7(b) plots the relationship between TMR and RA. We can see that TMR first grows dramatically with RA and then the increasing trend becomes gradual. When the MgO barrier is too thin, there exist pin holes within the MgO layer due to non-uniform deposition and roughness from bottom layers. These pin holes act as a current-shunting path and thus both low RA and low TMR are observed. As MgO thickness increases, the barrier becomes a more developed and continuous layer, allowing complete coherent tunneling to occur in the device. It gives rise to a sharp increase in the TMR. With thicker MgO barrier, the increasing trend becomes gradual. Our results suggest that there's a trade-off between high TMR and low RA. Hence, it's critical to choose the appropriate MgO thickness for the desirable MTJ depending on its usage.

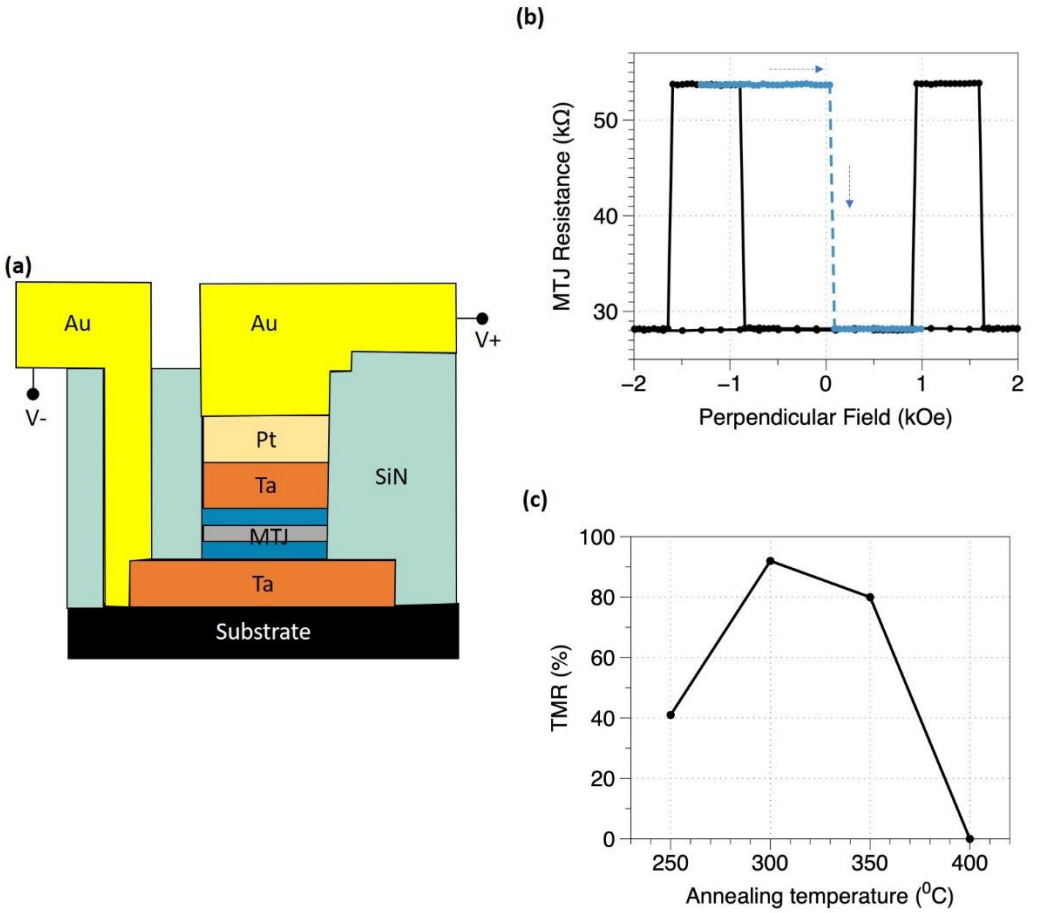

Figure 5.6 (a) Schematic of the MTJ stack and device. (b) Perpendicular-field-driven TMR loop. Blue dashed line: TMR minor loop. (c) The effect of annealing temperature on TMR.

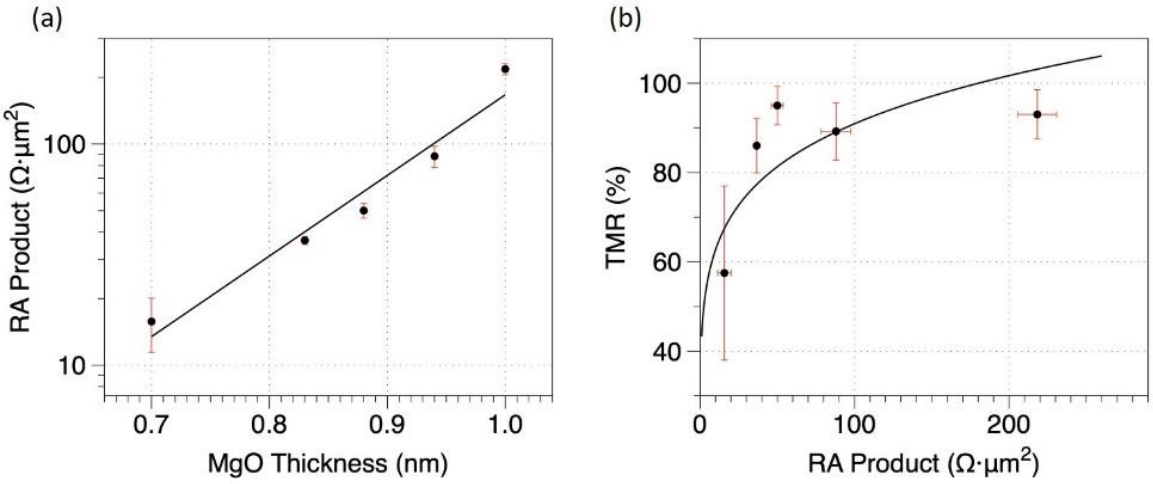

Figure 5.7 (a) RA product vs. MgO thickness. (b) TMR vs. RA product

5.1.2.4 Synthetic antiferromagnet integration

The purpose of using the synthetic antiferromagnet (SAF) structure is to minimize the effect of the stray field from the reference layer on the switching of the free layer. A SAF often consists of two magnetic components antiferromagnetically coupled by a metal spacer. For perpendicularly magnetized SAF, each magnetic component is usually made up of high magnetic-anisotropy multilayers such as [Co/Pt][95] or [Co/Pd][96] multilayers, and the metal spacer is chosen to have strong RKKY coupling at some adequate thickness, like Ru or Ir. When SAF is used in in p-MTJ, one of the magnetic components in SAF is exchange coupled with the reference layer so as to fix the moment direction of the reference layer. In addition, the moment of each magnetic component is carefully tuned in order to compensate the dipolar field from the reference layer. This can be done by adjusting the number of multilayers in the SAF.

Here we choose to develop the [Co/Pt]-multilayer-based SAF with a thin Ru spacer. [Co/Pt] superlattice is well known to be highly crystalized and have strong PMA > 10^7 erg/cm^3 while Ru is a strong RKKY material. Figure 5.8 shows the perpendicular M-H loop of an as-deposited SAF that's of substrate/ Ta (0.5)/ [Co (0.4)/Pt (1)]x3/ Co (0.6)/ Ru (0.8)/ Co (0.6)/ [Pt (1)/Co (0.4)]x5/ Ta (5) (unit in nm). The thickness of Ru corresponds to the second antiferromagnetic coupling peak in its RKKY curve. The hysteresis loop demonstrates clear sign of antiferromagnetic coupling that has the exchange couple field of 2.8 kOe.

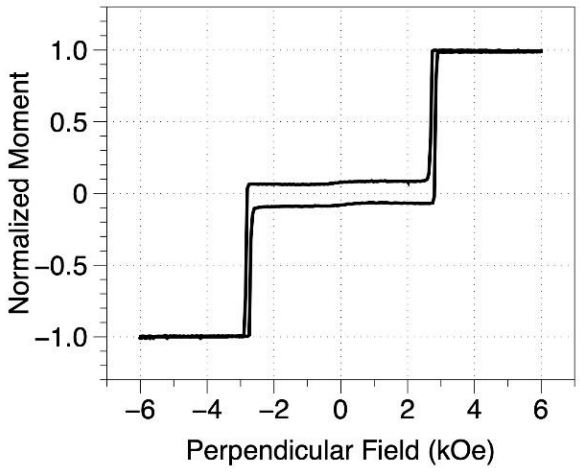

Figure 5.8 M-H loop of a perpendicular SAF showing the antiferromagnetic coupling between two [Co/Pt] multilayer stacks via Ru.

Next, we combine the SAF structure with the previously developed MTJ stack. Our goal is to minimize the minor loop shifting of the free layer. Unlike the two-terminal MTJ device usually having a bottom pinned FeCoB layer[95], here we put the SAF on top of the MTJ to pin the top FeCoB layer. This is because the bottom part in our later designed three-terminal SOT device must be a spin-current-generation channel, which means the bottom FeCoB layer should be the free layer to switch. For this study, we deposit film stacks consisting of substrate/ Ta (10)/ FeCoB (1.2)/ MgO (0.9)/ FeCoB (1.2)/ Ta (0.5)/ [Co (0.4)/Pt (1)] x 3/ Co(0.6)/ Ru (0.8)/ Co (0.6)/ [Pt (1)/Co (0.4)] x X/ Ta (2) (unit in nm), as schematically shown in Figure 5.9(a). The only difference between these films is that the top [Co/Pt] multilayers in the SAF has different number of repetitions X ranging from 4 to 7. Note that the bottom [Co/Pt] multilayers in the SAF is ferromagnetically coupled with the top FeCoB layer through a 0.5 nm Ta spacer. The perpendicular loops as well as the minor loop of the free layer are shown in Figure 5.9(b). When $X = 4 - 5$, the perpendicular loop contains three switching steps. The first switching step corresponds to the switching of the exchange coupled [Co/Pt] multilayers and the top FeCoB layer (denoted as M2). This switching occurs at a positive field because the antiferromagnetic characteristics of the SAF favors the anti-aligned configuration of the magnetic moments. The second switching step is relatively small, corresponding to the switching of the bottom free FeCoB layer (denoted as M1). The last switching happens at a large negative field, indicating the switching of the top [Co/Pt] multilayers (denoted as M3), and this switching step becomes larger as X increases. Interestingly, when $X = 6 - 7$ an additional switching step is observed. The extra switching was also found elsewhere[97]. The reason is that as the moment difference between M1 and M2 becomes larger, there exists another anti-aligned configuration where M2 and M3 flip simultaneously due to the strong antiferromagnetic coupling, as illustrated in Figure 5.9(b). The effect of X on the minor loop is shown by the shifting of the minor loops. With $X = 4$, M2 is not fully compensated and so the bottom free FeCoB layer favors down state. The minor loop then shifts to the left upon increasing X. With $X = 5 - 6$, the free layer shows bi-stable states at zero field. Hence, $X = 5 - 6$ are good choices to use in our p-MTJs. Furthermore, we characterize the TMR and RA product on the film with $X = 5.5$ by the current-in-plane tunneling (CIPT) technique. It gives about 70% TMR with 50 $\Omega \cdot \mu m^2$ RA product, which are comparable to what we obtained in the MTJ without the SAF.

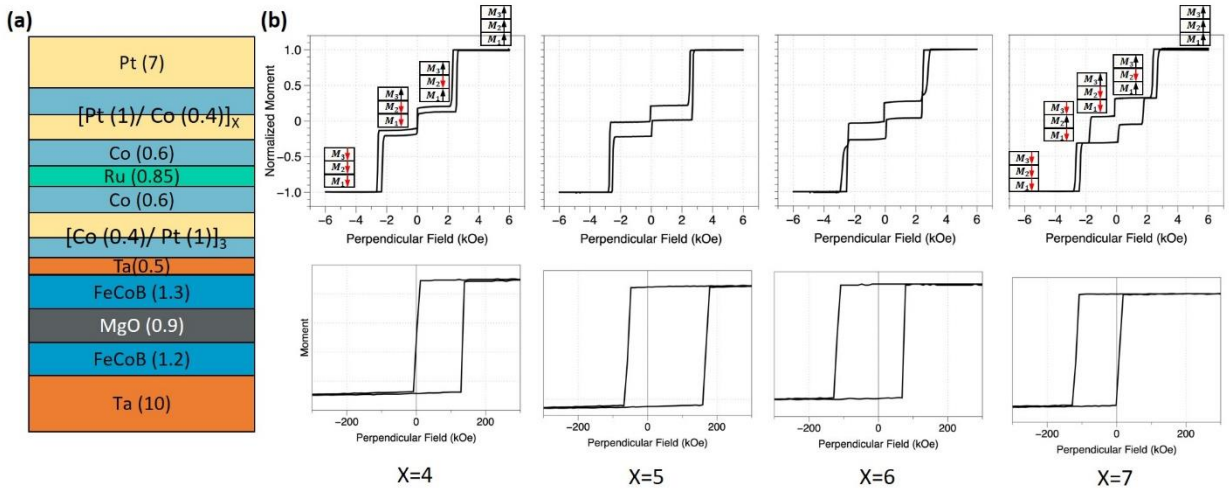

Figure 5.9 (a) The film stack of the MTJ with a top SAF. (b) Top: large-field perpendicular hysteresis loop of the films. Bottom: small-field minor loop of the free FeCoB layer. *X* is the number of repetitions of the [Co/Pt] multilayers in the top part of the SAF.

5.2 Experimental development of the field-free three-terminal SOT device

Now that we are able to fabricate switchable and readable p-MTJs, let's move on to combine the p-MTJs with the Ir switching scheme. In the following sections, we first study the effect of annealing on the interlayer exchange coupling (IEC) of Ir because annealing is necessary for the MTJ devices. Next, we explore the appropriate way to integrate the p-MTJ via examining the switching of a free FeCoB layer. After obtaining the robust switching of the free layer, we fabricate three-terminal SOT devices with nanoscale p-MTJs and characterize their switching profiles.

5.2.1 Thermal stability of the interlayer exchange coupling via Ir

So far, the field-free-switching devices haven't been processed with any heat treatment (except that the chips are baked at 95 ^{0}C for few minutes during Hall-bar device fabrication). But in order to integrate p-MTJs, annealing at 300 ^{0}C or above is often required. Thus, we would like to ensure that the film or device property won't degrade a lot after annealing, especially for the IEC that plays a critical role in the device functioning. Hence, the effect of annealing on the IEC is explored. Film stacks containing the sandwich structure Co (1.1 nm or 2 nm)/ Ir (1.35 nm)/ Co (1.1 nm or 2 nm) are deposited. The Co thickness is varied so that both perpendicular and in-plane IEC will be studied. The films are post-annealed at 300 ^{0}C for 10 min. Figure 5.10 shows the IEC via the 1.35-nm Ir before and after annealing. Interestingly, the in-plane exchange coupling

disappears almost completely while the perpendicular exchange coupling remains after annealing. One possible cause for the IEC degradation is that interdiffusion takes place during annealing so that the Ir spacer contains some Co contaminations. As the two films are processed with the identical annealing conditions, however, the interdiffusion can't explain that why the perpendicular exchange coupling still holds after annealing. It was also reported that Co has a low solubility in Ir up to 1000 ^{0}C[98], suggesting the interdiffusion in our films should be negligible. To best of our knowledge, we speculate that what actually happens is that the moderate annealing smooths out the films and helps form more Ir-Co bonds at the Ir/Co interface (in other words, the Ir/Co interface becomes more crystalline). As a result, the perpendicular moments become dominant at the Ir/Co interface. Because RKKY interaction is an interfacial phenomenon, the reduction of in-plane moment at the Ir/Co interface gives arise to the degradation of the in-plane exchange coupling.

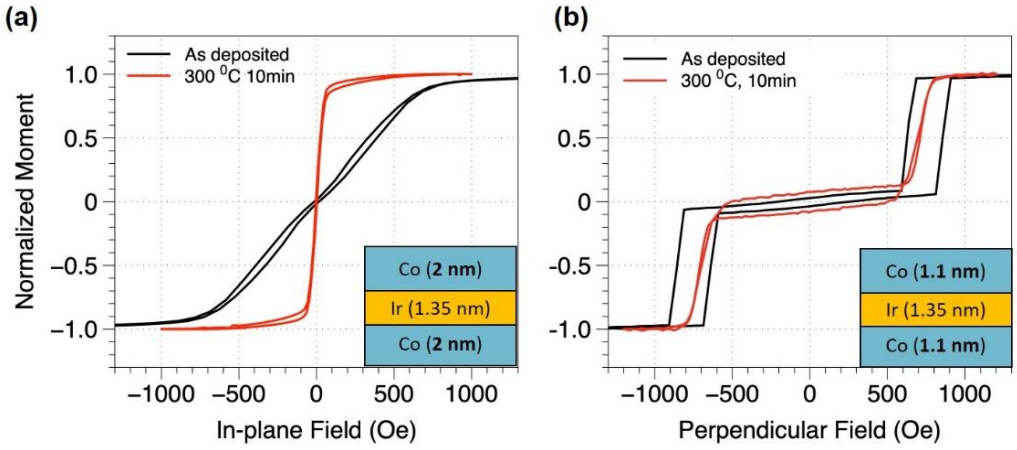

Figure 5.10 The effect on annealing on IEC. (a) In-plane exchange coupling in Co (2 nm)/ Ir (1.35 nm)/ Co (2 nm). (b) Perpendicular exchange coupling in Co (1 nm)/ Ir (1.35 nm)/ Co (1 nm)

The large degradation of in-plane exchange coupling will detrimental for our SOT devices because the local in-plane coupling field for the field-free switching is much reduced. To solve this problem, we incorporate an antiferromagnetic IrMn layer in order to pin the one of the Co layers entirely along the in-plane direction. Using an antiferromagnetic layer to fix the moment direction of the adjacent ferromagnetic layer is a commonly used technique in spin valves[6,99]. Our idea here is that by forcing one of the Co layers to align along an in-plane direction the formation of the perpendicular bonds at the interface can be reduced during annealing, and this pinned layer can also help align the other Co layer by IEC via Ir. In this way, the in-plane exchange coupling

will be retained. We deposit the film stack consisting of substrate/ Ru(2 nm)/ $Ir_{20}Mn_{80}$ (5 nm)/ Co(2 nm)/ Ir (1.35 nm)/ Co(2 nm)/ Ta. The film is annealed at 300 ^{0}C for 10 min in presence of a 5 kOe magnetic field parallel to the film plane. We then measure the in-plane hysteresis loop along the annealing field direction. In Figure 5.11. Clear evidence of antiferromagnetic coupling via the 1.35-nm Ir is observed after annealing, which is largely improved compared to the case without having the bottom IrMn (Figure 5.10(a)). We notice that the magnitude of the coupling field is about 500 Oe, still lower than the coupling field before annealing. On the other hand, the pinning field of IrMn is quite large, around 1250 Oe.

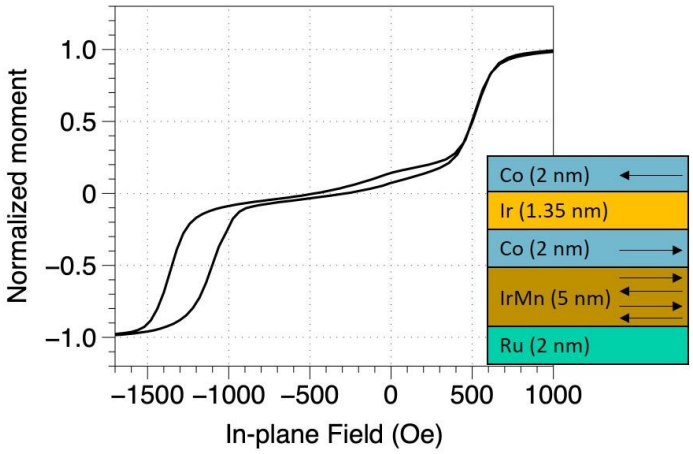

Figure 5.11 In-plane hysteresis loop of the film with a bottom IrMn layer. The film is post-annealed at 300 ^{0}C for 10 min in presence of a 5 kOe magnetic field parallel to the film plane. The loop is measured along the annealing field direction.

5.2.2 SOT switching of a perpendicular FeCoB layer

Before integrating with the full stack of p-MTJ, we first investigated the SOT switching of a single FeCoB layer that's designated to be the free layer in the p-MTJ. Since we've already obtained the field-free switching of a perpendicular Co layer as described in Chapter 4, a natural way is that we simply couple the FeCoB layer with the perpendicular Co layer so that the switching of the Co layer simultaneously triggers the switching of the FeCoB layer. For that purpose, we fabricate the film stack consisting of substrate/ Ru(2 nm)/ $Ir_{20}Mn_{80}$(5 nm)/ Co(2 nm)/ Ru(0.85 nm)/ Co(2 nm)/ Ir (1.35 nm)/ Co(1 nm)/ W(0.3 nm)/ FeCoB (1.1 nm)/ MgO (2 nm)/ Ta. The FeCoB layer is ferromagnetically coupled with the perpendicular Co layer through an ultra-thin W spacer. The film is annealed at 300 ^{0}C for 10 min in presence of a 5 kOe magnetic field parallel to the film

plane. Small-field perpendicular hysteresis loop (Figure 5.12(b)) shows only one sharp switching step, indicative of the parallelly aligned perpendicular layers. Figure 5.12(c) shows the current-induced switching results measured in the Hall-bar device with 1 μm-wide current- and 1 μm-wide voltage-channels. We find that the change in anomalous Hall voltage at H_x=0 Oe is smaller than that at H_x=200 Oe, suggesting that the switching at zero field is not a full switching. The switching loop changes its polarity from H_x=50 Oe to H_x=100 Oe, which indicates that the local in-plane field in the device is between 50 Oe to 100 Oe. It's smaller than the one in the case without the post annealing (Figure 4.2). The reduction in the coupling field can be one of the reasons for the partial switching at zero field. Another possible reason for the incomplete switching is that there are larger magnetic moments to switch by the SOTs. The coupled bilayers have almost twice the moment as a single perpendicular Co layer, and thus it's harder for the same amounts of SOTs to flip the larger moment. Applying higher charge current into the device can produce more SOTs but it also generates greater joule heating at the same time. The large amount of heating in the device not only causes random domain nucleation but also destabilizes the ferromagnetic coupling between the coupled bilayers, both of which will cause the partial switching.

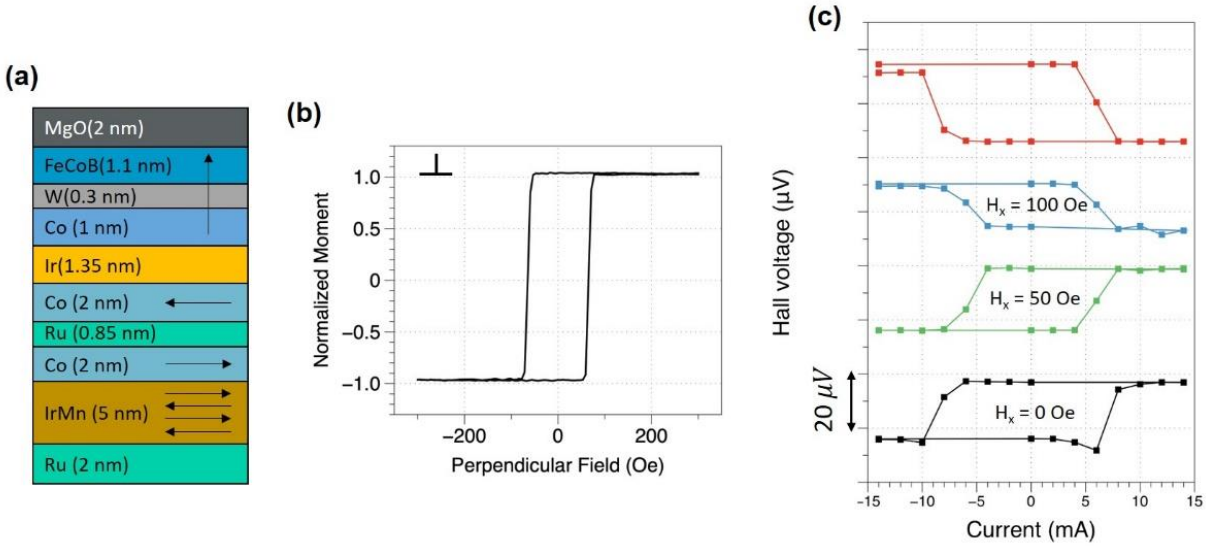

Figure 5.12 (a) Film stack for SOT switching of the coupled bilayers. (b) Small-field perpendicular hysteresis loop of the film. (c) Current-induced switching results measured in the patterned Hall-bar device.

It's not desirable to have the incomplete switching at zero field. To enhance the switching, we may either improve the IEC in our device or decrease the amount of magnetic moment for

switching. Improving the IEC doesn't seem very straightforward because it may require alternating the materials. Instead, we try to make the switching scheme simpler by replacing the bilayers with a single FeCoB layer so that the total moment to switch is reduced. There are two things to we need to verify: (1) whether there exists IEC between FeCoB and Co through the Ir and (2) whether FeCoB/ MgO has good PMA on an Ir buffer layer. For the first study, we fabricate the film of substrate/ Ru(2 nm)/ $Ir_{20}Mn_{80}$(5 nm)/ Co(2 nm)/ Ru(0.85 nm)/ Co(2 nm)/ Ir (1.35 nm)/ FeCoB (2 nm)/ MgO (2 nm)/ Ta. Figure 5.13(a) shows the in-plane M-H loop of the film after annealed at 300 ^{0}C for 10 min. One can clearly see that the FeCoB layer is anti-aligned with the Co layer via Ir. Interesting, the exchange coupling field is almost identical as the one in Co/ Ir/ Co (Figure 5.11). Note that RKKY coupling usually doesn't occur between magnetic layers composed of different materials. The antiferromagnetic coupling between FeCoB and Co may be attributed to the coexistence of Co composition in both layers. For the second study, film stack of substrate/ Ir(3 nm)/ FeCoB (1.2 nm)/ MgO (2 nm)/ Ta is deposited. The hysteresis loops of the annealed film are shown in Figure 5.13(b). The film has a clear perpendicular easy axis with an in-plane saturation field H_k =5 kOe. The study from other group also suggests that Ir is a good buffer layer material for p-MTJ in terms of getting high PMA and TMR[100].

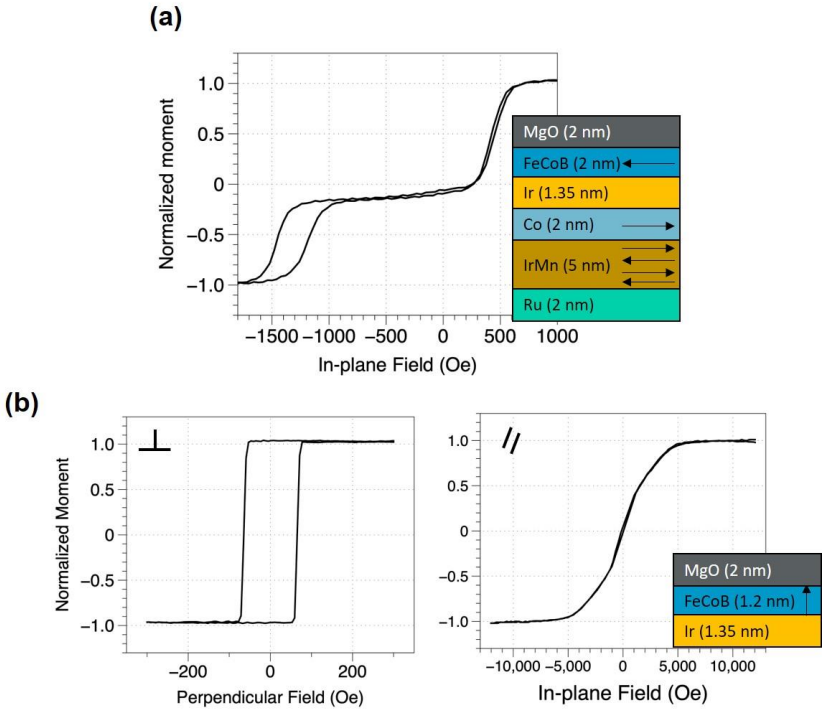

Figure 5.13 (a) In-plane M-H loop showing the IEC between FeCoB and Co via the 1.35-nm Ir spacer. (b) M-H loops demonstrating the PMA of FeCoB/ MgO on an Ir buffer layer.

Next, we move on to fabricate the film for the switching measurements. The film stack is substrate/ Ru(2 nm)/ $Ir_{20}Mn_{80}$(5 nm)/ Co(2 nm)/ Ru(0.85 nm)/ Co(2 nm)/ Ir (1.35 nm)/ FeCoB (1.2 nm)/ MgO (2 nm)/ Ta. The FeCoB layer has a perpendicular easy axis, and couples with the in-plane Co layer below Ir. Figure 5.14 shows the current switching results measured in the Hall-bar device with 1 μm-wide current- and 1 μm-wide voltage-channels. Well-defined magnetization switching loop is obtained in absence of an external field. The zero-field switching is nearly complete, much improved than the switching in the coupled bilayers. The in-plane coupling field at device level turns out to be about 100 Oe, as indicated by the collapsing of the switching loop at H_x = +100 Oe. Our results show that a FeCoB layer can be switched directly without being coupled to a switchable perpendicular Co layer. This scenario not only simplifies the film stack but also gives more robust magnetization reversal.

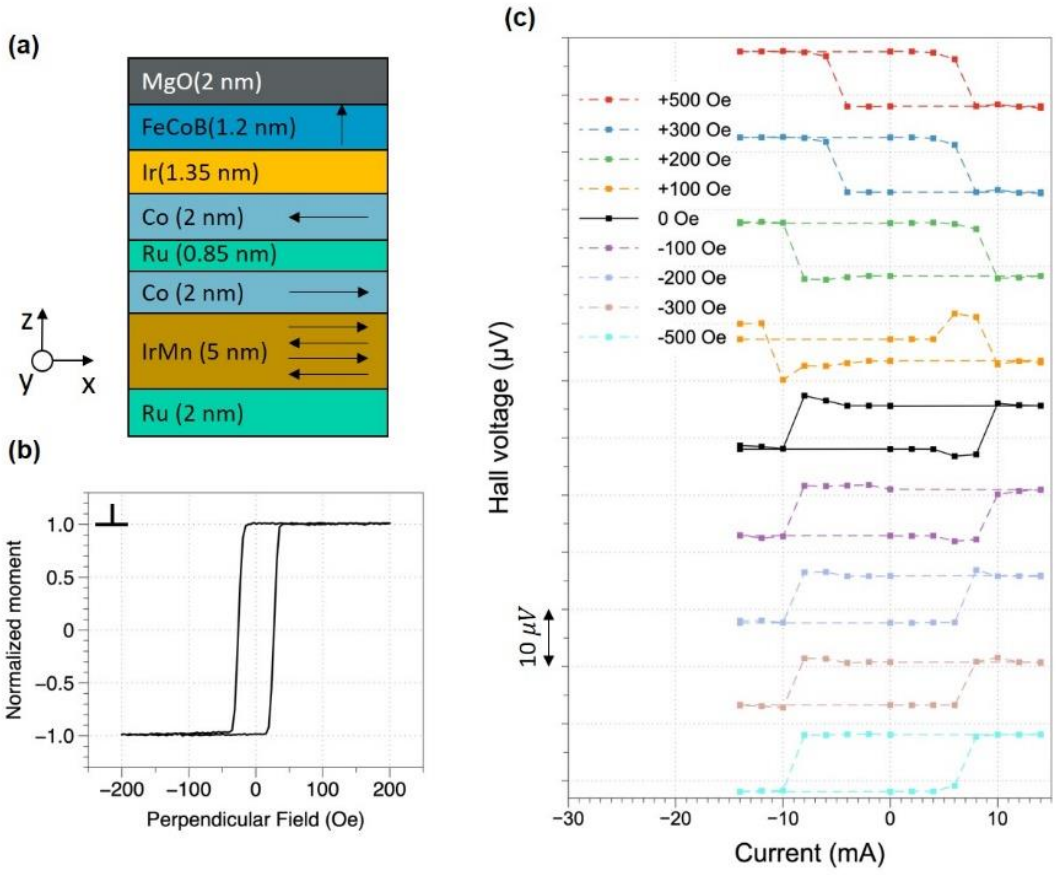

Figure 5.14 (a) Film stack for the SOT switching of the perpendicular FeCoB. (b) Small-field perpendicular hysteresis loop of the film. (c) Current-induced switching results measured in the patterned Hall-bar device.

5.2.3 Field-free SOT switching of p-MTJ device

5.2.3.1 Demonstration of the field-free switching in p-MTJ device

After getting the switching of the perpendicular FeCoB layer, we proceed to integrate the full p-MTJ stack with the Ir switching scheme. We deposit the film at room temperature by magnetron sputtering with base pressure $< 2 \times 10^{-8}$ Torr. The film structure, as shown in Figure 1(a), is substrate/ IrMn(5)/ Co(2)/ Ru(0.85)/ Co(2)/ Ir (1.35)/ FeCoB (1.2)/ MgO(1.2)/ FeCoB(1.3)/ Ta(0.5)/ $[Co(0.4)/ Pt(1)]_{3.5}$/ Ru(0.85)/ $[Co(0.4)/ Pt(1)]_{6.5}$/ Pt(7) (in nm). The purpose of using an in-plane SAF instead of a single in-plane Co layer is to minimize the effect of the in-plane stray field on the perpendicular SOT switching. The thickness of the Ir layer corresponds to the second antiferromagnetic coupling peak in the Ruderman–Kittel–Kasuya–Yosida (RKKY) thickness dependence curve. After deposition, the film is post-annealed at 300 ^{0}C for 10 min with a 5000 Oe magnetic field applied along -x direction. Figure 5.15(a) also shows the hysteresis loops of the film, exhibiting the well-defined PMA of the MTJ.

The deposited film is processed into three-terminal magnetoresistive devices (Figure 5.15(b)). In the device fabrication process, the MTJ pillar etching is controlled carefully so that the ion milling is stopped right after the MgO layer being etched, and thus the write path contains the Ir layer. The tunnel magnetoresistance ratio (TMR) is evaluated by measuring the resistance of MTJ with varying the perpendicular magnetic field. Figure 5.15(b) shows the TMR minor loop of 1.2-nm-thick free FeCoB layer of the device with a 150 nm-diameter MTJ. Bi-stable states of the low and high resistance of the MTJ is observed at zero field. The TMR is about 60%, with the abrupt magnetization reversal of the free layer.

In current-induced switching measurements, 200-ns current pulses are applied into the write path consisting of the Ir layer and the bottom pinned in-plane SAF structure. We connect a 10 MΩ resistor in series with the MTJ to reduce the bias voltage across the MgO layer. The resistance change of the MTJ is monitored by the lock-in technique. Figure 5.16(b) shows the well-defined current-induced switching of the MTJ at zero external field. Starting with a low-resistance state of MTJ and sweeping the current from positive to negative, a sharp increase in the MTJ resistance is observed when the current is below a negative threshold value, indicating the parallel (P) to antiparallel (AP) magnetization switching. Next, as the current is swept back to a sufficiently large

positive value, the switching is reversed (AP to P switching), as shown by the abrupt drop in MTJ resistance. By applying a sequence of switching pulses (Figure 5.16(c)), the devices exhibit reliable zero-field switching capability, where the MTJ can be switched repeatedly between low and high resistance states with applied current of opposite polarities.

To further study the switching behaviors, an external in-plane field H_x is applied during the current switching measurements. In Figure 5.16(b), when H_x is applied along -x direction, we obtain almost identical switching behavior as the zero-field switching, i.e., the switching is clockwise. It's as expected since the exchange coupling field acting on the free FeCoB layer also lies in the -x direction due to the antiferromagnetic coupling characteristic of the 1.35 nm Ir. When the direction of H_x is reversed, the switching loop becomes counter-clockwise. It's due to that the anti-aligned H_x now overcomes the local exchange coupling field (~100 Oe, see Figure 5.14) and thus the net field acting on the free FeCoB layer is along +x direction, leading to the opposite switching outcome.

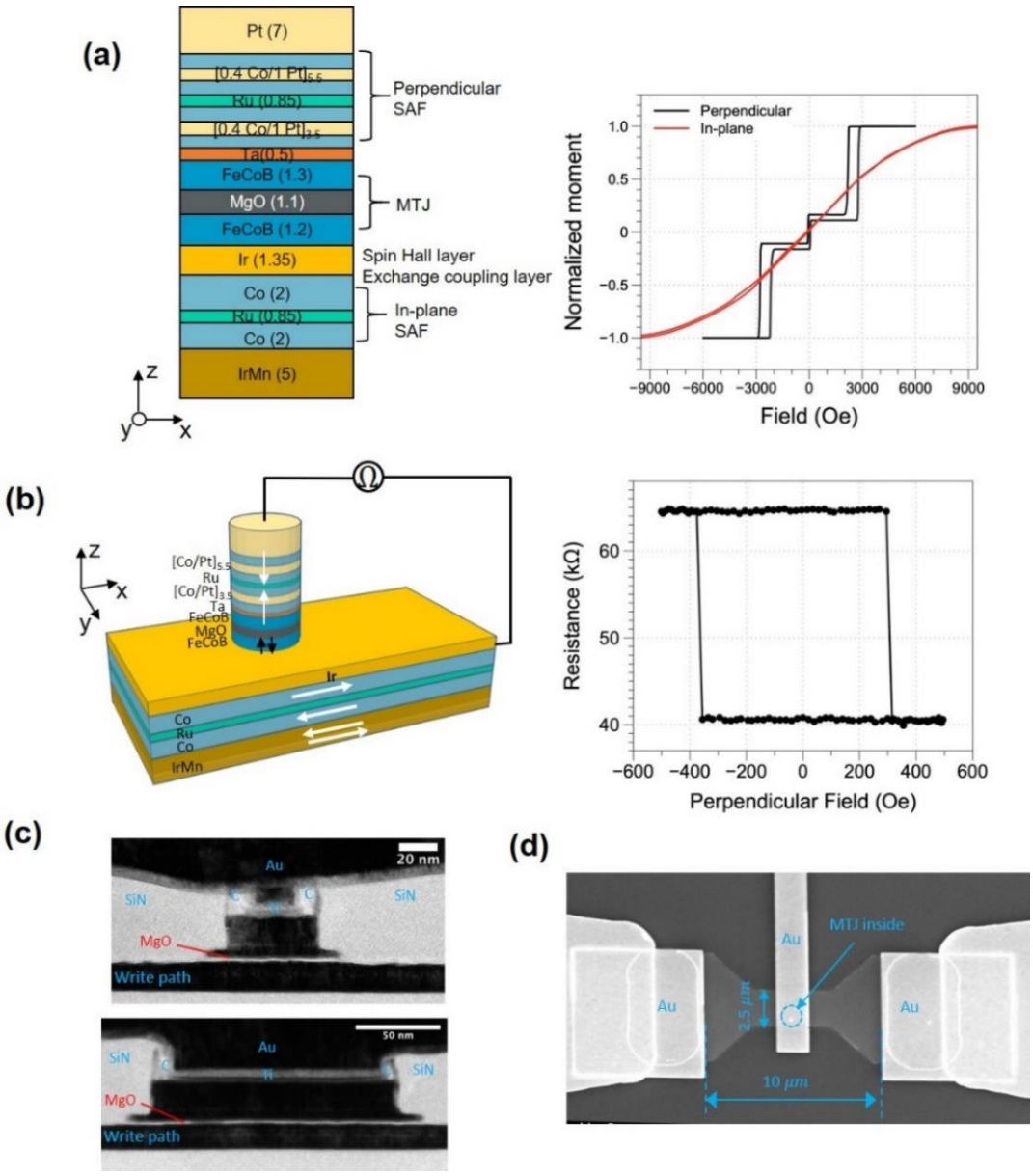

Figure 5.15 (a) Left: film stack, unit in nanometer. Right: M-H loops of the film. (b) Left: schematic of the device and testing set-up. Right: Perpendicular-field-driven TMR minor loop of a device with a 150-nm-diameter MTJ. (c) Cross-section TEM images of the devices with a 50-nm-diameter MTJ and a 150-nm-diameter MTJ. (d) Top-view SEM image of the device.

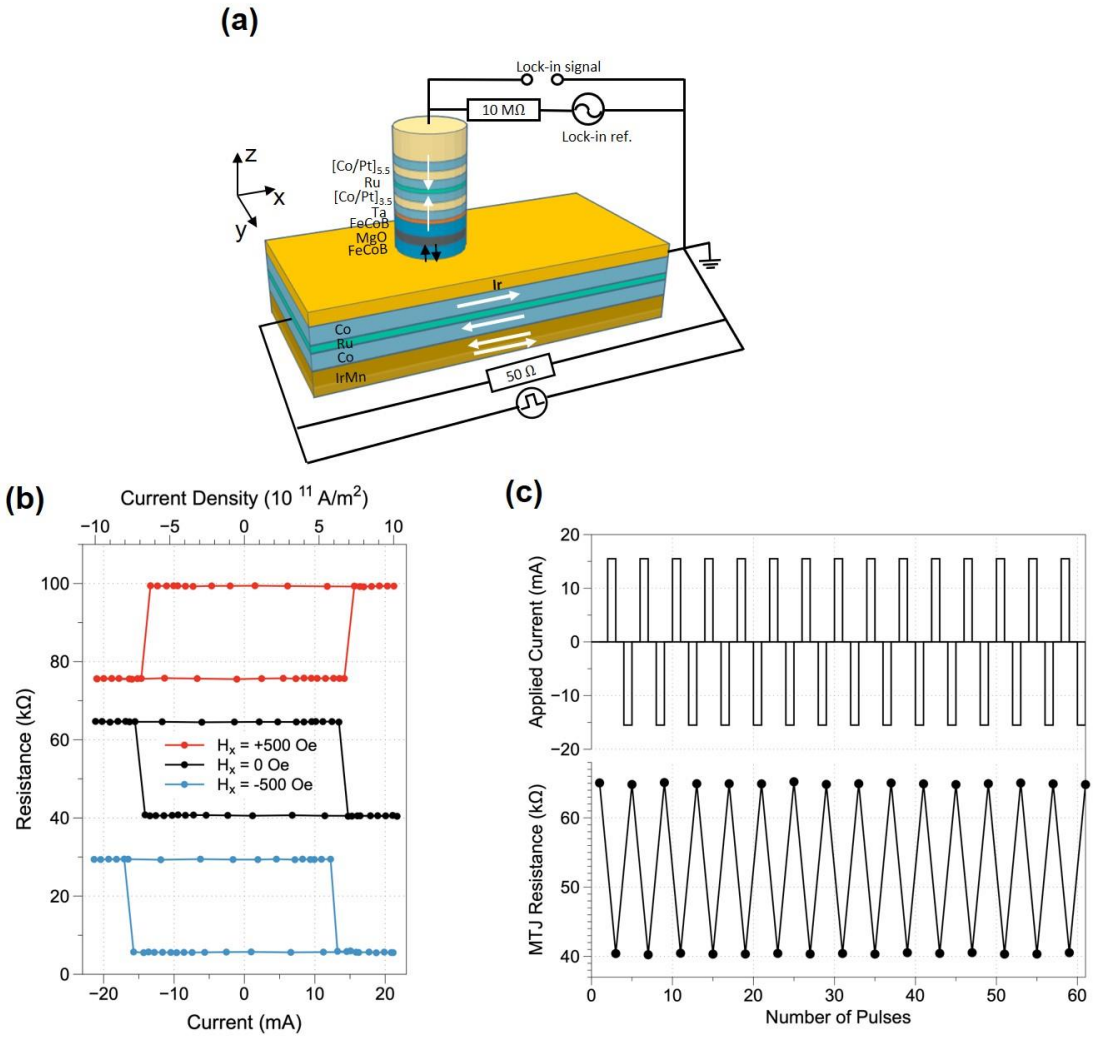

Figure 5.16 (a) Illustration of the testing set-up. (b) Current-induced switching w/o an externally applied field along current direction. The device has a 2.5 μm-width write path and a 150-nm-diameter MTJ. (c) Zero-field switching of the p-MTJs with applying a sequence of positive and negative switching pulses.

5.2.3.2 Effect of device size

Next, we compare the switching current for the devices with different sizes. In Figure 5.17(a), the results show that the switching current is linearly proportional to the width of the write path. The linear relationship can be interpreted by the fact that the SOT switching condition is determined by the current density instead of absolute current in the write path[18,19]. Furthermore, we study the effect of MTJ size on the switching current threshold. As shown in Figure 5.17(b), no significant change in the switching current is observed with MTJ sizes ranging from 500 nm to 150 nm while the switching current starts to increase as the MTJ size becomes smaller than 80 nm. To explain such trend in the switching current, we conduct micromagnetic simulations to compare the switching processes in devices with different sizes. Figure 5.18(a) illustrates the switching dynamics of the free FeCoB layer in a relatively large (240 nm x 240 nm) device. It's found that the switching starts with nucleation and formation of dense strips of reverse domains followed by rather complex expansion and merge of these reverse strip domains until the full reversal of the magnetic layer is reached. Note that such SOT resulted nucleation and expansion of reverse strip domains has been observed with utilization of Kerr microscopy in our previous experiments (Figure 4.6). In Figure 5.18(b), we show the initially formed reverse domain for five difference device sizes ranging from 300 x 300 nm^2 to 30 x 30 nm^2. Note the size of each reverse strip domain is essentially independent of device size. As the size of the free layer goes down, we observe the reducing number of domains. When the size is reduced below 60 nm, only a single reverse strip domain would nucleate under the SOT in the presence of the in-plane exchange field and thus near single domain switching is observed. Such transition from multi-domain switching in large devices to single domain switching in smaller devices causes a slight increase in the calculated switching current, as shown in Figure 5.18(c). The simulated trend of the switching current as a function of MTJ size agrees well with our experimental results (Figure 5.17(b)).

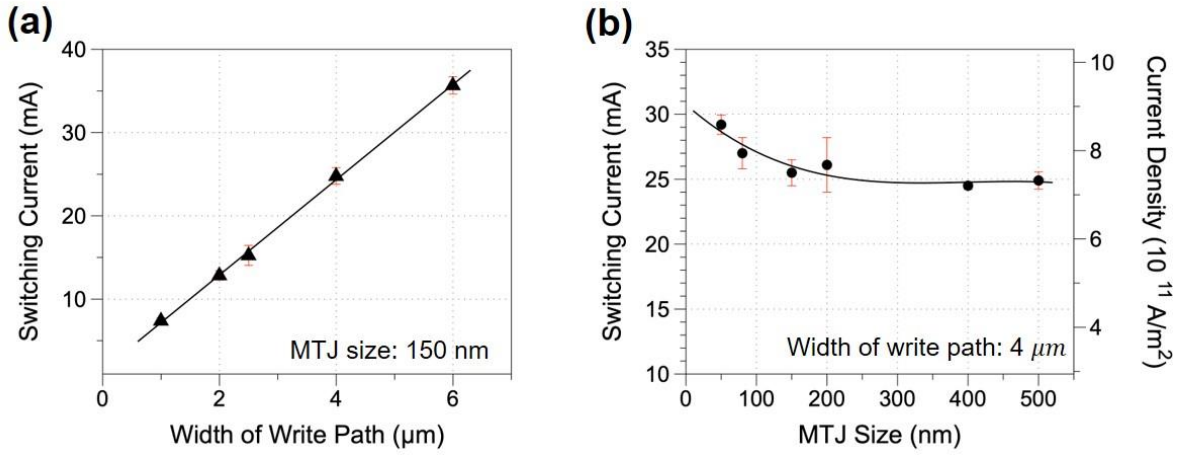

Figure 5.17 Measured switching current as a function of (a) the width of the write path and (b) the MTJ size.

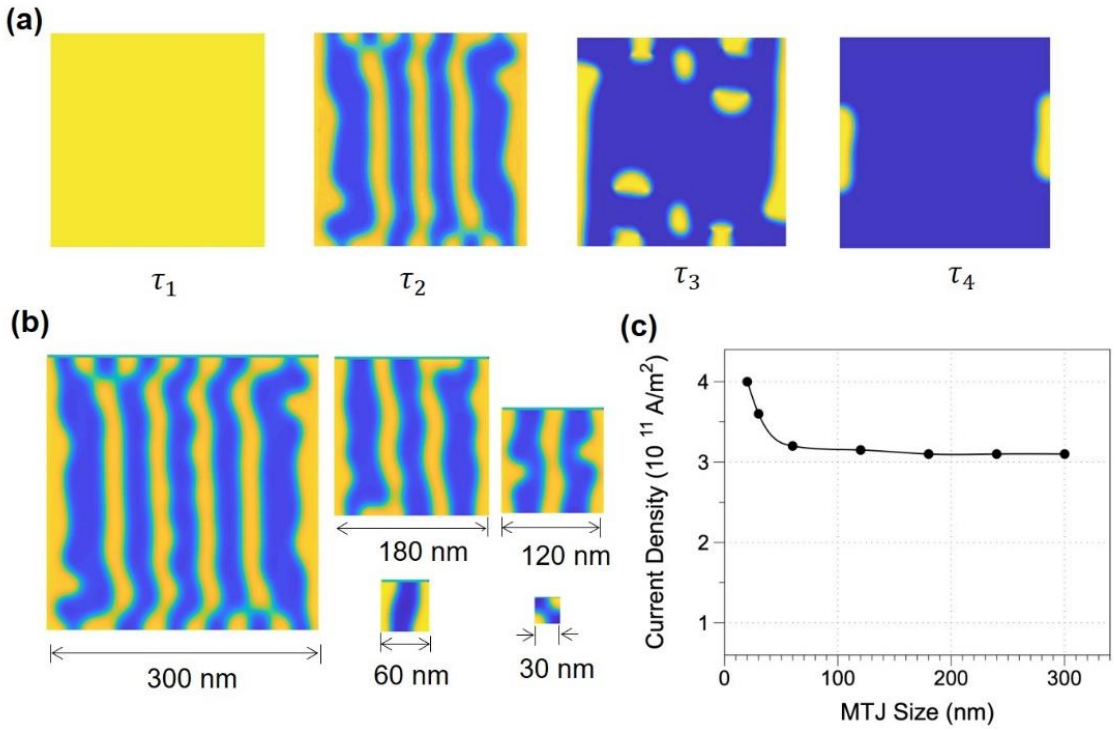

Figure 5.18 (a) Zero-field switching dynamics of the free FeCoB layer in a 240 nm x 240 nm device. Time: $\tau_1 < \tau_2 < \tau_3 < \tau_4$. (b) Comparison of the switching in devices with various sizes. (c) Simulated trend in the switching current as a function of MTJ size.

5.2.3.3 Effect of pulse width

We then study the effect of pulse width on the switching current threshold. The duration of current pulse is varied from 20 ns to 5 μs and the effect on the critical switching current is plotted in Figure 5.19(a). Interestingly, at current pulse width below 100 ns, the switching current value is essentially a linear function of inverse $\sqrt{\tau}$. When current pulse width is beyond 100 ns, the switching current levels off to almost a constant value.

Combined micromagnetic simulation (Figure 5.19(b)) using all measured properties of the fabricated MTJ stack suggests that the SOT switching in our devices should occur within 1 ns. Furthermore, the simulation shows that when the pulse width becomes longer than 1 ns, the switching current threshold should become a constant value, no longer depending on the pulse width. However, the measured switching current dependence on pulse width ranging from 20 ns and 100 ns evidently disagree with the micromagnetic simulations. The most plausible reason for the difference should be that no thermal effect is considered in the initial simulation, but noticeable amount of joule heating can be generated during the current pulse injection in the switching measurement. The joule heating can effectively reduce the PMA of the free layer, further causing the change in the switching current threshold. By varying the PMA of the free layer, our simulation shown in Figure 5.20(a) indicate a linear relationship between the critical switching current and the perpendicular anisotropy of the free layer.

Previous study has found that the perpendicular anisotropy of FeCoB/MgO decreases linearly with temperature, with a measured Blocking temperature at T_B = 450K at which the anisotropy vanishes[101]. Assuming the same Blocking temperature for the free layer fabricated here, the temperature dependence of the interfacial perpendicular anisotropy of the free layer is

$$K(T) = K_0\left(1 - \frac{T - T_{RT}}{T_B - T_{RT}}\right) \qquad \text{Equation 5.4}$$

where K_0 is the perpendicular anisotropy constant at room temperature T_{RT}. With a current pulse of duration τ, the temperature rise of the write wire underneath the free layer of the MTJ can be written as

$$T - T_{RT} = \frac{\left[I^2 R - k_{dissp}\left(T - T_{RT}\right)\right] \cdot \tau}{C \cdot V} \qquad \text{Equation 5.5}$$

Where $k_{dissp}\left(T - T_{RT}\right)$ is the power of heat dissipation, $CV_{effective}$ is the heat capacitance, I is the current and R is the resistance of the write path. Combining the two above equations with this linear dependence in Figure 5.20(a), we have

$$I = \frac{I_o}{\left(K_0 - 2\pi M_S^2\right)} \left\{ K_0 \left(1 - \frac{I^2 R}{\left(\frac{C \cdot V}{\tau} + k_{dissp}\right) \cdot \left(T_B - T_{RT}\right)} \right) - 2\pi M_S^2 \right\} \qquad \text{Equation 5.6}$$

where I_0 is the level-off switching current threshold at room temperature. The above equation should describe the switching current threshold as a function of pulse width τ, with considering the anisotropy reduction of the free layer. Figure 5.20(b) combines micromagnetic simulation results (blue curve) and measurement data (red circles) as a function of inverse pulse width. The black curves are simulation results for the free layers with varying PMA due to different joule heating, showing how the heat effect curve (blue curve) is generated. The results shown in Figure 5.20(b) provides a good understanding on the current driven perpendicular SOT switching in our devices. If the current pulse width is shorter than 1 ns, the temperature of the write wire doesn't rise and the free layer anisotropy remains unchanged. The switching current threshold follows the micromagnetic simulation result for the case with K_0. In this case, the switching occurs within a fraction of nanosecond and the threshold current will level off to a constant value for any pulse width longer than 1 ns. For the cases with current pulse width longer than 1 ns, the temperature elevates, and the PMA of the free layer decreases accordingly. The measured data is actually the level-off current threshold at different anisotropy. A longer duration pulse (for τ < 100 ns) leads to higher temperature, hence lower threshold current, until the heat generated becomes balanced by the heat dissipation. This lowest threshold current corresponding to the maximum temperature increase (from room temperature), which is 57 K in the case based on the calculation.

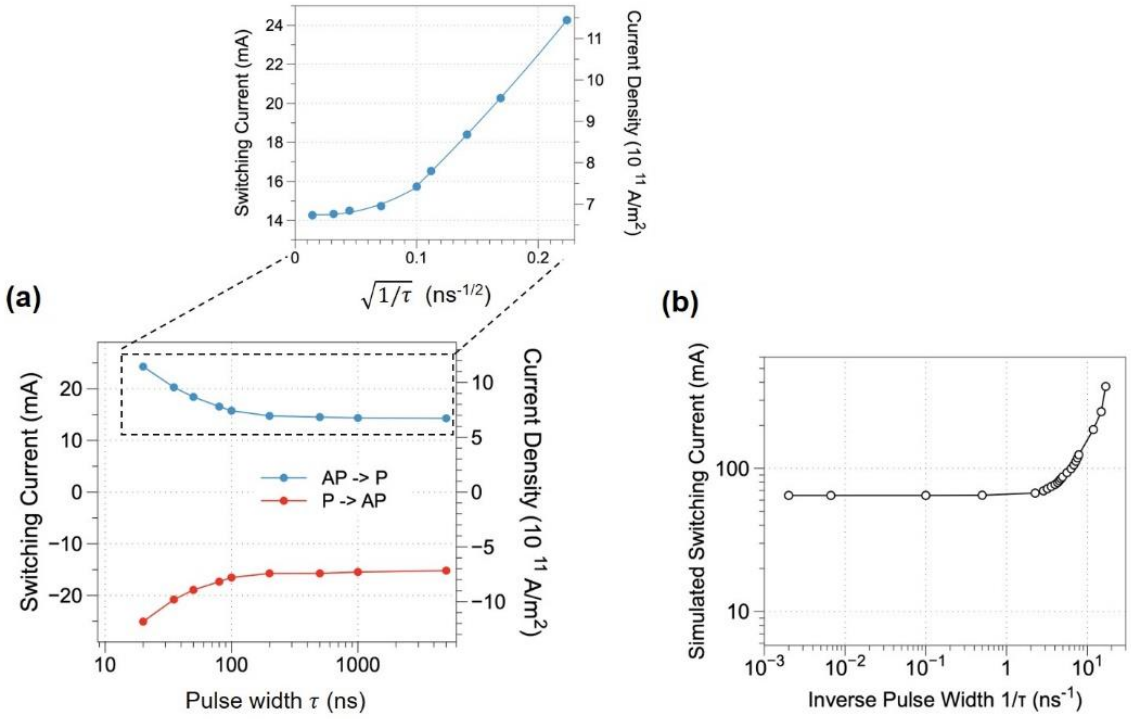

Figure 5.19 (a) Switching current with different pulse width τ. Upper: Switching current is plotted as a function of inverse $\sqrt{\tau}$. (b) Simulated switching current as a function of the inverse pulse width.

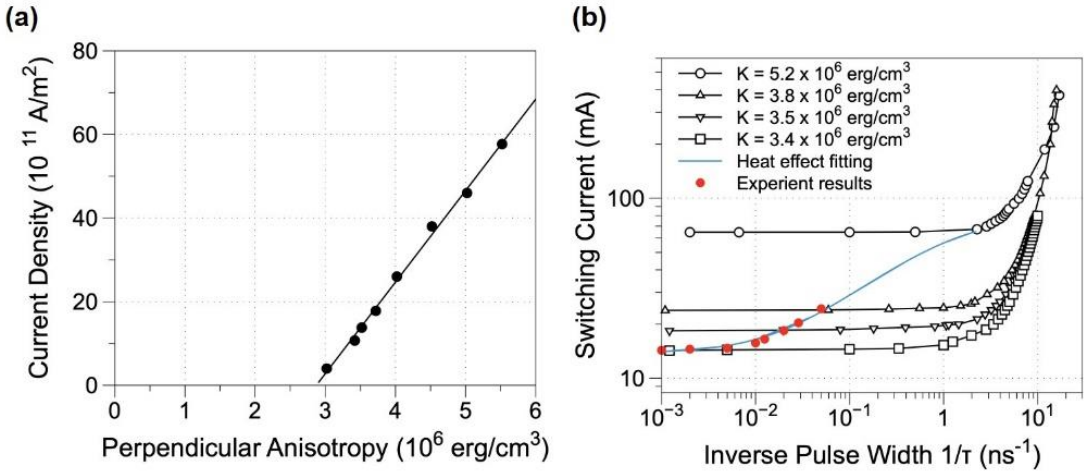

Figure 5.20 (a) Simulated critical current density as a function of the PMA of the free layer. (b) Simulated switching current as function of the pulse width with different perpendicular anisotropy of the free layer (black curves). The blue curve fits the level-off current of each black curve and shows how the switching current changes when considering the heat effect. The red dots correspond to the experimental data.

5.3 Summary

In conclusion, we have demonstrated reliable and repeatable field-free SOT switching of perpendicular MTJs, facilitated by a thin Ir layer which performs dual-function of injection of pure spin current via spin Hall effect and providing an in-plane field via exchange coupling. The switching dynamics has been investigated by both experiments and micromagnetic simulation. We found that the non-thermal impact SOT switching occurs over sub-nanosecond range since it is governed by magnetization precession. At nanosecond scale or longer, thermally induced anisotropy field degradation in the free layer of the MTJ becomes significant, resulting in lowering switching threshold current.

Our approach for field-free switching is based on well-understood phenomena and doesn't require special works in order to combine with magnetoresistive stacks. It should be noted that to get clean research results the write path was designed to contain several other layers along with the Ir layer. Those layers inevitably shunt some amounts of writing current into them. But we'd like to point out that only one in-plane layer is needed to insert below Ir in order to make our concept work. In that case, most of the writing current flows into the Ir layer because of its high conductance, and thus the total amount of current needed will be largely reduced. Moreover, our device exhibit potentials in ultra-fast switching speed and scaling down to dimensions of domain wall width. We believe such Ir-enabled manipulation of perpendicular MTJs can move forward the practical realizations of applications involving SOT memory, sensors and logic devices.

Chapter 6
Field-free Spin-orbit-torque Switching by Device Engineering

In this chapter, we demonstrate another approach in creating a local in-plane field for facilitating the perpendicular spin-orbit torque (SOT) switching. Different from previously utilizing the interlayer exchange coupling characteristic of some specific materials, here we alter the device design to achieve the goal. The idea comes from the well-known phenomenon that a current carrying wire produces an effective magnetic field surrounding it. Based on it, we add a transverse current line to the conventional three-terminal device, which can generate an in-plane Oersted field for the SOT switching. We present the experimental development and characterization of such SOT device. Our results show that the external-field-free deterministic SOT switching of p-MTJs can be achieved in those devices.

6.1 Device design

Our idea for achieving the field-free spin-orbit-torque (SOT) switching via device engineering is partially inspired by the design of the field-driven MRAM. In the field-driven MRAM, writing information is done by using the magnetic field generated by a charge current carrying wire. From Ampere's law, we know that a current carrying wire can create a magnetic field surrounding it. With using this principle, the field-driven MRAM contains two current lines to produce two magnetic fields orthogonal to each other, as shown in Figure 6.1(a). Let's denote the generated magnetic fields as H_1 and H_2. According to the Stoner–Wohlfarth model, the switching of a memory cell occurs when $H_1^{\frac{2}{3}} + H_1^{\frac{2}{3}} \geq H_k^{\frac{2}{3}}$, where H_k is the anisotropy field[102]. One beneficial feature of the field-driven MRAM design is that it prevents unwanted writing of other

cell because individual H_1 or H_2 not exceeding H_k won't results in any switching. One of the major issues in field-driven MRAM, however, is that it only works for in-plane MTJs.

In our case, we aim to have a local in-plane field in our device that's controllable in both magnitude and direction. In resembling the field-generating mechanism in the field-driven MRAM, we design our three-terminal device to have an additional current line orthogonal to the write path, as shown in Figure 6.1(b). We denote this current line as the field path to underlie its function of generating a magnetic field. In this device, the bottom write path is composed of a spin Hall material. Upon applying the charge current into the write path, it generates a pure spin current that diffuses into the adjacent free layer and exert spin orbit torques (SOTs). Meanwhile, a charge current flows into the top field path, which creates an in-plane Oersted field acting on the free layer. Our goal is that the SOTs together with the in-plane Oersted field can deterministically select the magnetization state of the free layer that will be detected by the resistance of the p-MTJ.

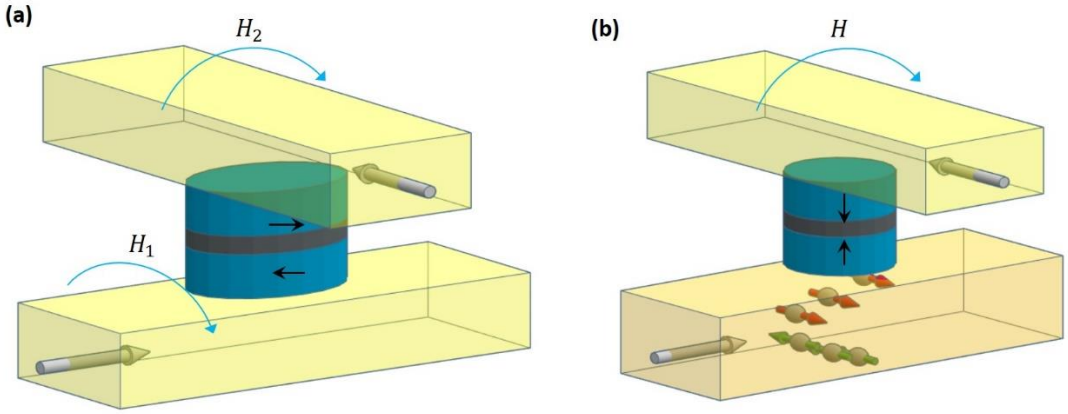

Figure 6.1 (a) Schematic of the field-driven MRAM where two orthogonal current-generated magnetic fields are used to switch to in-plane MTJ. (b) The design of our field-free-switching device where the bottom line is a spin-current source and the top line is responsible for generating an Oersted field.

6.2 Results and discussions

The film stack for this study consists of substrate/ W(4.5)/ FeCoB(1.2)/ MgO(1.2)/ FeCoB(1.3)/ Ta(0.5)/ [Co(0.4)/ Pt(1)]$_{3.5}$/ Ru(0.85)/ [Co(1)/ Pt(0.4)]$_{6.5}$/ Pt(7), where the numbers in the parenthesis have the unit in nanometer. W is selected as the spin-current source due to its prominent spin Hall effect. The film is deposited at room temperature by magnetron sputtering where DC sputtering is used for metals and RF sputtering for oxide. Then the film is processed for

post-annealing at 300 ^{0}C for 10 min. During the annealing, a 5 kOe magnetic field is applied normal to the film surface. Figure 6.2 shows the hysteresis loops of the film. Clear perpendicular magnetic anisotropy (PMA) of the MTJ is observed. The symmetric minor loop of the free layer indicates the stray field from reference layer is compensated by the SAF.

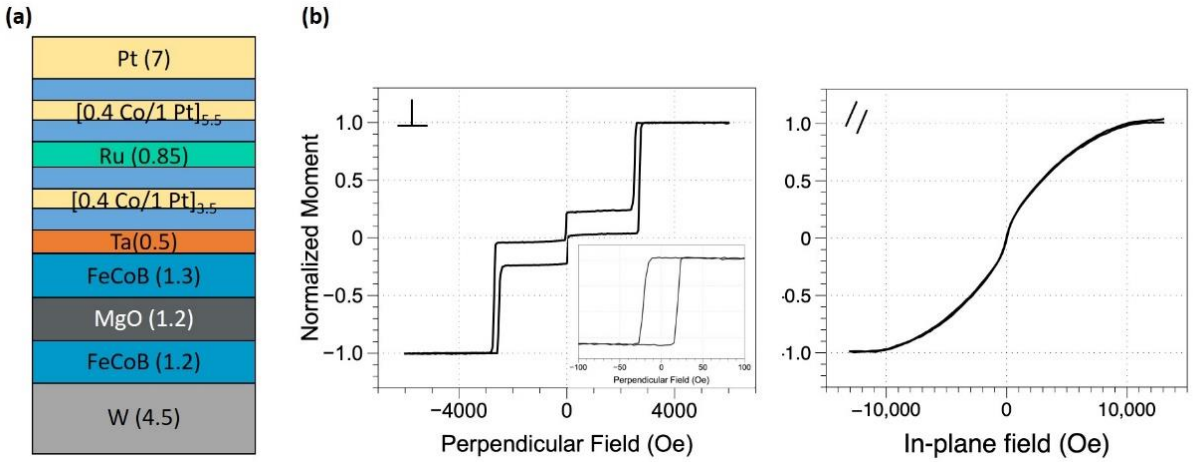

Figure 6.2 (a) Film stack, numbers in nanometer. (b) Hysteresis loops of the annealed film. Inserted in the perpendicular loop: minor loop of the free layer.

The film is then patterned into three-terminal device with the bottom write path and top field path orthogonal to each other, as shown in Figure 6.3(a). The device contains a 150-nm-diameter MTJ in the middle. The width of the write path is 2 μm and the width of the field path is 1.5 μm, both are much wider than the MTJ. Figure 6.3(b) shows the TMR minor loop of the MTJ. Abrupt switching steps are observed in the TMR loop. The TMR of the MTJ is about 50 %.

The SOT switching is first characterized without applying current into the field path during writing. In Figure 6.4, no switching is observed without the presence of an external field. By having a constant external field H_x, the switching start to take place, whose polarity reverses under the fields along opposite directions. The observation suggests the driving force for the magnetization switching derives from the SHE-induced SOTs. Similar switching behaviors were also found and discussed in previous chapters. The critical switching current in our device is about 4.5 mA.

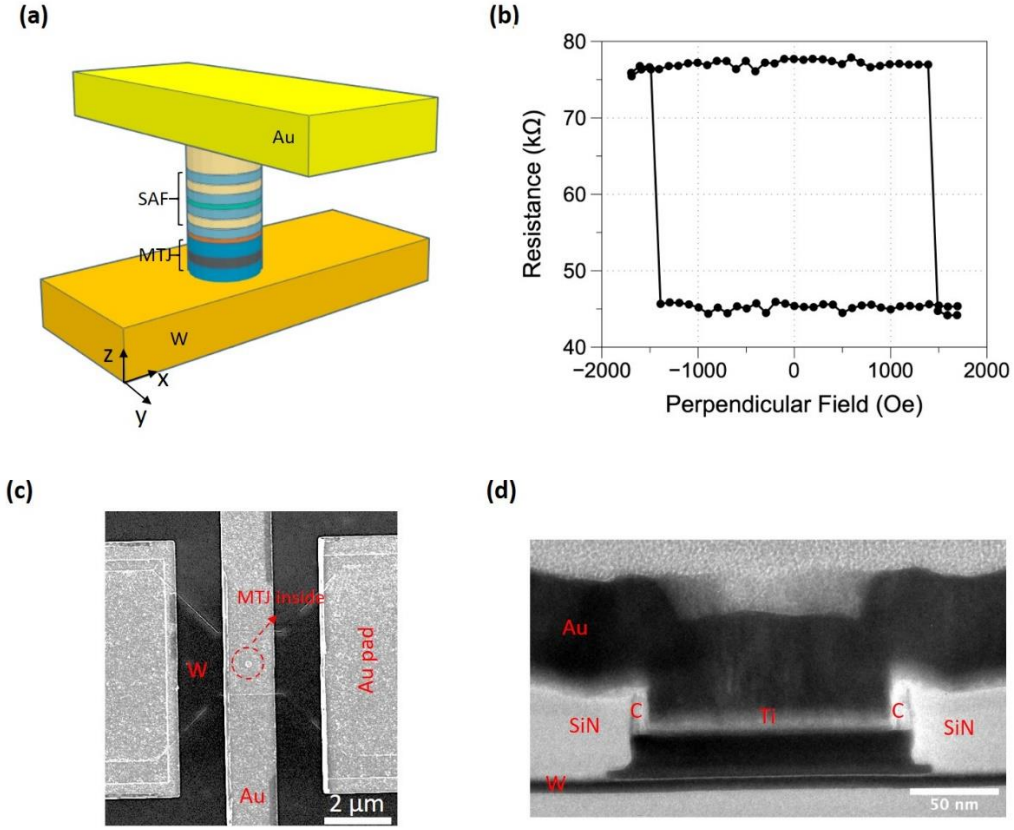

Figure 6.3 (a) Schematic of the device. (b) Field-driven TMR minor loop of the device. (c) Top-view SEM image of the fabricated device. (d) Cross-section TEM image of the MTJ.

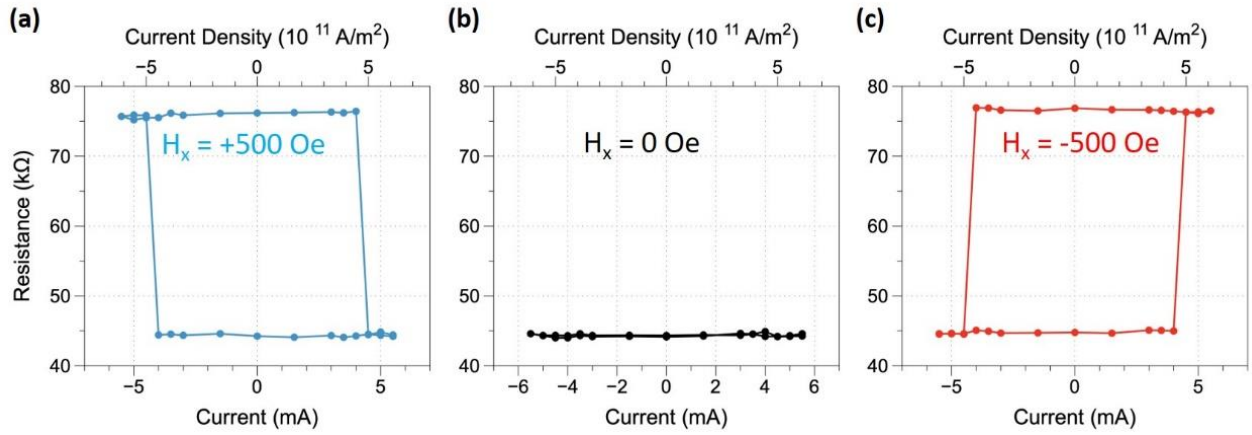

Figure 6.4 Current switching results with an external field of (a) H_x=+500 Oe, (b) H_x=0 Oe, and (c) H_x=-500 Oe. No current is applied into the field path during writing.

Next, we start to apply a charge current into the field path during writing, in absence of an external field. To ensure that the field current and the writing current are applied simultaneously, the testing circuit are designed as shown in Figure 6.5(b). In this testing set-up, the field path is

connected in parallel with the write path. A single current source is used and responsible for sending current pulses into both paths. Two identical resistors are connected in series with the field path, whose resistance can be tuned manually. Note that the direction of the field current should be fixed even when the writing current is applied in the opposite direction. So when the polarity of the writing current is reversed, the connection in the field path will be flipped. Figure 6.5(c) shows the current switching results. Clear evidence of deterministic switching is observed at zero external field. The results indicate that the Oersted field generated by the top wire can effectively assist the SOT switching of the p-MTJ. With knowing the resistance of the top and bottom paths, we can calculate the individual amount of current flowing into each path. The threshold current in the write path for the switching is I_1 = 4.4-4.5 mA that's almost identical as what we obtained in Figure 6.4 while the threshold current in the field path is I_2=36.5 mA.

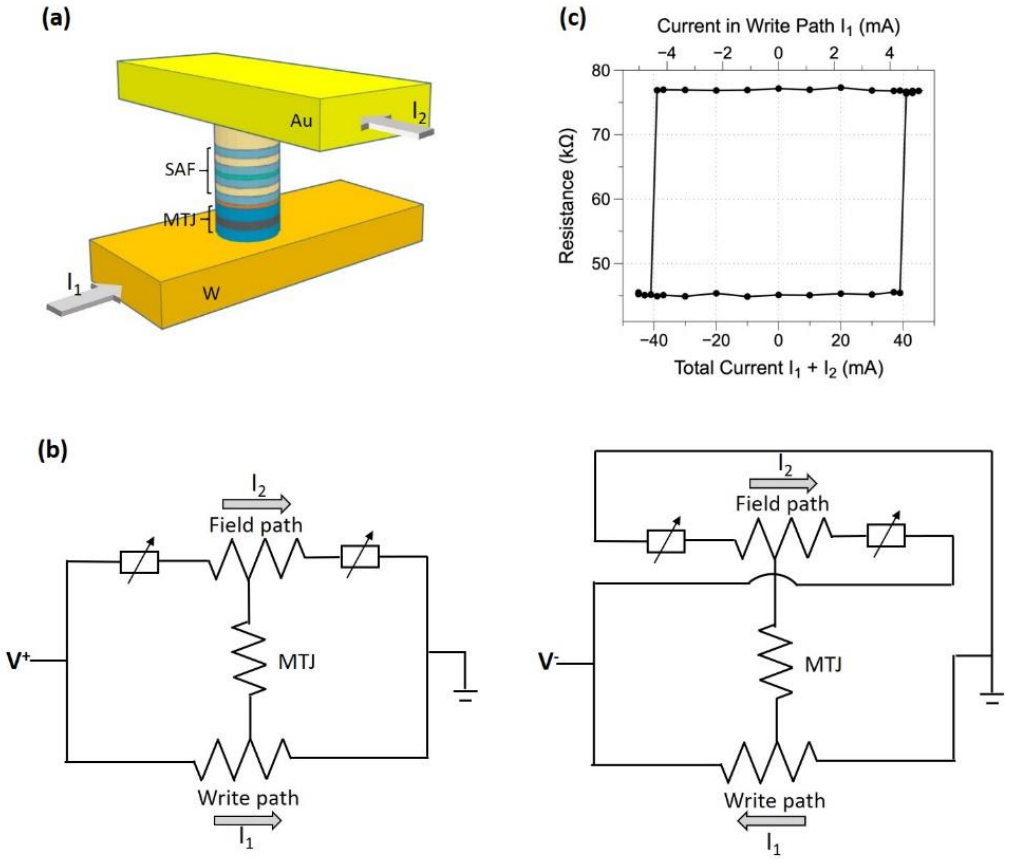

Figure 6.5 (a) Sketch of the device and the current configurations. (b) The testing set-ups with the write current I_1 applied in opposite directions, where the direction of the field current I_2 is fixed. (c) Current switching without an external field. Here, the resistance of the write path and field path is 1750 Ω and 30 Ω, respectively. Each resistor connected with the field path is set as 95 Ω.

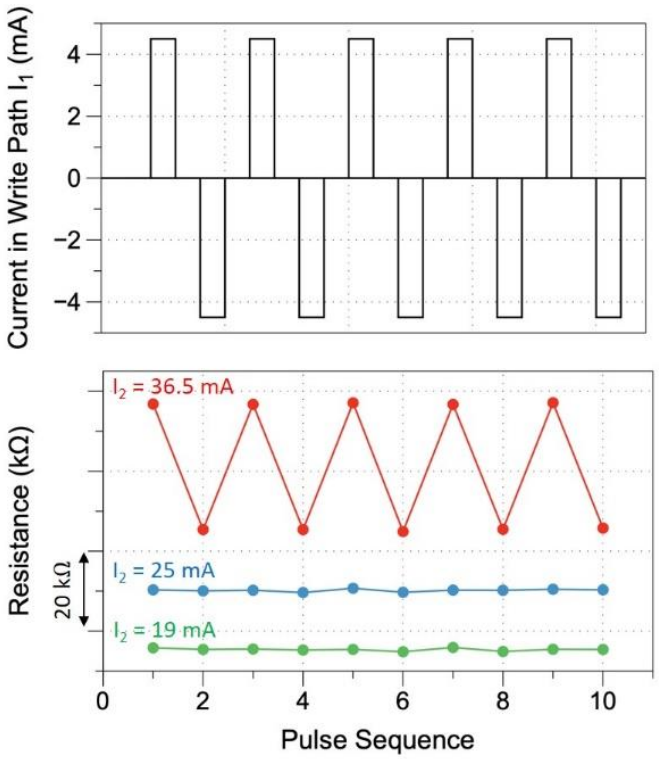

Figure 6.6 The detected MTJ resistance with a sequence of write current I_1=±4.5 mA where the magnitute of the field current is varied.

Given that the write path and field path are connected in parallel, by changing the resistance of the two resistors connected in series with the field path, we can control the relative amount of current that flows into the field path. In Figure 6.6, we apply a sequence of positive and negative switching current ($I_1 = \pm 4.5$ mA) into the write path while the field current I_2 is varied. The repeated switching is obtained only with $I_2 = 36.5$ mA while no significant resistance change of the MTJ is observed with smaller I_2.

To examine the magnitude of the Oersted field generated by the field path, an external field H_x is applied to counter the effect of the Oersted field. The results are shown in Figure 6.7. We start to see some random fluctuations in the switching loop at H_x = +100 Oe. As H_x increases to +150 Oe, the switching loop completely collapses, and no sign of deterministic switching is observed. The collapsing of the switching loop suggests that the Oersted field generated by I_2=36.5 mA in the field path has the magnitude of around 150 Oe. With H_x= +300 Oe, the MTJ experiences a net magnetic field in the opposite direction, and thereby the shape of the switching loop flips.

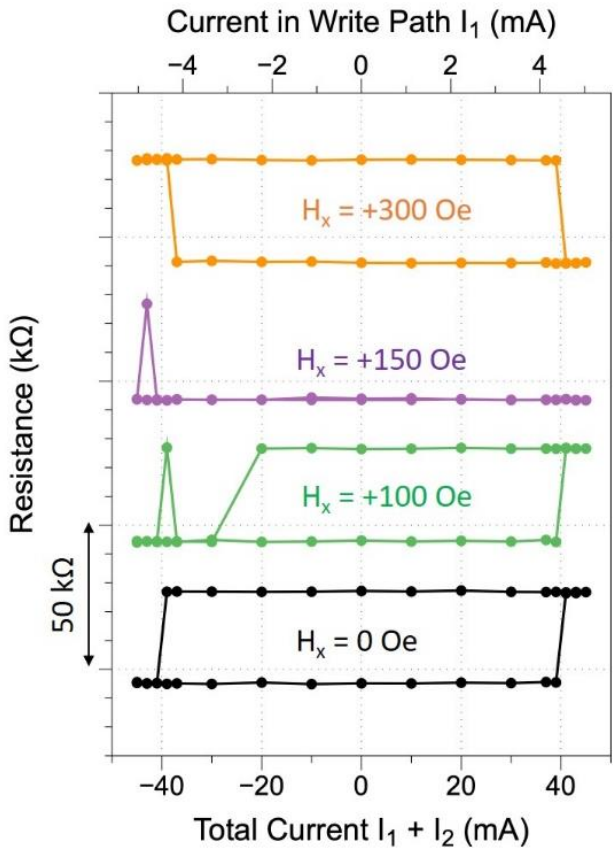

Figure 6.7 Current switching results in the presence of an in-plane field H_x. Different from Figure 6.4, here the current is sent into both the bottom and top paths.

We also simulate the effective magnetic field generated by the field current. Figure 6.8 illustrates the 2-dimensional simulation process. The cross-section area of the field path is meshed into 1 nm × 1 nm grids. The current flowing into each grid is given by $I_{grid} = A_{grid}\frac{I_2}{A}$ where A is the cross-section area of the field path and A_{grid} is the area of the grid. The magnetic field generated by the current in each grid can be calculated by $\boldsymbol{H_{grid}} = 10^4\frac{\mu_0 I_{grid}}{2\pi r}\hat{\phi}$ (Oe), where r is the distance from the grid to the free layer of p-MTJ and $\hat{\phi}$ is the circumferential unit vector. $\boldsymbol{H_{grid}}$ can be decomposed in to x and z components. But by combing the effects from all grids, the z components cancel each other and only x components are left. The total magnetic field acting on the free layer from I_2 = 36.5 mA is calculated to be H = 236 Oe, pointing along x direction. We can see that the the simulated field is comparable to the one obtained experimentally (150 Oe).

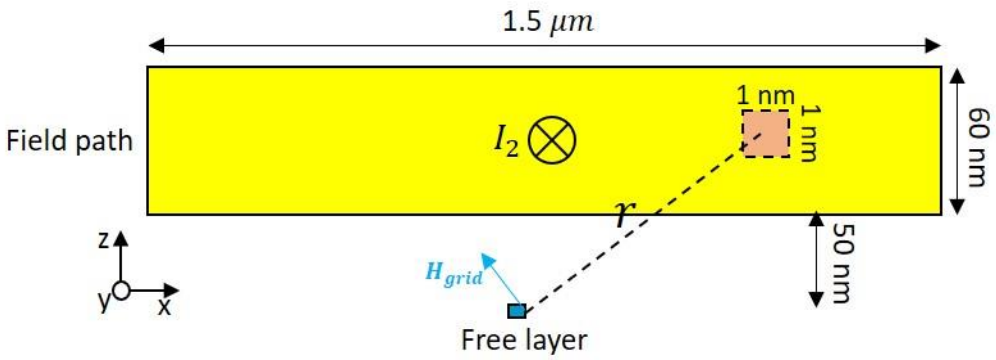

Figure 6.8 Simulation of the Oersted field from the field current. The yellow rectangle is the cross section of the field path that has the dimension 1500 nm × 60 nm. The free layer of the p-MTJ is simplified as a dimensionless point, and it's 50 nm away from the bottom of the field path. The field path is divided into 1 nm × 1 nm grids. The magnetic field $\boldsymbol{H_{grid}}$ from the current flowing in each grid is calculated, and all fields are combined to obtain the total effective field. **Courtesy**: Yuwei Qin.

Our device is found to demonstrate reliable switching capability with sufficient applied write current and field current. The switching diagram is plotted in Figure 6.9, where the blue region implies the combination of I_1 and I_2 that can lead to the deterministic switching of the MTJ. Although increasing the field current gives rise to larger effective magnetic field, it turns out the critical writing current needed for the switching almost doesn't change. For example, the critical writing current I_1^* remains at +4.5 mA with I_2 ranging from +36.5 mA to +44 mA. Similarly, increasing the current value in the write path doesn't have much effect on the critical field current I_2^* either. The simulation results by other research group suggest that a larger in-plane field should result in the reduction in the critical writing current[18]. The discrepancy observed in our experiment may be due to that the range of the applied current is not large enough to cause noticeable change.

From Figure 6.9, we notice that the switching only occurs when both the write current and field current exceed the threshold values, and the MTJ state is determined by the relative orientations of the two current. Such device characteristic renders our device unique advantages. For instance, if a memory array consists of many such device cells, individual I_1 or I_2 will not be able to trigger the switching of any cell. Only when both I_1 and I_2 are above some critical values can the preferable state of a single cell be selected. It prevents the half-select problem where the writing of one cell causes the undesirable writing of other cells. Furthermore, unlike field-driven

MRAM limited to the in-plane MTJs, such memory array can make use of the p-MTJs that have better thermal stability.

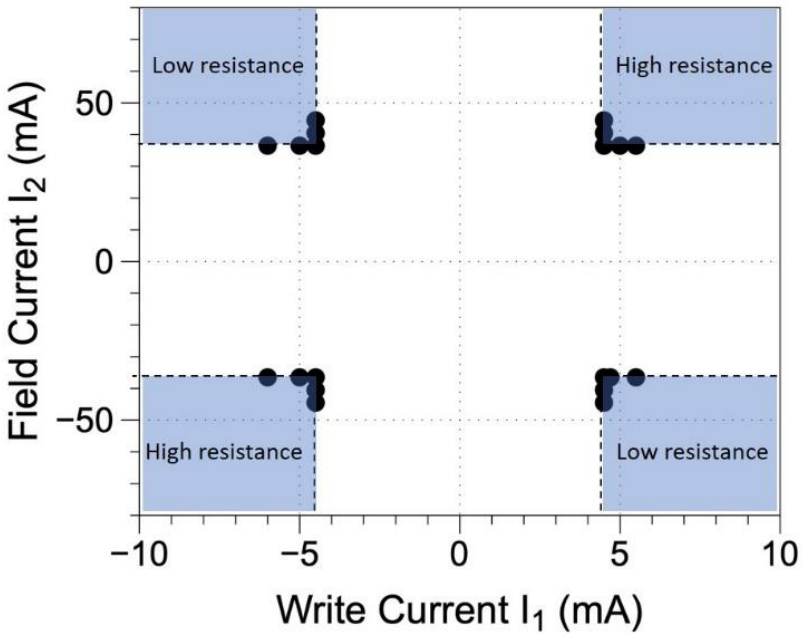

Figure 6.9 The switching diagram with respect to I_1 and I_2, where the blue regions shows the set of currents that can deterministically select the MTJ state. The black circles are the measured critical switching current. The dashed lines are the fits of the trend of the black circles.

6.3 Summary

To summarize, we've realized the field-free SOT switching of p-MTJs via engineering the device design. In particular, we patterned an additional current line orthogonal to the write path. This current line can generate an in-plane Oersted field during the writing operation, assisting the SOTs to switch the free layer of p-MTJ. The MTJ state was found to depend on both the magnitude and relative orientations of the writing current and field current. The critical amount of currents needed for obtaining successful writing results were also evaluated. The SOT device we presented provides reliable write and read operations and doesn't required complicated fabrication techniques, thus can be promising for non-volatile memory and computing applications.

Chapter 7

Tailoring the Current-induced Domain Wall Motion by Engineering the Heavy Metal Underlayers

In the conventional spin-orbit-torque (SOT) driven domain wall motion (DWM) experiments, all domain walls move in the same direction that's either along or against the charge current direction depending on the interplay of the spin Hall effect (SHE) and Dzyaloshinskii-Moriya interaction (DMI). More specifically, the direction of DWM is determined by the chirality of DW and the sign of spin Hall angle of heavy metal (that determines the spin polarization of spin current), reversing either of which leads to reversed direction of DWM. In this chapter, we manipulate the direction of DWM by utilizing two heavy metal underlayers, Pt and W, that have opposite spin Hall angles. This is done by carefully tuning the relative thicknesses of the two heavy metal layers so that the spin polarization of the spin current can be varied. In this way, we are able to control the direction of DWM along or against the flow of charge current without altering the materials in the system. Based on it, we design a DWM-based wedge device where the DWs with the identical chiral structure will travel in opposite directions, and thus leading to expansion or shrinking of reversed domains.

7.1 Study of W structure

The heavy metal materials we choose are Pt and W that have opposite spin Hall angles. Both materials have been widely studied in experiments associated with spin current generation and SOT driven process[18,20,56,103]. It's well known that Pt possess an FCC lattice structure. As for W, however, it has two possible crystal structures: the BCC α-W and the A15 β-W, as illustrated in Figure 7.1(a). Although β-W is a metastable phase, it not only shows higher spin Hall efficiency

(spin Hall angle~0.3[20]) but also have longer spin diffusion length (~3.5 nm[104]) than α-W. The good spin Hall properties make β-W more desirable for our DWM study. Hence, we first investigate the structure of our fabricated W film. Film stacks of substrate/ W (4 nm, 6 nm, 8nm)/ Ta (2 nm) are deposited by DC magnetron sputtering at room temperature. The W layer is deposited by using relatively low DC power (15 W) and high Ar pressure (7 mT), for the reason that the low deposition rate under these conditions favor the growth of β-W[105]. The top Ta layer is used to prevent W oxidation. Next, X-ray diffraction (XRD) measurement is conducted for the lattice structure characterization. Figure 7.1(b) shows the XRD patterns of the films. Note that the 4 nm film is the thinnest film that we can extract XRD signals from. From the XRD results, 4 nm W is found to be formed of mostly β-W, and 6-nm W composes of a mixture of α-W and β-W while 8-nm W is a pure α-W phase. Such thickness dependence has also been observed by other groups[20], where β-W tends to exist in thinner film. As such, thinner W layer, like 0.6–1.5 nm W that will later be used in our DWM study, is also expected to be a β-W phase.

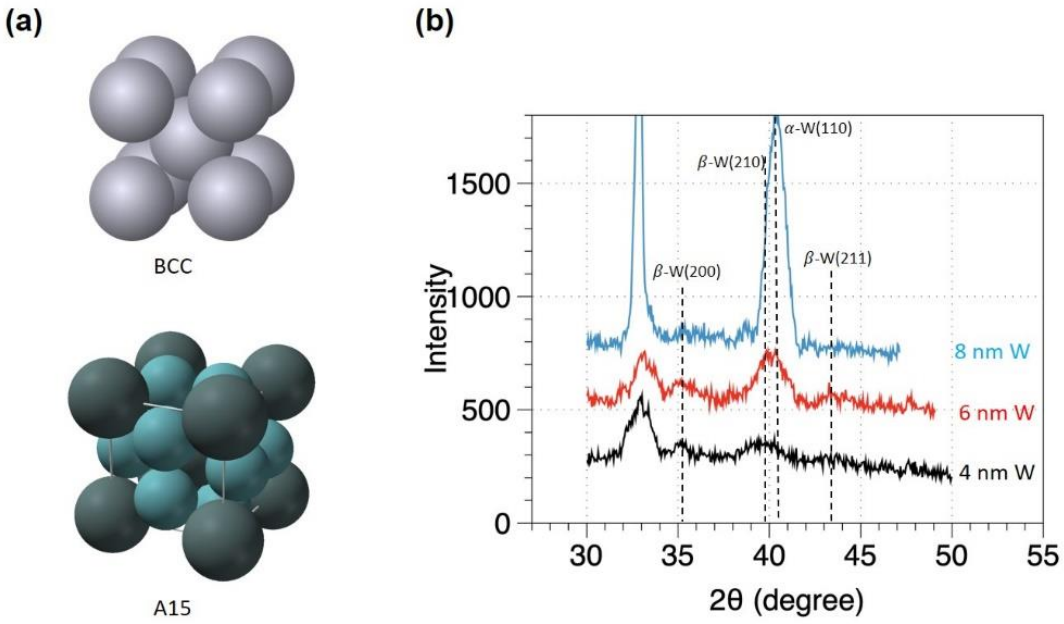

Figure 7.1 (a) Illustration of the (top) BCC and (bottom) A15 structures . Compare with BCC structure, A15 structure has two additional atoms on each face. Note that atoms with different sizes illustrated in the A15 structure are only to distinct their atomic positions. In actual, they should be identical W atoms. (b) XRD measurement results for the films with different W thickness.

7.2 Film stacks and DW chirality

The film stacks for DWM study are substrate/ Ta(0.5)/ Pt(3)/ W(0.6, 0.8, 1, 1.5)/ FeCoB (1.2)/ MgO(2)/Ta(1) with units in nanometers. Note that the bottom and top thin Ta layers are for film adhesion and capping purposes, and the effect of spin Hall torques from these layers on the FeCoB layer should be negligible. The films are then annealed at 305 ^{0}C under 5 kOe magnetic field perpendicular to the film surface. Magnetization curves were measured by Alternating Gradient Field Magnetometer. Figure 7.2 shows the M-H curves that indicate all films have a perpendicular easy axis. It can also be seen that film-level magnetic properties are similar for the films with different W thicknesses.

Next, we characterize the DW chirality via measuring the asymmetric growth of magnetic bubble domains. Figure 7.3(a) illustrate the measurement set-up. The film is placed under the Kerr microscope, subject to a perpendicular field and an in-plane field. An initial bubble domain is created by applying a perpendicular field pulse at a manufactured defect that has lower domain nucleation energy. The growth of the bubble domain is then recorded under a constant perpendicular field in the presence of an in-plane field of various magnitudes. Figure 7.3(b) shows some examples of the observed bubble domains. When only the perpendicular magnetic field is applied, the bubble domain grows symmetrically because there is no energy preference in growing along a particular direction in the film plane. With adding an in-plane field, the bubble domain exhibits asymmetrical growth. More specifically, it can be seen that under H_x = +400 Oe the right DW grows faster than the left DW while the trend reverses if we switch the in-plane field direction (Figure 7.3(b), left and right). Such asymmetric growth is the results of the interaction between the in-plane field and DW chiral structure, where higher DW velocity is favored when H_x is parallel to the center DW magnetization. Our observations suggest that the DWs in our films are right-handed Neel-type walls. A summary of DW velocity as a function of in-plane field is plotted in Figure 7.3(c). We observe that the velocity of anti-aligned DW decreases with increasing H_x and then reaches a minimum. This minimum indicates that the effective DMI field H_{DMI}, which stabilizes the Neel-type wall structure, is cancelled by H_x in both magnitude and direction. Thus, it implies that H_{DMI} is around 430 Oe at the W/ FeCoB interface. Antiparallel H_x larger than 430 Oe overcomes H_{DMI} and flip the DW magnetization, which results in increasing domain wall velocity.

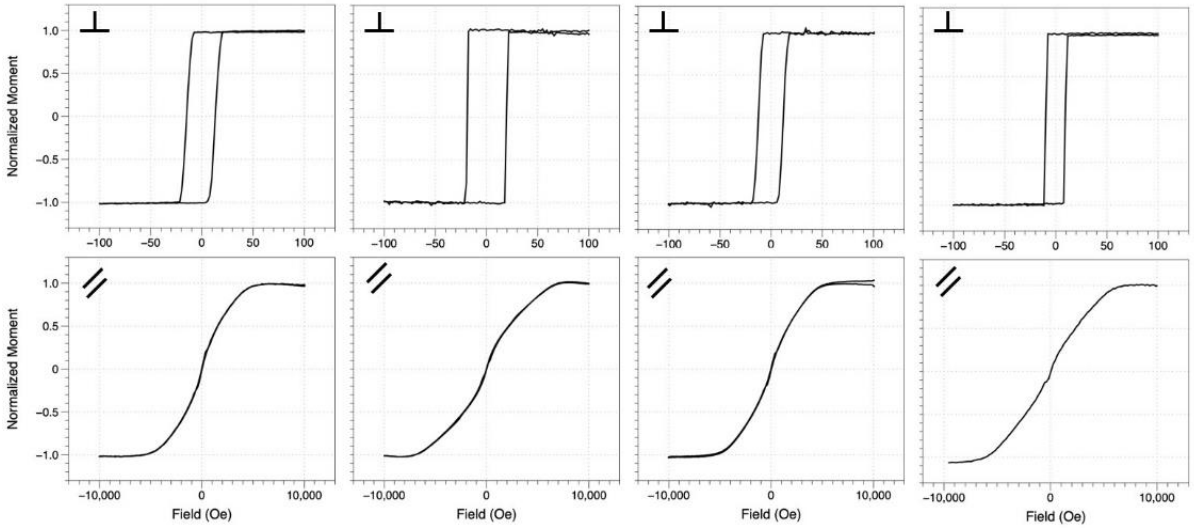

Figure 7.2 Perpendicular and in-plane M-H curves for the stacks with, from left to right, 0.6 nm, 0.8 nm, 1 nm and 1.5 nm W layer.

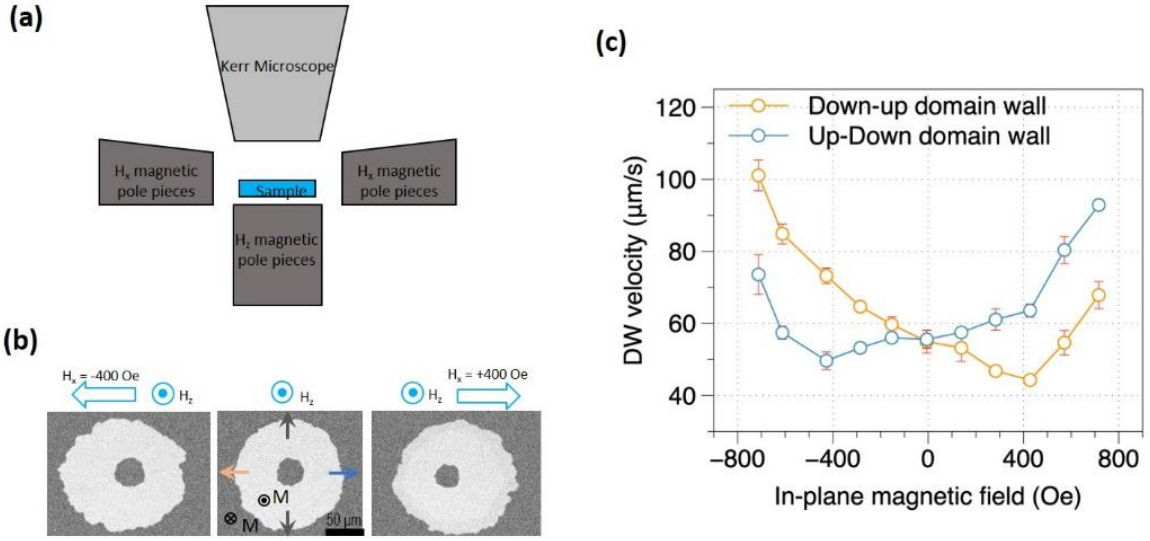

Figure 7.3 Results of the magnetic bubble domain testing obtained from the film with 1 nm W. (a) Schematic of the testing set-up. (b) Examples of the Kerr microscope image showing the shape of bubble domains after applying pulses of perpendicular field H_z = 50 Oe, with and without a static in plane field $H_x = \pm 400$ Oe, Dark circular region in the middle of each image is the size of the bubble domain initially created. Arrows on the domain walls indicate right-handed chirality. (c) Velocity of down-up and up-down domain wall as a function of in-plane magnetic field.

7.3 Current-induced DWM

Now that we've obtained the information about DW chirality, we continue to study the current-induced DWM with different W layer thickness. The films are lithographically patterned into 4 μm wide × 26 μm long wires with bowtie-like contact pads on each side. The DWM under nanosecond current pulses was tracked by Kerr microscope, where the velocity of DWM was determined with the sequences of Kerr images. Figure 7.4(a) show the DWM process for devices with 0.6 nm and 1 nm W layer. In these images, each of the narrow white bands presents a domain with magnetic moment pointing outwards while the rest of the wire has moment pointing in the opposite direction. It can be seen that, for the device with 0.6 nm W layer, domain walls move against the current direction. When W layer thickness is increased to 1 nm, however, domain walls are observed to travel along the current direction. Figure 7.4(b) presents the DW velocity as a function of W layer thickness, where positive velocity refers to the motion along the current direction. We can see that the DW velocity increases linearly with W layer thickness and it changes sign at 0.8 nm W layer. In other words, we obtain DW moving in opposite directions with below and above 0.8 nm W layer.

We attribute our observations to the generation of spin currents with opposite signs of spin polarization as the W layer thickness is changed. Such spin currents further cause the reversed spin orbit torques exerted on the DWs within the FeCoB layer, which results in DWs moving along opposite directions. For convenience, we refer the spin current generated by Pt as positive spin current and the one by W layer as negative spin current. When the W layer is relatively thin (< 0.8 nm), most electric current goes into the Pt layer and so the positive spin current generated by the Pt layer dominates over the negative one generated by the W layer. Hence, in total the FeCoB layer receives a positive spin current (Figure 7.4(a) left). Because the DWs has right-handed chirality, such spin current drives these DWs against the current direction, which is opposite to the case of Pt/ [Co/Ni] (positive spin current + left-handed chirality) and W/ FeCoB/ MgO (negative spin current + right-handed chirality)[57]. As the thickness of W layer increases, more electric current shunts into the W layer that gives rise to larger negative spin current. Eventually, as the W layer is thicker than 0.8nm, this negative spin current overcomes the positive one from the Pt layer (Figure 7.4(a) right). As a result, a net negative spin current is injected into the FeCoB layer and thus DWs experiences opposite spin orbit torques from previous case. Since the domain wall

chirality is fixed, the current driven DWM switches direction to that along the current direction. Note that the spin diffusion length in W is 3.5 nm[104] that is much larger than the W layer thickness in our experiments. Therefore, the spin current from the Pt layer should be able to travel through the W layer and further be absorbed by the FeCoB layer.

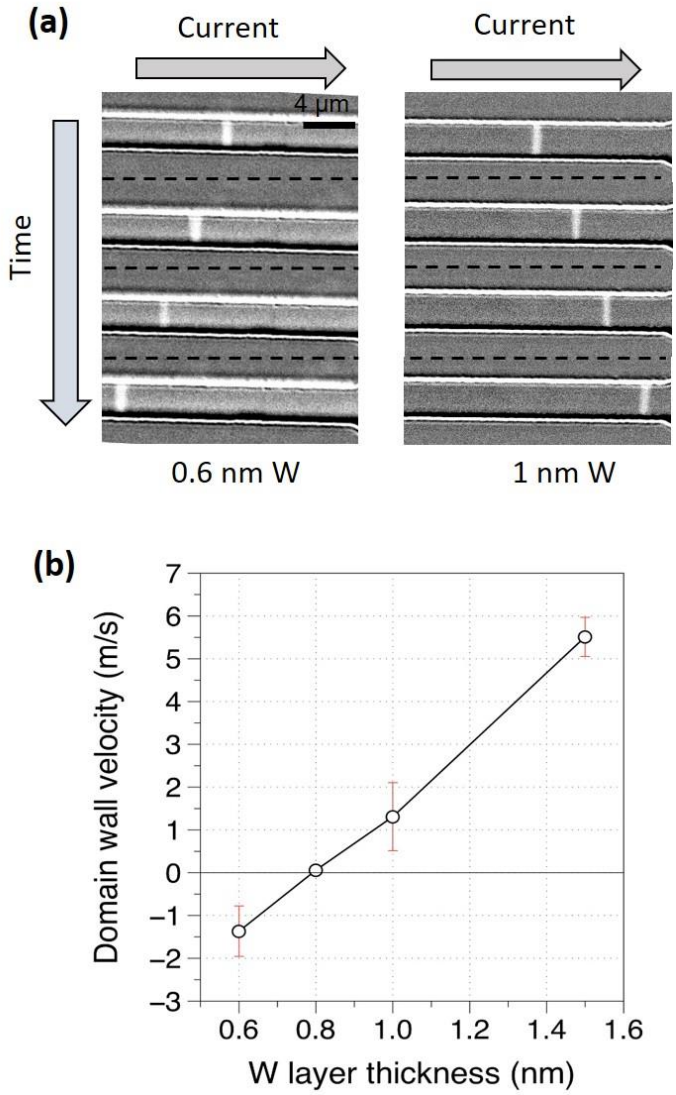

Figure 7.4 Current induced domain wall motion for devices with different W layer thicknesses. (a) Kerr microscope images showing the domain wall motion under applied voltage 0.75 V/μm for devices with 0.6 nm and 1 nm W layer. Between images: 20 pulses with 200 ns pulse length. (b) Summary of the domain wall velocity as a function of the W layer thickness.

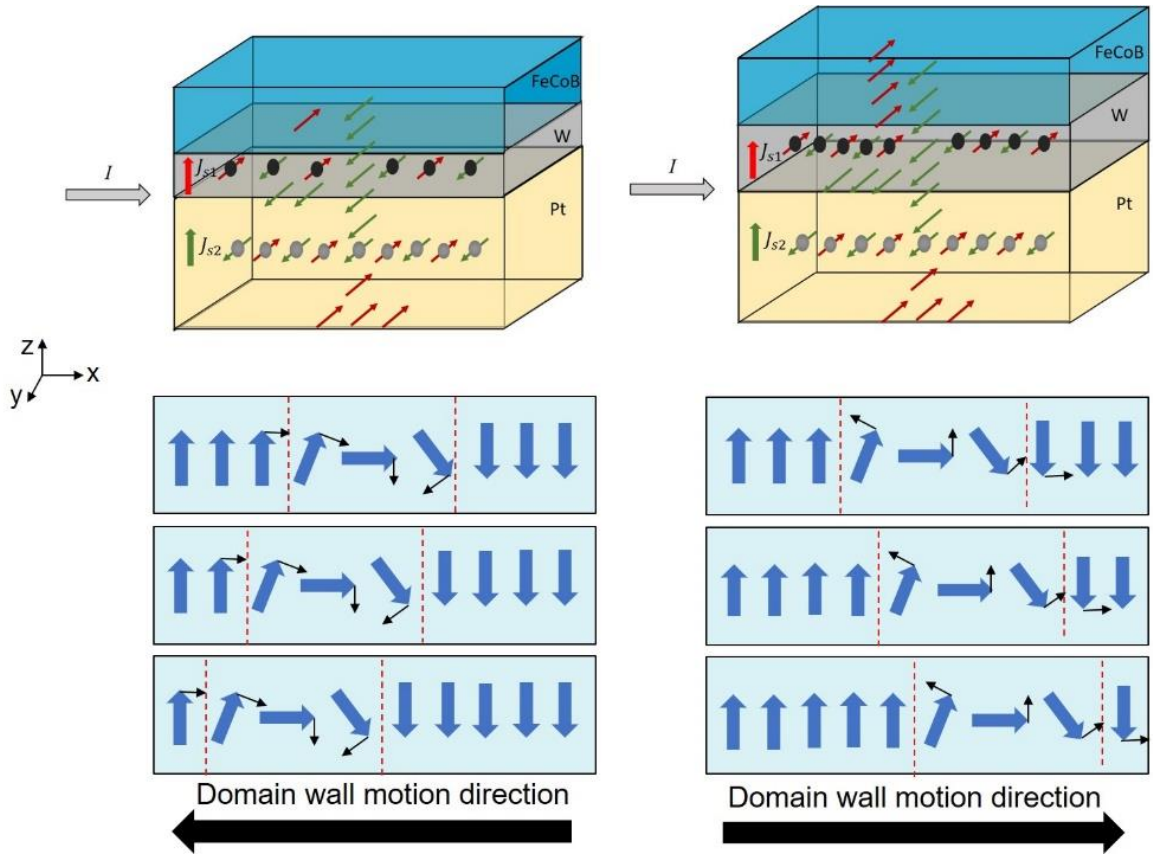

Figure 7.5 Top row: Illustration of injection of the spin currents with opposite signs of spin polarization generated by the two heavy metal layers. Left: W layer < 0.8 nm, Right: W layer > 0.8 nm. Thin red and blue arrows denote the spin directions. Bottom row: Illustration of the SOT DWM in the perpendicularly magnetized FeCoB layer. Blue arrows: magnetization direction. Thin black arrows: damping-like fields from the SOTs exerted on DW magnetization

7.4 SHE-induced magnetization switching

In order to verify that opposite spin currents are generated in our bi-underlayer system, films with 0.6 nm and 1.5 nm W layer are patterned into Hall bars with 2 μm-wide channels for SHE-induced magnetization switching. Current at mA level sweeps from negative to positive values and then anomalous Hall voltage is measured with 100 μA current. A static in-plane field is applied parallel or antiparallel to the current direction and the corresponding magnetization switching curves are recorded. Figure 7.6 shows the results for devices with 0.6 nm and 1.5 nm W layer. It can be seen that for both devices the magnetization switching can be realized by current, and the switching behaviors are opposite if reversing the direction of in-plane field, which is the typical behavior of SHE induced switching. More importantly, we observed that the switching loops are flipped for the two devices under the same in-plane field. For instance, with H_x = 500 Oe and sweeping current from negative to positive, the device with 1.5 nm W layer switches from up to down state while the other device with 0.6 nm W switches from down to up state. It indicates that the spin orbit torques exerted on the FeCoB layer are opposite for the two devices, thus they favor opposite magnetization states under a given set of current and in-plane field. This is clear evidence that the spin currents with opposite signs of spin polarization are generated in the two cases. Meanwhile, we also notice that the device with 1.5 nm W layer has lower switching current threshold. It should be due to that the absolute strength of spin orbit torques in this device are large than the other one. This can also be seen from Figure 7.4(b) that the absolute value of DW velocity with 1.5 nm W layer is higher than that with 0.6 nm W layer.

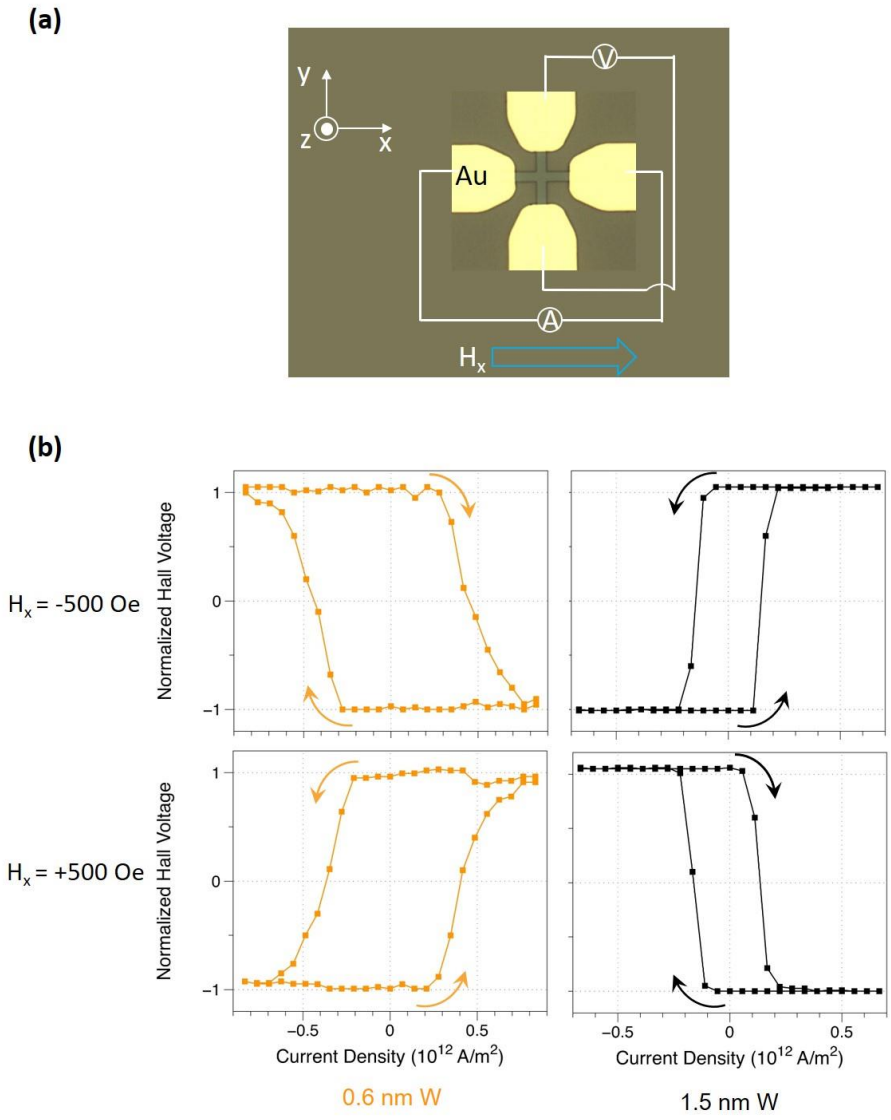

Figure 7.6 (a) Optical image of the device (middle) and schematic of measurement settings. (b) Current-induced switching loops for devices with 0.6nm and 1.5 nm W layer. Top row: in-plane field applied along -x direction and bottom row: field along +x direction.

7.5 Proposed device

We have shown that the direction of DWM can be controlled by varying the W thickness in the double underlayer device. Based on our results, we propose a wedge device that can achieve field-free perpendicular SOT switching. The wedge device is similar to the previous double-underlayer device, but now the W layer has a wedge structure with the thickness in the middle to be 0.8 nm, as shown in Figure 7.7. Upon injecting a charge current into the device, due to thickness variation, the left part of the device will generate a positive spin current while the right part will create a negative spin current. This wedge device also contains a transverse current path (not shown) so that an opposite domain can be nucleated by a current-generated oersted field. For the device to work, a reserved domain is first initialized at center of the device by passing a short pulse through the transverse current line. Then a write current is applied along the horizontal direction in the heavy metal underlayers. The write current triggers SHE of the heavy metal layers and further induce DWM in the FeCoB layer. Now the left and right DWs have the same chiral structure but they receive spin current of opposite spin polarization. Hence, the SOTs drive the left and right DWs to move in the opposite directions. From our previous results, the left DW should move along the current direction as the W thickness below it is greater than 0.8 nm, while the DW on the right side should move against the current direction. As such, depending on the polarity of the write current we can obtain the expansion or shrinking of the opposite domain, and thus deterministically select the magnetic state of the perpendicular FeCoB layer. Note that it's done in the absence of an external field. The device without a wedge layer (Figure 7.4(a)), in the contrary, can only give domain shifting because the left and right DWs move in the same direction. In that case, DWM can't lead to the magnetization reversal.

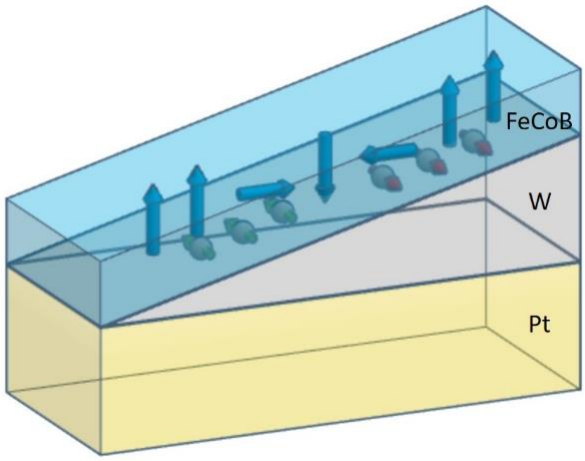

Figure 7.7 Proposed DW device that contains a W wedge. Due to the W thickness variation, the spin currents in the left and right parts of the device have opposite spin polarizations.

7.6 Summary

In summary, we have studied the current-induced DWM in a system with two heavy metal underlayers that are of opposite spin Hall angles. We demonstrated that by changing the relative thickness of two heavy metal underlayers it's able to obtain current driven DWM along opposite directions. This results from the competition of two pure spin currents with opposite signs of spin polarization that are generated by the spin Hall effect of the heavy metal underlayers. Such way of manipulating current-induced DWM also allows us to design a novel device that utilizes a wedge structure to realize the field-free perpendicular SOT switching.

Chapter 8

Spin-orbit Torque Driven Domain Wall Motion with a Magnetic Oxide Interlayer for mCell Application

mCell, proposed by our group, is a domain wall motion (DWM) based four-terminal magnetoresistive device with isolated write path and read path for all-spin logic and memory applications. A mCell requires an electric-insulating magnetic layer to couple the spin-Hall write path to the magnetic free layer in the read path. Both paths are magnetic layers with perpendicular magnetic anisotropy (PMA) and their perpendicularly oriented magnetization needs to be maintained with an insertion layer. Here we report the development of a magnetic oxide (FeO_x) layer that could serve as the electric-insulating magnetic layer (EIM) inserted in between the write and read paths of the mCell. The FeO_x insertion layer not only provides sufficient magnetic coupling between the adjacent magnetic layers, but also significantly enhances the spin-orbit torque (SOT) driven DWM of the coupled stacks. Measurements also show the FeO_x layer is relatively resistive and should provide adequate electric insulation between the write and read paths.

8.1 mCell introduction

As shown in Figure 8.1, a mCell is a four-terminal resistor with the isolated write path and read path. The write path consists of a spin hall layer and an adjacent magnetic layer with a trapped domain wall (DW) while the read path contains two perpendicular MTJs (p-MTJs), each of which has a top reference layer and a bottom free layer. In mCell, the write path is magnetically coupled but electrically insulating with the read path via an electric-insulating magnetic (EIM) interlayer. In this way, the resistance state of the MTJ in the read path can be controlled by the magnetic state

of the write path via magnetic coupling while there is no interference between the writing and reading current. During device operation, a charge current is sent into the spin hall layer in the write path to move the DW. Due to the magnetic coupling through the EIM layer, the free layer in the read path aligns with domain magnetization underneath it in the write path. The change in the moment direction of free layer will read out by resistance change of the MTJ. Reversing current direction in the write path also reverses the direction of DWM, and thus the two resistance states of the MTJ can be obtained.

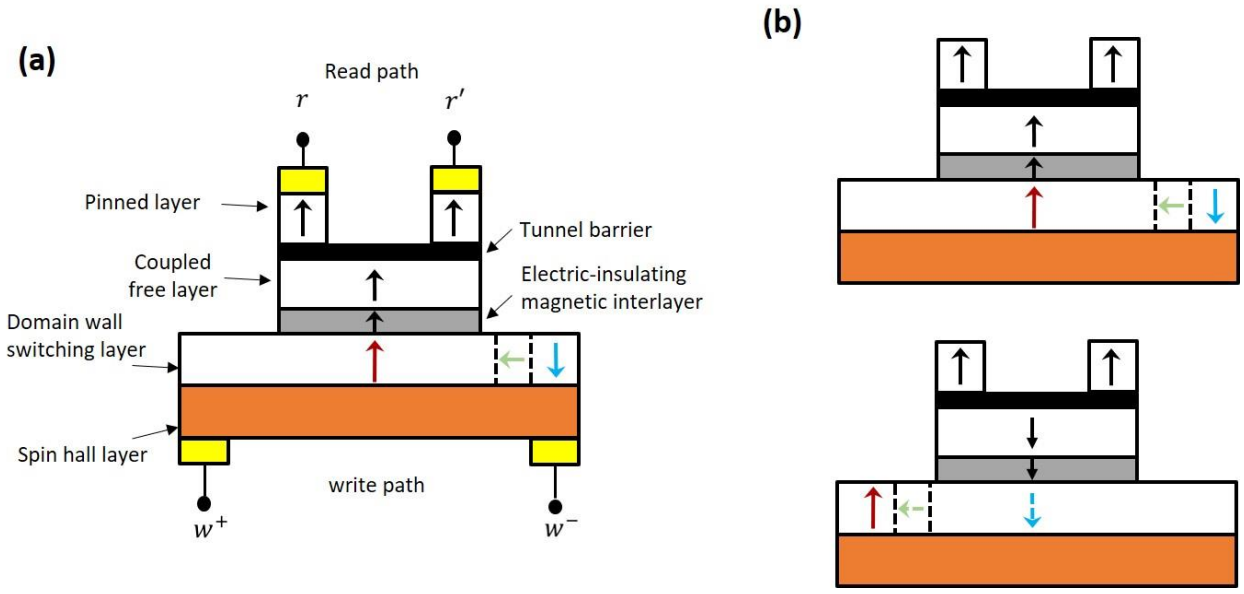

Figure 8.1 (a) The design of the mCell. (b) Low and high resistance states of a mCell, which is controlled by the SOT-driven DWM.

8.1.1 Materials selection for mCell

Because the write path and read path are separate in the mCell, they can be developed and optimized individually. The read path can adopt the common MTJ stacks described in Chapter 5, which consists of the FeCoB/ MgO/ FeCoB trilayers with a top [Co/Pt] based synthetic antiferromagnet (SAF) structure. As for the write path, we'd like to select the materials that can enable the efficient SOT-driven DWM. For this reason, we choose to use the Pt/[Co/Ni] multilayer stack because such material combination not only has prominent spin Hall effect (SHE) but also has strong Dzyaloshinskii-Moriya interaction (DMI), ideal for high-speed and low-power DWM[55,67]. Lastly, we propose to use FeO_x for the EIM layer that should provide both magnetic coupling as well as electrical insulation. In the following sections, we focus on the current-induced

DWM in the mCell. We study the magnetic and electrical properties of the FeO_x layer, as well as compare the current-induced DWM with and without this magnetic oxide layer.

8.2 DWM in Pt/[Co/Ni] wire

We first study the current-induced DWM in the write path only, which consists of the Pt/[Co/Ni] multilayers. Film stack of substrate/ TaN(0.5)/ Pt(3)/ [Co(0.3)/ Ni(0.6)]x2/ Co[0.3]/ TaN (2) (unit in nm) is deposited by magnetron sputtering at room temperature. Figure 8.2(a) shows the well-fined PMA of the film, which should originate from Pt/Co and Co/Ni interfaces[106]. Next, the film is patterned into $2\mu m$-wide domain wall wires for the DWM testing. The fabrication and testing procedure of the DW device are described in Chapter 3. Figure 8.2(b) shows the Kerr microscope images of the wire after applying a series of current pulses. The DWs move along the direction of current flow. It implies the driving force for the DWM is SHE instead of spin transfer torque (STT) because STT always moves DWs in the direction of electron flow. Figure 8.2(c) summarizes the DW velocity as a function of the current density applied along the wire. The DWM only occurs with the current density higher than some critical value J_c. Above J_c, the DW velocity increases sharply with the applied current. The DMI of the Pt/[Co/Ni] wire is evaluated from the current-induced DWM at current density $J = 1 \times 10^{12}\ A/m^2$ by applying an external in-plane magnetic field H_x along the wire. When the external field balances the effective DMI field, the DWs will stop moving. Figure 8.2(d) shows the DW velocity in the presence of a static in-plane magnetic field. No motion is observed in a finite range of field. We select the middle point of this range as the effective DMI field that gives H_{DMI} = 1.35 kOe. The results in Figure 8.2(b)-(c) demonstrate that we are able to get reliable DWM in Pt/[Co/Ni] wires, where the direction and velocity of the motion can be controlled by the sign and magnitude of the applied current.

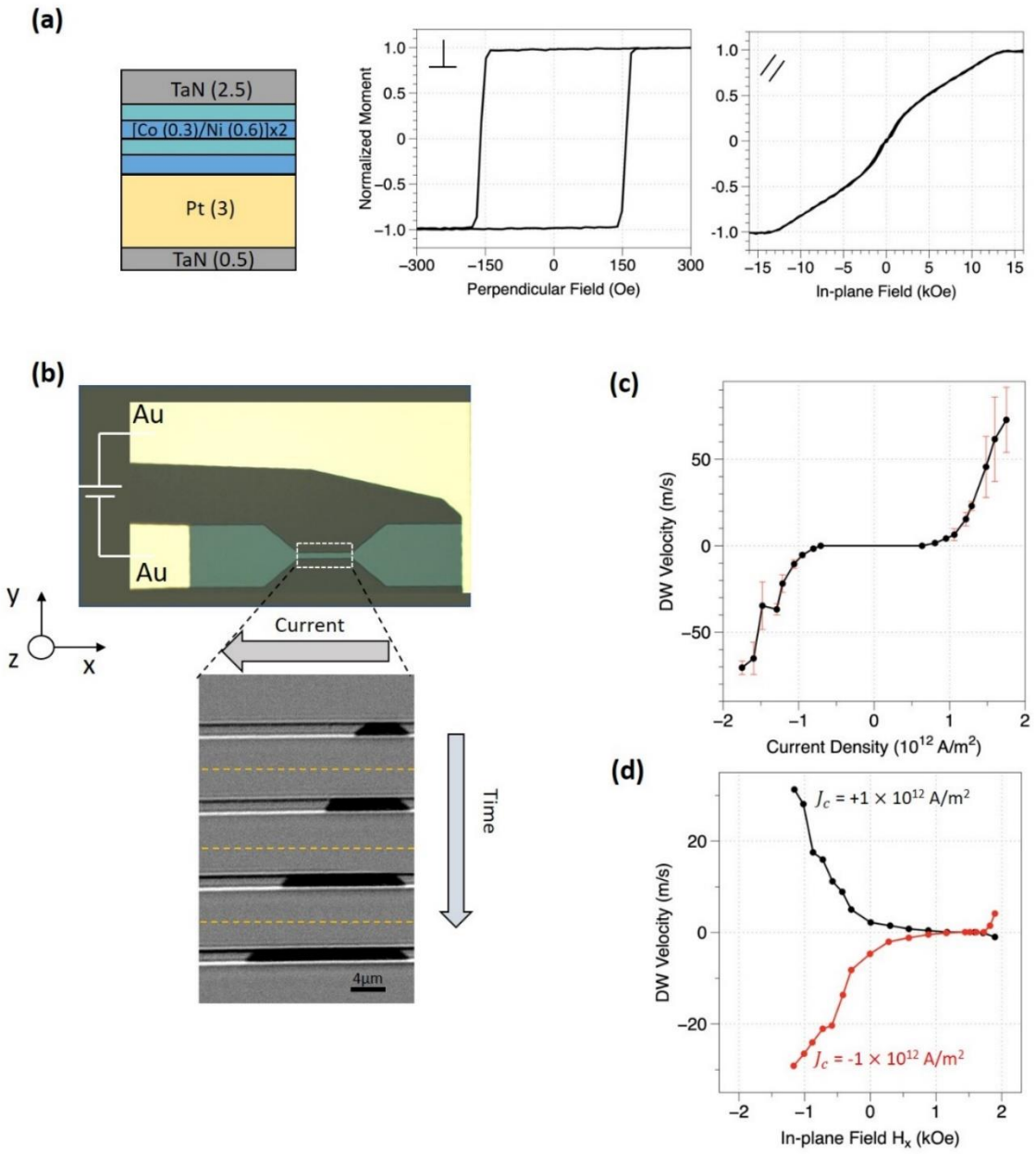

Figure 8.2 (a) Film stack and hysteresis loops of the film. (b) Top: optical image of the DW device and the sketch of the testing set-up. Bottom: DWM images captured by the Kerr microscope. J_c = 1.5 × 10^{12} A/m^2, 1 pulse between images. (c) DW velocity as the function of current density in Pt. (d) Velocity of the up-down DW as a function of the in-plane magnetic field H_x, under J_c = ±1 × 10^{12} A/m^2.

8.2.1 Annealing effect on current-induced DWM

The MTJ units in the mCell requires post-annealing for promoting the PMA as well as the TMR property. The post annealing is often processed at the temperature ranging from 250 ^{0}C to 400 ^{0}C for a period of time up to several hours. Such annealing can cause some changes in the DWM behavior in the Pt/[Co/Ni] wire. Hence, we'd like to investigate the annealing effect on current-induced DWM in Pt/[Co/Ni] wires. For this study, the Pt/[Co/Ni] films are annealed at different temperatures from 250 ^{0}C to 350 ^{0}C for 10 min. Then all films are patterned into the DW devices. Both film and device properties are measured and compared. From Figure 8.3, it's observed that the H_k drops significantly above 300 ^{0}C. Meanwhile, the DMI in Pt/[Co/Ni] wires is also found to decrease shapely after annealing. To explore the cause for such decrease, we conduct the scanning transmission electron microscopy (STEM)-energy dispersive X-ray spectroscopy (EDS) mapping of of Pt, Co, Ni, and Ta in our films, as shown in Figure 8.4. With comparing the images of the films before and after annealing, we observe prominent interdiffusion across the Pt/Co interface. Such interlayer diffusion occurring during the annealing results in the less sharp interface, causing the reduction of H_k and H_{DMI}.

An example of the annealing effect on the DWM is shown in Figure 8.3(c). Compared to the DWM with the un-annealed film, the device with the annealed films exhibit reduced DWM efficiency. The annealing not only causes larger critical current density but also results in slower motion speed. Figure 8.3(d) shows the DW velocity measured at $J = 1 \times 10^{12}\ A/m^2$ as a function of different annealing temperatures. Increasing the annealing temperature yields a monotonic decrease in the DW velocity, except for the case with the annealing temperature above 350 ^{0}C. Because larger H_{DMI} can cause faster DWM, the decreasing trend of the DW velocity can be explained by the decreasing H_{DMI} after annealing. The reason for the increase in DW velocity above 350 ^{0}C is still unclear and needs further investigation.

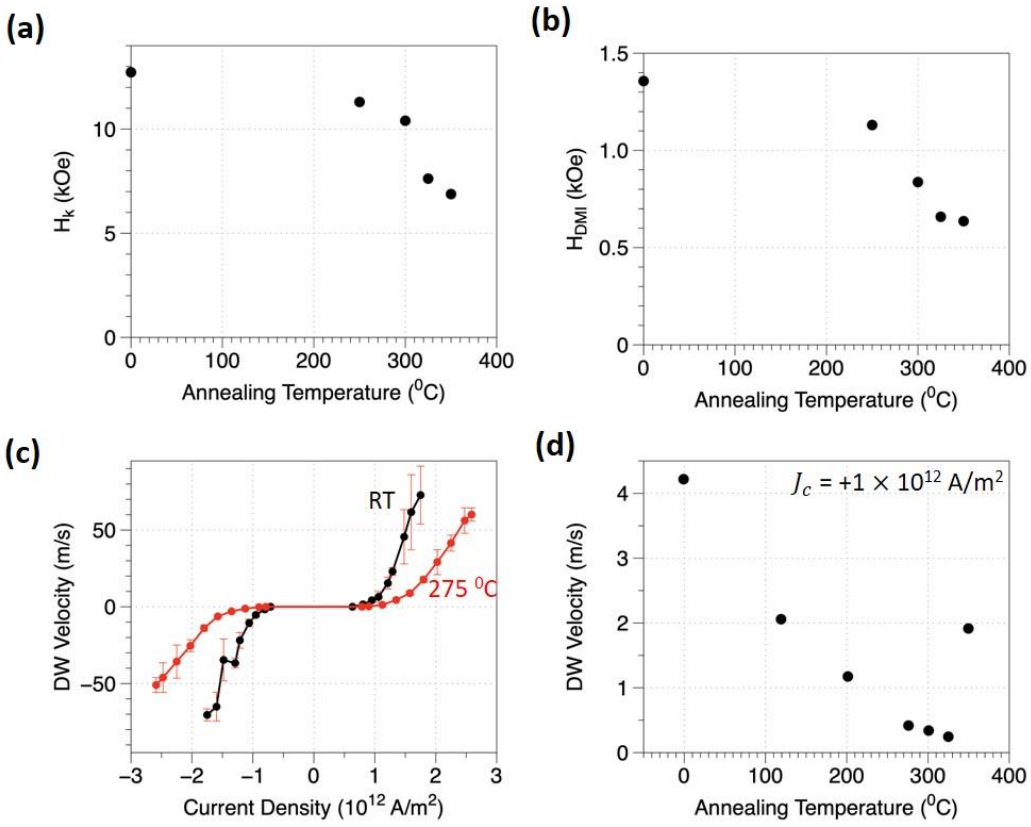

Figure 8.3 The effect of annealing on (a) the anisotropy field, (b) the effective DMI field, (c) and (d) DW velocity.

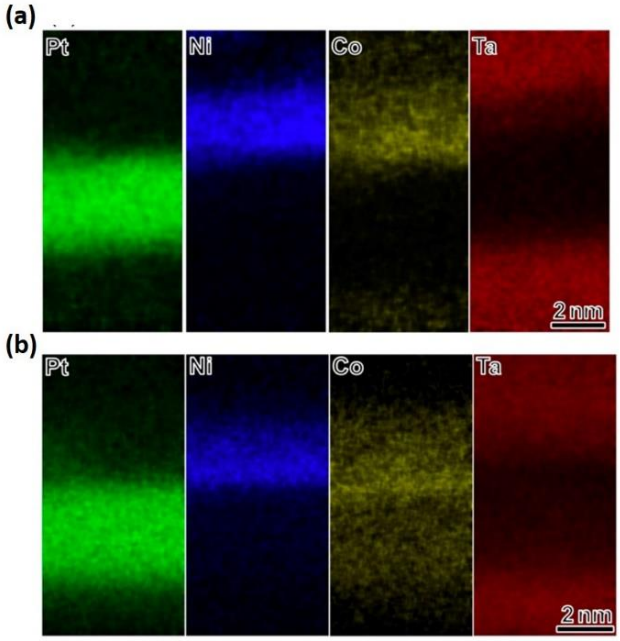

Figure 8.4 EDS mapping of Pt, Ni, Co and Ta in the films (a) before annealing and (b) after annealing at 300 ^{0}C.

8.3 DWM in magnetic bilayers coupled by a magnetic oxide interlayer

We've demonstrated the DWM in the Pt/[Co/Ni] write path and explored the effect of annealing on the DWM efficiency. In the mCell design, it requires an EIM interlayer to couple the write path with the free layer in the read path so that the magnetization state of the free layer can be controlled by the DWM in the write path. This interlayer should also be electrically insulating in order to minimize the intermixing of writing and reading current. Here we demonstrate a magnetic oxide interlayer, FeOx, that can both provide magnetic coupling and some electric resistance between two perpendicular magnetic components.

8.3.1 Magnetic property

All films are deposited by magnetron sputtering (DC for metals and RF for oxides) at base pressure $< 2 \times 10^{-8}$ Torr on thermally oxidized Si substrate. To study the magnetic oxide layer, the film stacks are, from substrate side, Ta (2)/ Pt (3)/ [Co (0.3)/Ni (0.6)]x2/ FeO_x (0.8 or 1.2)/ $Fe_{52.5}Co_{17.5}B_{30}$ (1.2)/ MgO (1)/ Ta (2) (unit in nm). We denote those films as the bilayer stacks because they contain two magnetic components (the [Co/Ni] multilayers and FeCoB/MgO layers). Note that the FeO_x ($1.3< x <1.5$) layer is the intended magnetic oxide layer. For comparison, two other stacks are fabricated with only one magnetic component, which are Ta (2)/ Pt (3)/ [Co (0.3)/Ni (0.6)] x2 /Ta (2) (denoted as the Co/Ni stack) and Ta (2)/ FeCoB (1.2)/ MgO (1)/ Ta (2) (denoted as the FeCoB stack). As-deposited films are subsequently annealed at 275 ^{0}C under 5000 Oe magnetic field perpendicular to the film surface. Perpendicular and in-plane magnetization curves are measured by alternating gradient field magnetometer (AGFM) and saturation magnetization is measured by physical property measurement system (PPMS).

The perpendicular and in-plane hysteresis curves are shown in Figure 8.5 for the bilayer stacks with 1.2 nm and 0.8 nm FeO_x insertion layer. For the stack with 1.2 nm FeO_x layer, there is a sharp switching step in the perpendicular curve followed by a large tail (Figure 8.5(a), blue curve). It has been widely studied, however, that the Pt/ [Co/ Ni]x2 multilayers and the FeCoB/ MgO layers both have square-shaped perpendicular loop due to their strong perpendicular interfacial anisotropy[89,106], which are also seen in our previous measurement results (Figure 8.2). Hence, the large tail should result from the in-plane shape anisotropy of the 1.2 nm FeO_x insertion layer, as the in-plane moment from the FeO_x layer pulls at least one of its neighboring magnetic layers

towards the in-plane direction. This is also supported by the soft magnetic behavior around zero field in the in-plane curve (Figure 8.5(b), blue curve). When the FeO_x layer thickness is reduced to 0.8 nm (Figure 8.5, red curves), the perpendicular loop has a squared shape with sharp switching and in-plane curve shows typical hard axis behavior. These changes indicate the entire stack has perpendicular anisotropy with negligible in-plane component. We attribute it to that the strong perpendicular magnetic moments from the Pt/ [Co/ Ni]x2 multilayers and the FeCoB/ MgO layers are now able to align the moment of the FeO_x layer into perpendicular direction when the moment of the latter is relatively small. It can be seen the insertion of the FeO_x layer results in lower anisotropy field of H_k= 5 kOe, compared to 11.3 kOe of the Co/Ni stack and 8.1 kOe of the FeCoB stack (Table 8.1). Note that the single-step switching in the perpendicular curve for t_{FeO_x}= 0.8 nm suggests that the entire magnetic film stack is ferromagnetically coupled together. The coupling indicates that the aligned FeO_x insertion layer in turn act as an exchange coupling interlayer for its neighboring magnetic components.

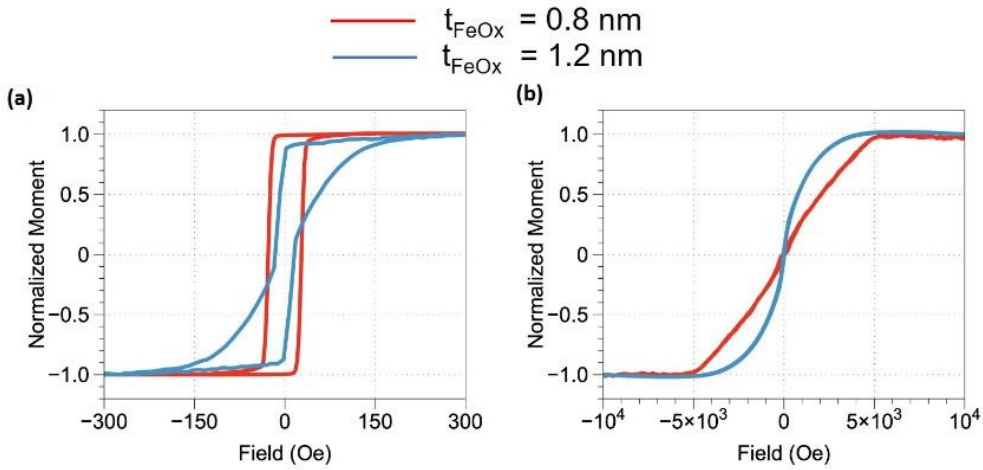

Figure 8.5 Normalized (a) perpendicular and (b) in-plane magnetization versus applied field curves for the bilayer stacks with 0.8 nm (red) and 1.2 nm (blue) FeOx insertion layer.

Table 8.1 The Anisotropy field (H_k), coercivity (H_c) and saturation magnetization (M_s) of the bilayer stack with 0.8 nm FeO_x insertion layer, the Co/Ni stack and the FeCoB stack.

	Bilayer stack	Co/Ni stack	FeCoB stack
H_k (kOe)	5	11.3	8.1
H_c (Oe)	28	155	30
M_S (emu/cc)	-	575	584

8.3.2 Tunneling resistance of the magnetic oxide

To characterize the resistance of the FeOx layer, films are deposited with stacks Ta (25)/ Pt (3)/ [Co (0.3)/Ni (0.6)]x2/ FeOx (3 or 5) or Ta (5)/ FeCoB (1.2)/ Ta (2) /Pt (10) with unit in nanometers. Note that the MgO layer is excluded to avoid its insulating impact on the resistance measurement. These films are patterned into 3.5 μm-diameter circular devices with pairwise top and bottom leads by photolithography, argon ion mill etching and reactive ion etching. Device resistance is measured by two-probe resistance measurement technique with current flowing through the device stack from the top lead to the bottom lead. Figure 8.6(a) gives the schematic of our circular devices for resistance measurement while the measured device resistance is plotted in Figure 8.6(b) for different insertion layers. Results show that the devices have three orders of magnitude higher resistance with 5 nm FeO_x insertion layer than those having the Ta insertion layer of same thickness. It should be noted that, for devices with the Ta insertion layer, the main contribution to the device resistance comes from the Ta bottom leads instead of from the device stack. When the FeO_x insertion layer thickness decreases to 3 nm, the device resistance drops dramatically, which might imply electron tunneling behavior through the insertion layer[107]. When the thickness is reduced below 1 nm, resistance from the device stack becomes too small compared to the Ta bottom leads, and thus hard to be characterized. So more conductive materials such as Pt or Cu, need to be used for bottom leads in the future experiments in order to better characterize the resistance of ultra-thin FeO_x. With that being mentioned, the experiments we conducted convey some information that the FeO_x interlayer is much more resistive than a normal metal interlayer.

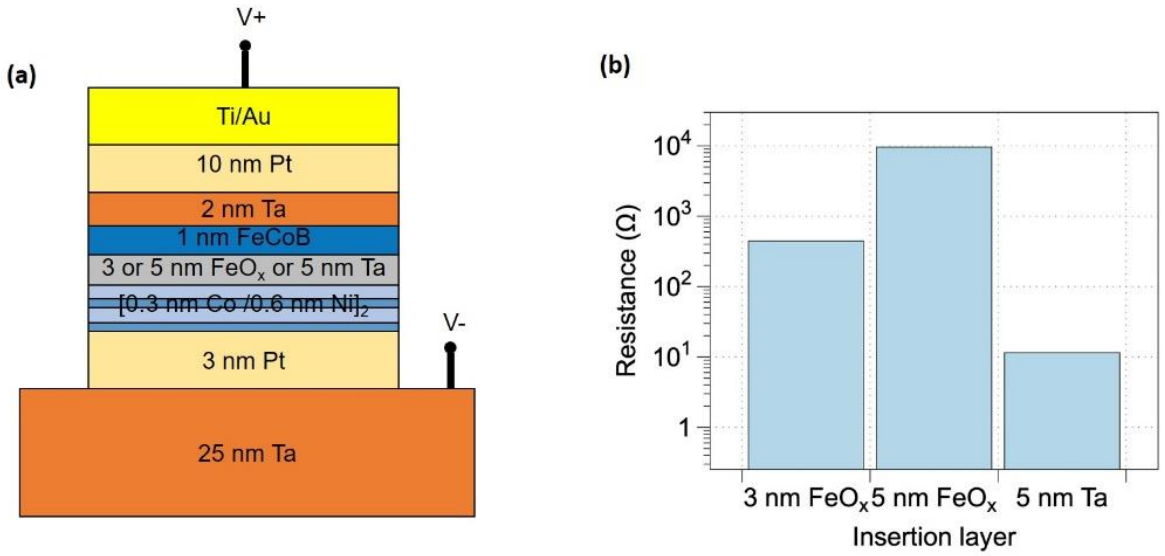

Figure 8.6 (a) Schematic of the 3.5 μm-diameter circular device for resistance measurement. (b) Device resistance for stacks with 3 nm, 5 nm FeO_x insertion layer or 5 nm Ta insertion layer.

8.3.3 Current-induced domain wall motion with the magnetic oxide interlayer

To study the current-induced DWM, films of the bilayer stack with 0.8 nm FeO_x insertion layer and the Co/Ni stack are lithographically patterned into 2 μm-wide 26 μm-long wires with bowtie-like contact pads on each side. Figure 8.7(a) shows the DWM process for the bilayer stack with 0.8 nm FeO_x interlayer. Note that there is only one DW created within the wire. It can be seen that, the DW moves in the current direction, which agrees with the previously shown DWM in the Pt/ [Co/Ni] multilayers (Figure 8.2(b)). Meanwhile, magnetic contrast in up- and down- domains is uniform and no splitting in domains was observed during DMW. The stable and uniform DWM suggests that DWM in FeCoB layer is consistent with that in the Pt/ [Co/Ni] multilayers. In other words, the spin Hall driven DWM in the Pt/ [Co/Ni] multilayers induces the even-pace DWM in the FeCoB layers due to the complete ferromagnetic coupling via the FeO_x interlayer.

The corresponding DWM velocity is plotted in Figure 8.7(b) as a function of applied voltage per unit wire length. The DWM velocity increases sharply with larger applied voltage and the highest velocity we achieved was 58 m/s at 0.9V/μm. The velocity curve for the Co/Ni stack is also included for comparison (Figure 8.7(b), orange curve). Our results show that the DWM in the coupled bilayer stack has even higher velocity than that in the Co/Ni stack under the same applied voltage (or equivalently, under the same current density, as we assume most of the current shunts

into the Pt layer during measurement). To better understand it, we adopt the one-dimensional (1D) model of domain wall dynamics that takes into account SHE and DMI, as described in [56]. The motion velocity in the center of a Neel type wall is given by $v \propto H_{DMI}\theta_{SHE}J/H_kM_st$, where H_{DMI} is the effective DMI field, θ_{SHE} is the spin Hall angle, J is the current density in the spin Hall layer, M_s is the saturation magnetization and t is the thickness of the ferromagnetic layer. In our case, H_{DMI}, θ_{SHE} and J are the same for both the coupled bilayer stack and the Co/Ni stack. $H_k$of the coupled bilayer stack is less than a half of the H_k of the Co/Ni stack, as shown in Table 8.1. The M_s value of bilayer stack is calculated as the weighted average of the Pt/ [Co/Ni] multilayers and the FeCoB layer, and the small magnetization of the FeO_x layer is ignored for simplification. This gives us the magnetization value M_s = 579 emu/cc for the coupled bilayer stack. Thus, simple calculation yields that the DWM velocity of the coupled bilayer stack should be about 35% larger than that of the Co/Ni stack. Although this value does not agree with our results quantitatively, it suggests that the enhanced velocity observed in the coupled bilayer stack is mainly due to the lower H_k. In addition, the coupled DWM proves to be efficient that has voltage threshold as low as 0.3 V/μm. Such threshold value suggests a mCell of 100 nm size would only need the switching voltage of 30 mV that's suitable for realizing the fanout of mCell-formed logic circuits. We also observed, however, that DWM of the coupled bilayer stack is only stable between – 0.9 V/um and 0.9 V/ μm. When the applied voltage is beyond this range, the DWM became irregular and one domain splits into multi-blocks (Figure 8.7(c)). The most likely reason is that joule heating becomes prominent under large applied voltage. The large amount of heat within the wire not only lowers the H_k of the entire stack but also destabilizes the ferromagnetic coupling.

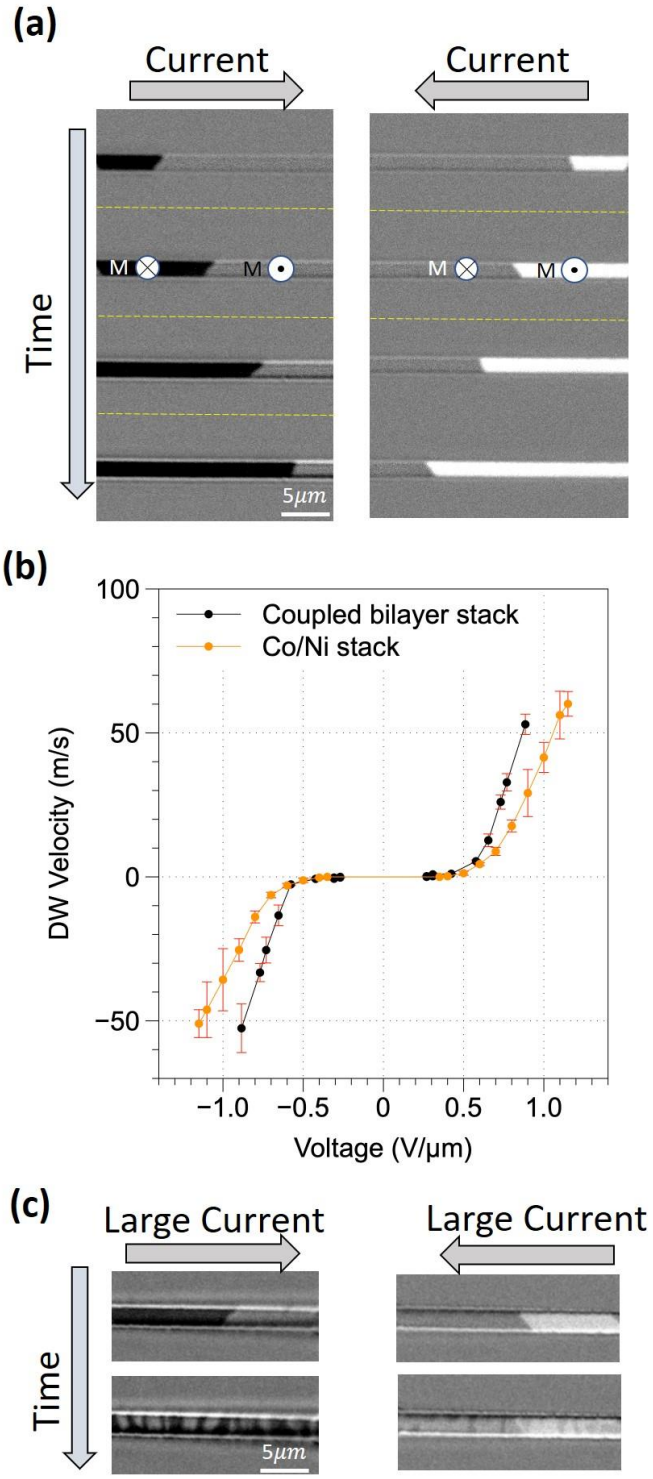

Figure 8.7 (a) Kerr images showing current induced DWM for the bilayer stack with 0.8 nm FeO_x insertion layer under 0.7 V/μm, 100 ns and 2 pulses. (b) Domain wall velocity as a function of voltage per unit wire length for the coupled bilayer stack and the Co/Ni stack. (c) Kerr images showing irregular DWM of the coupled bilayer stack under 1.15 V/μm, 100 ns and 2 pulses.

8.3.4 Discussion

After studying the properties of the FeO_x and its effect on DWM, one question still remains in the actual composition of the fabricated FeO_x, that is, the Fe: O ratio. Although the FeO_x layer is sputtered from a Fe_3O_4 target, the actual composition can differ from the target due to different sputtering yields of Fe and O atoms. It turns out to be difficult to probe the composition of the FeO_x layer by common chemical composition techniques such as energy-dispersive X-ray spectroscopy (EDS), for that (1) EDS is not good at quantifying light element like oxygen and (2) the FeO_x layer can be oxidized when exposed to air during SEM/TEM sample preparation and thus the real composition changes. With that being mentioned, however, we still get some evidence that the as-deposited FeO_x should have very close composition to Fe_3O_4. In one of ongoing projects in our group[108], the FeO_x fabricated with the same conditions is used for grain boundary material for heat assisted magnetic media (HAMR). In their TEM results, it's found that the grain boundary material is crystalline, and the lattice structure and size matches that of Fe_3O_4. This may provide some side information that the composition of our FeO_x is close to Fe_3O_4.

Another concern is that the FeO_x can oxidize the neighboring magnetic layers. As the FeO_x layer gets thicker, this problem is likely to become more severe and destroy the perpendicular anisotropy of neighbor magnetic layers, which can cause what we saw in Figure 8.5, blue curves. Although the oxidation from FeO_x can't be completely ruled out, we think the possibility is low. The reason is that Fe-O bonds are more chemically stable than Co-O and Ni-O bonds as indicated by the Ellingham diagram. So the oxygen atoms should prefer to stay within the FeO_x layer instead of diffusing into the nearby Co/Ni or FeCoB layers. It's somewhat analogous to the case of FeCoB/MgO in MTJ where oxygen is strongly bonded with Mg and is not absorbed by Fe or Co.

8.4 Summary

In summary, we introduced the concept of mCell and discussed the materials selections that fit the mCell's design. We studied and developed the write path structure where the SOT driven DWM is used to control the magnetization. The annealing effect on the DWM was evaluated. It was found the interdiffusion occurring during the annealing results in the degradation of the DWM efficiency. Thus, it would be desirable if one can develop a more thermally stable structure for the DMW in the future work.

In addition, we have showed that a magnetic oxide layer (FeO_x) could act as both a ferromagnetic coupling and an electric barrier between two perpendicular magnetic components. This electrical-insulating magnetic layer enables that the spin Hall driven DWM in one magnetic component induces the even-pace DWM in its coupling layer. Although the in-plane nature of the insertion layer lowers the H_k, the velocity of the coupled DWM turns out to be largely enhanced. The voltage threshold for coupled DWM is as low as 0.3 V/μm, which makes the mCell with a magnetic oxide interlayer a promising candidate for power-efficient logic and memory applications.

Chapter 9
Conclusion and Future Work

Writing magnetic bits by spin-orbit torques (SOTs) arising from spin-orbit effects such as spin Hall effect (SHE) creates new possibilities for ultrafast and low-power memory and computing applications. In this research work, we have studied the role of SOTs in altering the magnetic state and dynamics in the perpendicularly magnetized systems. Several approaches have been explored for manipulating the SOTs to obtain desirable switching outcomes. By engineering the materials and device design, we demonstrated that the SOT switching of a perpendicular layer no longer requires an externally applied magnetic field. We hope the concepts and methods developed in this work would advance the viability of SOT switching as well as inspire the development of new device architectures.

9.1 Summary

One of the major issues we tackled is that the SOT switching of a perpendicular magnet often demands an external in-plane field, which greatly limits the practicality of SOT devices. In our work, we first attempted to eliminate the need for the external field via engineering the SOT materials. We discovered a unique heavy metal material, iridium (Ir), that can not only generate a spin current from SHE but also mediate an intrinsic magnetic field by its interlayer exchange coupling capability. By utilizing these properties, the robust SOT switching of a perpendicular Co layer has been achieved in absence of an external magnetic field. The Kerr microscope study revealed that the switching process in our devices takes place by domain nucleation followed by domain wall propagation to achieve the full expansion of reserved domains. In-depth simulation analysis suggested that the exchange coupling field plays a vital role in the domain expansion, and the higher the coupling field, the higher the expansion speed of the reversed domains.

After testing the concept in the switching of a single perpendicular magnet, we moved on to develop the three-terminal SOT device that combines the Ir switching scheme with perpendicular magnetic tunnel junctions (p-MTJ). It was found that Ir fits pretty well with the MgO-based p-MTJs. A series of dedicated experimental works have been shown to construct the nanoscale three-terminal devices. In those devices, we obtained the reliable and repeatable writing and reading operations at zero external field. In addition, a systematic study has been conducted in order to characterize the switching profiles of the device. We pointed out that the joule heating has significant impact on lowering the magnitude of the critical switching current.

Furthermore, we proposed and tested a new device design to realize the field-free perpendicular SOT switching. The idea was based on the well-known phenomenon that a current carrying wire produces an effective magnetic field. By adding an extra current line orthogonal to the write path in the three-terminal device, it was shown that an in-plane Oersted field can be generated and used for assisting the SOT writing of the p-MTJs. We investigated the critical amount of current needed for producing enough Oersted field for getting the successfully writing. We demonstrated that only when both the writing current and field current are above some critical values can the stable of p-MTJ be selected. Such device characteristic prevents the erroneous switching of half-selected elements.

In our SOT switching experiments, we found that the switching process is often dominated by the opposite domain nucleation and then the motion of the domain walls (DWs) to expand the reversed domains. To gain more understanding of the domain wall motion (DWM) process, we explored the DWM in a perpendicular magnetized system with two heavy metal underlayers. The two underlayers can generate competing spin currents that have opposite spin polarizations. We were able to control the amount of the spin current from each layer by tuning the layer thickness. We reported that varying the relative thicknesses of the underlayers in our DW devices led to the DWM along different directions. Based on our results, we proposed a wedge DW device that utilizes the SOT driven DWM to get the expansion of an opposite domain for the full magnetization reversal.

SOT driven DWM provides efficient and versatile ways to control the magnetic state of a magnetic layer. The last part of our work investigated a DWM based magnetic logic device, known

as mCell, in an attempt to understand how well the device could work. In particular, we focused on the writing operation in mCell. The write path structure based on Pt/[Co/Ni] wires were designed and the DWMs were tested. We discussed the annealing effect on the DWM performance. Moreover, we developed a magnetic oxide interlayer that not only couples the [Co/Ni] multilayers in the write path with the free layer in the read path but also provides some electrical insulation between them. It was found that the efficiency of the DMW can be enhanced due to the insertion of this magnetic oxide interlayer.

9.2 Suggestions for future work

9.2.1 Lowering the power consumption

Being able to operate at ultra-low power consumption would be one of the desirable properties of SOT devices. To further improve the performance of our SOT devices, lowering the power consumption is thus a direction that's worth exploring. In the Ir-enabled field-free-switching device described in Chapter 4 and 5, the power consumption can be reduced if we can find ways to improve the Ir's capability of converting the charge current into the spin current. One possible way is by introducing some impurities into Ir so that there will be more spin-orbit interactions between the electrons and heavy metal atoms, and thus leading to larger intrinsic spin Hall effect. Other research group reported that the spin Hall efficiency of Pt could be enhanced by adding other metal elements such as Al, Hf[109]or Au[110]. Similarly, we can try to mix some heavy metal elements, like Pt, Au or W, into Ir to make Ir-based alloys and use them as the spin-Hall material for our SOT device. With that being mentioned, improving the spin Hall efficiency in this way seems to be rather based on trials and errors. So it would be helpful if one can develop a numerical model to simulate the effect and provide some guidance in choosing the materials as well as determine the compositions. In addition, there has been research work predicting that the A15 structured $IrCr_3$ should exhibit giant intrinsic spin Hall effect due to its specific band structures[111]. This is another thing to investigate experimentally so as to get better spin Hall efficiency. Again, it also requires further physical understanding in the spin-Hall phenomenon and how to control the spin-orbit coupling via material engineering. It should be noted that introducing other elements into Ir can cause the degradation of the interlayer exchange coupling. Figure 9.1 shows some initial works in the study of $Ir_{(1-x)}Pt_x$, where x is the Pt concentration. It's found that the exchange

coupling field reduces significantly with only 10% Pt addition. The reduction in the exchange coupling will largely affect the performance of the field-free-switching device. Hence, one of the challenges here is to figure out how to improve the spin Hall efficiency of Ir while still maintaining sufficient interlayer exchange coupling. On the other hand, to reduce the amount of the writing current shunting into the in-plane magnetic layer, a highly resistive magnetic material will be favorable, such as a magnetic oxide.

For the Oersted-field-assisted SOT device, the power consumption can be reduced if there's a way to lower the critical field current. In the calculation of the Oersted field described in Chapter 6, we notice that the Oersted field is inverse proportional to the distance between the free layer and the field path. That means the shorter the distance, the less field current we need to apply. To reduce the distance, instead of patterning the field path on top of MTJ, we can put a predefined field path underneath the write path, as shown in Figure 9.2. Prior to the three-terminal device fabrication, we pre-pattern the field path and bury it into the substrate. In this way, the field path locate closer to the free layer and the distance between the free layer and field path can be reduced from the previous 50 nm to 6-10 nm.

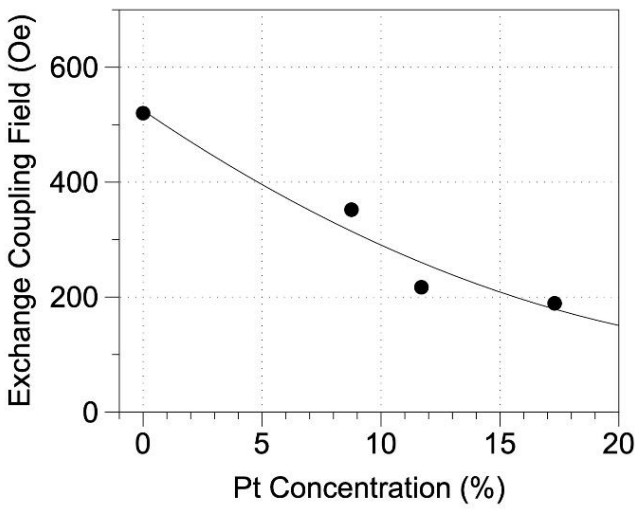

Figure 9.1 The exchange coupling field as a function of the Pt concentration in $Ir_{(1-x)}Pt_x$. The exchange coupling fields are extracted from the M-H loops of a series of films containing substrate/ Ru(2 nm)/ IrMn (5 nm)/ Co (2 nm)/ $Ir_{(1-x)}Pt_x$ (1.35nm)/ FeCoB (2 nm)/ MgO (2 nm)/ Ta (2 nm). All films are annealed at 300 ^{0}C for 10 min.

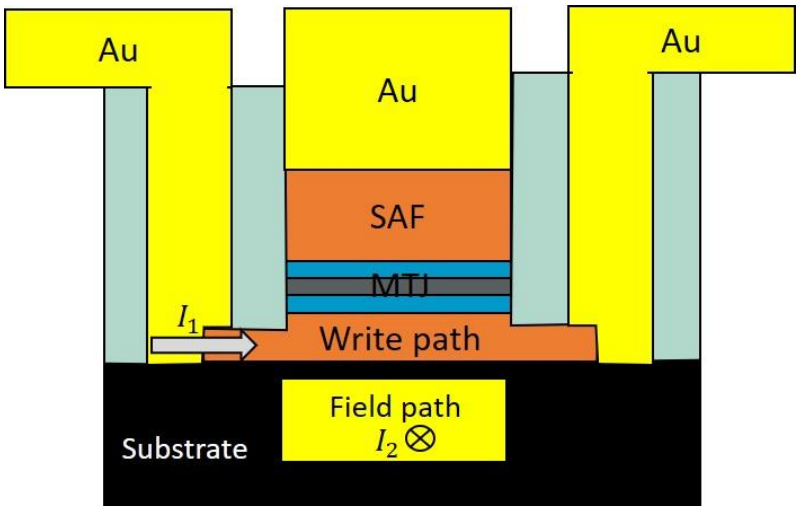

Figure 9.2 Lowering the critical field current. Here the field path is pre-patterned within the substrate and is below the write path of the device.

9.2.2 mCell development

In Chapter 8, we showed the concept and preliminary development of mCell in which the SOT driven DWM is utilized to write information. With integrating the field-free SOT switching method we've developed, the next-generation mCell will no longer limit to the DWM writing. Figure 9.3 shows the new mCell designs that are built on the Ir-enabled switching scheme as well as the Oersted-field-assisted switching scheme. Compared with the DW device, these designs are not only more scalable but also gives faster writing speed. To demonstrate the full capability of mCell, especially the logic computing functions, there are some challenges to overcome. The first is that mCell fabrication requires the ion milling to be stopped at the MgO barrier during MTJ etching. It's not an easy task because the MgO barrier is ultra-thin (0.8 nm – 1.2 nm). So one needs to do lots of careful calibrations to ensure that the etching can be controlled precisely and the process to be repeatable. It's suggested that chemical-assisted ion milling may be helpful for better controlling of the etch-stop-on-MgO[112]. The second is to improve the performance of p-MTJs. Functional mCell array requires the MTJs to have TMR > 100 % and RA < 10 $\Omega \cdot \mu m^2$. The TMR and RA properties of p-MTJs are directly related to the quality of the MgO barrier. The better quality the barrier has, the higher performance of the p-MTJs. There are many parameters that can affect the quality of the MgO barrier including the sputtering power, pressure and temperature as well as the target quality. One may do a grid search on the sputtering parameters to explore the optimal fabrication conditions. Another technique to fabricate the MgO barrier, which is widely used by industries, is to first sputter a thin MgO layer and then oxidize it. On the other hand, the low spin-polarization elements, such as Ta, can diffuse into the FeCo/ MgO interface during annealing, which significantly degrades the MTJ performance. To avoid this issue, less diffusive elements, like W or Mo, can be used as the buffer layer and capping layer materials for the p-MTJ.

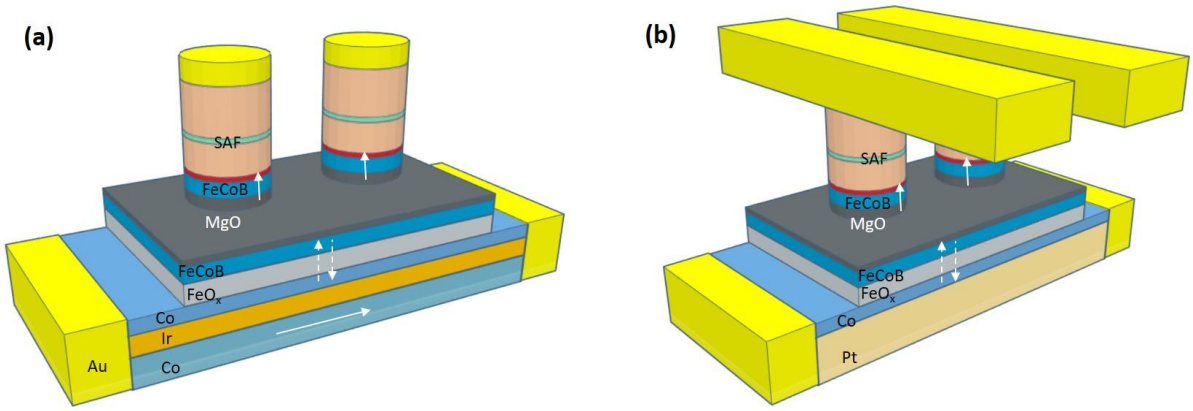

Figure 9.3 mCell design with the developed field-free switching schemes. (a) Ir-enabled fied-free switching. (b) Field-free switching assisted by the Oersted field.

9.2.3 Engineering the spin current

Recently people have reported research works in which they manipulate the spin current so that the spin polarization of the spin current can contain some perpendicular component. This can be done by introducing STTs into the SOT switching[113] or harness some novel spin transport phenomena at the interfaces[114]. The perpendicular part of the spin current turns out to be quite efficient in switching a perpendicular magnet. Although the microscopic mechanisms of those switching schemes are still vague, directly engineering the spin current is an interesting area to explore. The key here is to figure out how to tilt the spin polarization towards the perpendicular direction. In order to get the bipolar switching, the tilting direction also needs to change sign when the flow of the charge current reverses. This may be done (1) by creating some type of magnetic interface or spin polarizer so that the its interaction with the spin current alters the spin polarization, (2) or by designing novel device architectures such that the trajectory of the spin current can be controlled.

9.3 Exploring new applications

The sub-nanosecond writing capability allows the SOT devices to keep pace with today's even-faster CPU as well as to provide future potentials for novel data-intensive computing applications. Although there can still be years away from the commercial realization of the SOT devices, in this last section, we'd like to briefly discuss some intriguing applications areas where

the SOT devices can fit in. Besides the memory and storage applications, the SOT devices are also promising candidates for other advanced areas such as accelerators, sensors and neuromorphic computing.

Von-Neumann computing with separate computing and memory units will inevitably reach a bottleneck within the next decade due to long memory latency, limited memory width and huge power waste for keeping data in volatile memory. In an attempt to solve these issues, processing-in-memory (PIM) architecture has been proposed, where the logic and memory units are tightly bonded together. The coupling of computing and memory in PIM not only increases the memory width but also decreases the memory transfer latency and off-chip communication energy. With the integration with the non-volatile memory, the PIM architecture becomes even more attractive for an energy efficient information processing platform. To catch up with the fast processing speed of the current processors, the non-volatile memory with fast writing operations is needed. In this case, SOT-MRAM is a promising high-performance candidate thanks to its ultra-fast writing speed, high endurance as well as good compatibility with the CMOS fabrication technology. Thus, designing a PIM architecture with SOT-based memory would be appealing for parallel, power efficient, high-speed accelerators and information processing applications.

In recent years, deep learning has attracted tremendous attentions from both academy and industries for that it has been proven to be an extremely powerful tool in many computational tasks including computer vision, natural language processing and speech recognition. In deep learning algorithms, a hierarchical level of artificial neural networks (ANNs) is utilized to perform the learning process. The ANNs, inspired by the human brains, consists of many neuron nodes that are connected together to form a dense network. Accordingly, the concept known as the neuromorphic computing mimics the neuro-biological working methods in order to realize efficient and fast computations in ANNs. In neuromorphic computing, synaptic device with electronic analog behaviors is designed to be used as the individual neuron. In exploiting the appropriate synaptic device, spintronic devices have been proposed due to their non-volatility and low power consumption. In particular, the DW analog memristor that has multiple magnetization states controlled by DWM can potentially act as the synaptic neuron in the neuromorphic computing system. To control the magnetization states efficiently, SOTs can be utilized as the driving force for the DWM. On the other hand, multi-level device can also be obtained based on

the three-terminal SOT device. This device contains multiple p-MTJs on the write path, and the write path of this device is engineered to have a gradually increasing width. As such, the current density under each MTJ will be different. The critical current for switching the MTJ sitting on the narrow area may be not sufficient for switching the one sitting on the wider area due to the reduced current density. Hence, the amount of the writing current can be tuned to control the switching of the MTJs. By packing many MTJs on the write path, this device will exhibit nearly analogy behaviors.

The last but not least interesting field is associated with the SOT nano-oscillators. It has been shown that SOTs can effectively trigger the oscillation of a magnetic moment. The oscillation frequency is tunable by controlling the spin current. Compared to the STT oscillator, the SOT oscillator consumes less energy and allows for the individual optimization of the oscillation's amplitude and frequency. Although the SOT oscillator awaits lots of further research work, it opens new possibilities for novel applications including wireless sensing and high-frequency communication.

Reference

1 S.A. Wolf: *Science (80-.).*, 2001, vol. 294, pp. 1488–95.

2 A.D. Kent and D.C. Worledge: *Nat. Nanotechnol.*, 2015, vol. 10, pp. 187–91.

3 M.N. Baibich, J.M. Broto, A. Fert, F.N. Van Dau, F. Petroff, P. Etienne, G. Creuzet, A. Friederich, and J. Chazelas: *Phys. Rev. Lett.*, 1988, vol. 61, p. 2472.

4 G. Binasch, P. Grünberg, F. Saurenbach, and W. Zinn: *Phys. Rev. B*, 1989, vol. 39, pp. 4828–30.

5 G.A. Prinz: *Science (80-.).*, 1998, vol. 282, pp. 1660–3.

6 J.L. Leal and M.H. Kryder: *J. Appl. Phys.*, 1998, vol. 83, pp. 3720–3.

7 B. Dieny: *J. Magn. Magn. Mater.*, 1994, vol. 136, pp. 335–59.

8 D. Wang, C. Nordman, J.M. Daughton, Z. Qian, J. Fink, D. Wang, C. Nordman, J.M. Daughton, Z. Qian, and J. Fink: *IEEE Trans. Magn.*, 2004, vol. 40, pp. 2269–71.

9 S. Ikeda, J. Hayakawa, Y. Ashizawa, Y.M. Lee, K. Miura, H. Hasegawa, M. Tsunoda, F. Matsukura, and H. Ohno: *Appl. Phys. Lett.*, 2008, vol. 93, p. 82508.

10 J.-G. (Jimmy) Zhu and C. Park: *Mater. Today*, 2006, vol. 9, pp. 36–45.

11 S. Bhatti, R. Sbiaa, A. Hirohata, H. Ohno, S. Fukami, and S.N. Piramanayagam: *Mater. Today*, 2017, vol. 20, pp. 530–48.

12 A. Chen: *Solid. State. Electron.*, 2016, vol. 125, pp. 25–38.

13 M. Durlam, D. Addie, J. Akerman, B. Butcher, P. Brown, J. Chan, M. DeHerrera, B.N. Engel, B. Feil, G. Grynkewich, J. Janesky, M. Johnson, K. Kyler, J. Molla, J. Martin, K. Nagel, J. Ren, N.D. Rizzo, T. Rodriguez, L. Savtchenko, J. Salter, J.M. Slaughter, K. Smith, J.J. Sun, M. Lien, K. Papworth, P. Shah, W. Qin, R. Williams, L. Wise, and S. Tehrani: in *IEEE International Electron Devices Meeting 2003*, IEEE, 2003, pp. 34.6.1-34.6.3.

14 I.L. Prejbeanu, M. Kerekes, R.C. Sousa, H. Sibuet, O. Redon, B. Dieny, and J.P. Nozières: *J. Phys. Condens. Matter*, 2007, vol. 19, p. 165218.

15 L. Berger: *Phys. Rev. B*, 1996, vol. 54, pp. 9353–8.

16 J. Slonczewski: *J. Magn. Magn. Mater.*, 1996, vol. 159, pp. L1–7.

17 J.A. Katine, F.J. Albert, R.A. Buhrman, E.B. Myers, and D.C. Ralph: *Phys. Rev. Lett.*, 2000, vol. 84, pp. 3149–52.

18 L. Liu, O.J. Lee, T.J. Gudmundsen, D.C. Ralph, and R.A. Buhrman: *Phys. Rev. Lett.*, 2012, vol. 109, p. 096602.

19 L. Liu, C.-F. Pai, Y. Li, H.W. Tseng, D.C. Ralph, and R.A. Buhrman: *Science (80-.).*, 2012, vol. 336, pp. 555–8.

20 C.-F. Pai, L. Liu, Y. Li, H.W. Tseng, D.C. Ralph, and R.A. Buhrman: *Appl. Phys. Lett.*, 2012, vol. 101, p. 122404.

21 A. Van Den Brink, G. Vermijs, A. Solignac, J. Koo, J.T. Kohlhepp, H.J.M.M. Swagten, and B. Koopmans: *Nat. Commun.*, 2016, vol. 7, p. 10854.

22 Y.-W.W. Oh, S. Chris Baek, Y.M. Kim, H.-W.H.Y.H.W. Lee, K.-S.K.-D.D.K.S.K.-J.J. Lee, C.-G.G. Yang, E.-S.S. Park, K.-S.K.-D.D.K.S.K.-J.J. Lee, K.-W.W. Kim, G. Go, J.-R.R. Jeong, B.-C.C. Min, H.-W.H.Y.H.W. Lee, K.-S.K.-D.D.K.S.K.-J.J. Lee, B.-G.G. Park, S.H.C. Baek, Y.M. Kim, H.-W.H.Y.H.W. Lee, K.-S.K.-D.D.K.S.K.-J.J. Lee, C.-G.G. Yang, E.-S.S. Park, K.-S.K.-D.D.K.S.K.-J.J. Lee, K.-W.W. Kim, G. Go, J.-R.R. Jeong, B.-C.C. Min, H.-W.H.Y.H.W. Lee, K.-S.K.-D.D.K.S.K.-J.J. Lee, and B.-G.G. Park: *Nat. Nanotechnol.*, 2016, vol. 11, pp. 878–84.

23 S. Fukami, C. Zhang, S. DuttaGupta, A. Kurenkov, and H. Ohno: *Nat. Mater.*, 2016, vol. 15, pp. 535–41.

24 L. Liu, A. Richardella, I. Garate, Y. Zhu, N. Samarth, and C.-T. Chen: *Phys. Rev. B*, 2015, vol. 91, p. 235437.

25 M. DC, R. Grassi, J.-Y. Chen, M. Jamali, D. Reifsnyder Hickey, D. Zhang, Z. Zhao, H. Li, P. Quarterman, Y. Lv, M. Li, A. Manchon, K.A. Mkhoyan, T. Low, and J.-P. Wang: *Nat. Mater.*, 2018, vol. 17, pp. 800–7.

26 N.H.D. Khang, Y. Ueda, and P.N. Hai: *Nat. Mater.*, 2018, vol. 17, pp. 808–13.

27 J. Sinova, S.O. Valenzuela, J. Wunderlich, C.H. Back, and T. Jungwirth: *Rev. Mod. Phys.*,

2015, vol. 87, pp. 1213–60.

28 S.D. Stranks and P. Plochocka: *Nat. Mater.*, 2018, vol. 17, pp. 381–2.

29 J. Sinova and T. Jungwirth: *Phys. Today*, 2017, vol. 70, pp. 38–42.

30 D.C. Ralph and M.D. Stiles: *J. Magn. Magn. Mater.*, 2008, vol. 320, pp. 1190–216.

31 S. Fukami, T. Anekawa, C. Zhang, and H. Ohno: *Nat. Nanotechnol.*, 2016, vol. 11, pp. 621–5.

32 K. Garello, C.O. Avci, I.M. Miron, M. Baumgartner, A. Ghosh, S. Auffret, O. Boulle, G. Gaudin, and P. Gambardella: *Appl. Phys. Lett.*, 2014, vol. 105, p. 212402.

33 M. Cubukcu, O. Boulle, N. Mikuszeit, C. Hamelin, T. Bracher, N. Lamard, M.-C. Cyrille, L. Buda-Prejbeanu, K. Garello, I.M. Miron, O. Klein, G. de Loubens, V. V. Naletov, J. Langer, B. Ocker, P. Gambardella, and G. Gaudin: *IEEE Trans. Magn.*, 2018, vol. 54, pp. 1–4.

34 J.M.D. Coey: *Magnetism and Magnetic Materials*, Cambridge university press, 2010.

35 P. Gambardella and I.M. Miron: *Philos. Trans. R. Soc. A Math. Phys. Eng. Sci.*, 2011, vol. 369, pp. 3175–97.

36 M. Heide, G. Bihlmayer, and S. Blügel: *Phys. Rev. B*, 2008, vol. 78, p. 140403.

37 W. Zhang, M.B. Jungfleisch, W. Jiang, J.E. Pearson, A. Hoffmann, F. Freimuth, and Y. Mokrousov: *Phys. Rev. Lett.*, 2014, vol. 113, p. 196602.

38 S. Murakami and N. Nagaosa: in *Comprehensive Semiconductor Science and Technology*, vol. 1–6, Elsevier, 2011, pp. 222–78.

39 G. Vignale: *J. Supercond. Nov. Magn.*, 2010, vol. 23, pp. 3–10.

40 G.Y. Guo, S. Murakami, T.-W. Chen, and N. Nagaosa: *Phys. Rev. Lett.*, 2008, vol. 100, p. 096401.

41 A. Manchon, H.C. Koo, J. Nitta, S.M. Frolov, and R.A. Duine: *Nat. Mater.*, 2015, vol. 14, pp. 871–82.

42 H.B.M. Saidaoui and A. Manchon: *Phys. Rev. Lett.*, 2016, vol. 117, p. 036601.

43 S.C. Baek, V.P. Amin, Y.-W. Oh, G. Go, S.-J. Lee, G.-H. Lee, K.-J. Kim, M.D. Stiles, B.-

G. Park, and K.-J. Lee: *Nat. Mater.*, 2018, vol. 17, pp. 509–13.

44 P.M. Haney, H.-W.W. Lee, K.-J.J. Lee, A. Manchon, and M.D. Stiles: *Phys. Rev. B*, 2013, vol. 87, pp. 1–13.

45 A. Chernyshov, M. Overby, X. Liu, J.K. Furdyna, Y. Lyanda-Geller, and L.P. Rokhinson: *Nat. Phys.*, 2009, vol. 5, p. 656.

46 K.-S.S.K.-J.J. Lee, S.-W.W. Lee, B.-C.C. Min, and K.-S.S.K.-J.J. Lee: *Appl. Phys. Lett.*, 2013, vol. 102, p. 112410.

47 M. Cubukcu, O. Boulle, N. Mikuszeit, and C. Hamelin: *Spintec*, 2015, pp. 1–23.

48 S. Shi, Y. Ou, S. V. Aradhya, D.C. Ralph, and R.A. Buhrman: *Phys. Rev. Appl.*, 2018, vol. 9, p. 011002.

49 S. Ikeda, K. Miura, H. Yamamoto, K. Mizunuma, H.D. Gan, M. Endo, S. Kanai, J. Hayakawa, F. Matsukura, and H. Ohno: *Nat. Mater.*, 2010, vol. 9, pp. 721–4.

50 M. Yoshikawa, E. Kitagawa, T. Nagase, T. Daibou, M. Nagamine, K. Nishiyama, T. Kishi, and H. Yoda: *IEEE Trans. Magn.*, 2008, vol. 44, pp. 2573–6.

51 C. Park, J.J. Kan, C. Ching, J. Ahn, L. Xue, R. Wang, A. Kontos, S. Liang, M. Bangar, H. Chen, S. Hassan, M. Gottwald, X. Zhu, M. Pakala, and S.H. Kang: in *2015 IEEE International Electron Devices Meeting (IEDM)*, vol. 2016-Febru, IEEE, 2015, pp. 26.2.1-26.2.4.

52 G. Yu, P. Upadhyaya, Y. Fan, J.G. Alzate, W. Jiang, K.L. Wong, S. Takei, S.A. Bender, L. Chang, Y. Jiang, M. Lang, J. Tang, Y. Wang, Y. Tserkovnyak, P.K. Amiri, and K.L. Wang: DOI:10.1038/nnano.2014.94.

53 L. You, O. Lee, D. Bhowmik, D. Labanowski, J. Hong, J. Bokor, and S. Salahuddin: *Proc. Natl. Acad. Sci.*, 2015, vol. 112, pp. 10310–5.

54 Y.-C. Lau, D. Betto, K. Rode, J.M.D. Coey, and P. Stamenov: *Nat. Nanotechnol.*, 2016, vol. 11, pp. 758–62.

55 K.-S. Ryu, L. Thomas, S.-H. Yang, and S. Parkin: *Nat. Nanotechnol.*, 2013, vol. 8, pp. 527–33.

56 K.-S. Ryu, S.-H. Yang, L. Thomas, and S.S.P. Parkin: *Nat. Commun.*, 2014, vol. 5, p. 3910.

57 J. Torrejon, J. Kim, J. Sinha, S. Mitani, M. Hayashi, M. Yamanouchi, and H. Ohno: *Nat. Commun.*, 2014, vol. 5, p. 4655.

58 S. Emori, U. Bauer, S.-M. Ahn, E. Martinez, and G.S.D. Beach: *Nat. Mater.*, 2013, vol. 12, pp. 611–6.

59 Y. Liu, X. Liu, and J.-G. Zhu: *IEEE Trans. Magn.*, 2018, vol. 54, pp. 1–5.

60 I.M. Miron, T. Moore, H. Szambolics, L.D. Buda-Prejbeanu, S. Auffret, B. Rodmacq, S. Pizzini, J. Vogel, M. Bonfim, A. Schuhl, and G. Gaudin: *Nat. Mater.*, 2011, vol. 10, pp. 419–23.

61 X. Fong, Y. Kim, K. Yogendra, D. Fan, A. Sengupta, A. Raghunathan, and K. Roy: *IEEE Trans. Comput. Des. Integr. Circuits Syst.*, 2016, vol. 35, pp. 1–22.

62 D. Bhowmik, U. Saxena, A. Dankar, A. Verma, D. Kaushik, S. Chatterjee, and U. Singh: *J. Magn. Magn. Mater.*, 2019, vol. 489, p. 165434.

63 K. Yue, Y. Liu, R.K. Lake, and A.C. Parker: *Sci. Adv.*, 2019, vol. 5, p. eaau8170.

64 M. Cubukcu, O. Boulle, M. Drouard, K. Garello, C. Onur Avci, I. Mihai Miron, J. Langer, B. Ocker, P. Gambardella, and G. Gaudin: *Appl. Phys. Lett.*, 2014, vol. 104, p. 042406.

65 K. Kim, J. Seo, E. Lee, K.-T. Ko, B.S. Kim, B.G. Jang, J.M. Ok, J. Lee, Y.J. Jo, W. Kang, J.H. Shim, C. Kim, H.W. Yeom, B. Il Min, B.-J. Yang, and J.S. Kim: *Nat. Mater.*, 2018, vol. 17, pp. 794–9.

66 F. Oboril, R. Bishnoi, M. Ebrahimi, and M.B. Tahoori: *IEEE Trans. Comput. Des. Integr. Circuits Syst.*, 2015, vol. 34, pp. 367–80.

67 S. Parkin and S.-H. Yang: *Nat. Nanotechnol.*, 2015, vol. 10, pp. 195–8.

68 S.-H. Yang, K.-S. Ryu, and S. Parkin: *Nat. Nanotechnol.*, 2015, vol. 10, pp. 221–6.

69 D.M. Bromberg, H.E. Sumbul, J.-G. Zhu, and L. Pileggi: *J. Appl. Phys.*, 2015, vol. 117, p. 17B510.

70 D.M. Bromberg, M.T. Moneck, V.M. Sokalski, J. Zhu, L. Pileggi, and J.-G. Zhu: in *2014 IEEE International Electron Devices Meeting*, vol. 2015-Febru, IEEE, 2014, pp. 33.1.1-

33.1.4.

71 A. Manchon, J. Železný, I.M. Miron, T. Jungwirth, J. Sinova, A. Thiaville, K. Garello, and P. Gambardella: *Rev. Mod. Phys.*, 2019, vol. 91, p. 035004.

72 W. Zhang, M.B. Jungfleisch, W. Jiang, J. Sklenar, F.Y. Fradin, J.E. Pearson, J.B. Ketterson, and A. Hoffmann: *J. Appl. Phys.*, 2015, vol. 117, p. 172610.

73 Y. Niimi, M. Morota, D.H. Wei, C. Deranlot, M. Basletic, A. Hamzic, A. Fert, and Y. Otani: *Phys. Rev. Lett.*, 2011, vol. 106, p. 126601.

74 M. Yamanouchi, L. Chen, J. Kim, M. Hayashi, H. Sato, S. Fukami, S. Ikeda, F. Matsukura, and H. Ohno: *Appl. Phys. Lett.*, 2013, vol. 102, p. 212408.

75 J. Zhou, H. Zhou, A. Bournel, and W. Zhao: *Sci. China Physics, Mech. Astron.*, 2020, vol. 63, p. 217511.

76 P.P.J. Haazen, E. Murè, J.H. Franken, R. Lavrijsen, H.J.M. Swagten, and B. Koopmans: *Nat. Mater.*, 2013, vol. 12, pp. 299–303.

77 Y. Liu, M. Furuta, and J.-G. (Jimmy) Zhu: *AIP Adv.*, 2018, vol. 8, p. 056306.

78 W. Zhang, V. Vlaminck, J. Pearson, R. Divan, S. Bader, and A. Hoffmann: in *APS March Meeting Abstracts*, 2014.

79 W. Chen, L. Qian, and G. Xiao: *AIP Adv.*, 2018, vol. 8, p. 055918.

80 Z. Zhao, A.K. Smith, M. Jamali, and J. Wang: *arXiv Prepr. arXiv1603.09624*.

81 S. Yuasa and D.D. Djayaprawira: *J. Phys. D. Appl. Phys.*, 2007, vol. 40, pp. R337–54.

82 T. Miyazaki, T. Yaoi, and S. Ishio: *J. Magn. Magn. Mater.*, 1991, vol. 98, pp. L7–9.

83 T. Miyazaki and N. Tezuka: *J. Magn. Magn. Mater.*, 1995, vol. 139, pp. L231–4.

84 J.S. Moodera, L.R. Kinder, T.M. Wong, and R. Meservey: *Phys. Rev. Lett.*, 1995, vol. 74, pp. 3273–6.

85 W.H. Butler, X.-G. Zhang, T.C. Schulthess, and J.M. MacLaren: *Phys. Rev. B*, 2001, vol. 63, p. 54416.

86 J. Mathon and A. Umerski: *Phys. Rev. B*, 2001, vol. 63, p. 220403.

87 S.S.P. Parkin, C. Kaiser, A. Panchula, P.M. Rice, B. Hughes, M. Samant, and S.-H. Yang: *Nat. Mater.*, 2004, vol. 3, pp. 862–7.

88 S. Yuasa, T. Nagahama, A. Fukushima, Y. Suzuki, and K. Ando: *Nat. Mater.*, 2004, vol. 3, pp. 868–71.

89 S. Ikeda, K. Miura, H. Yamamoto, K. Mizunuma, H.D. Gan, M. Endo, S. Kanai, J. Hayakawa, F. Matsukura, and H. Ohno: *Nat. Mater.*, 2010, vol. 9, pp. 721–4.

90 S. Ikeda, H. Sato, H. Honjo, E.C.I. Enobio, S. Ishikawa, M. Yamanouchi, S. Fukami, S. Kanai, F. Matsukura, T. Endoh, and H. Ohno: *Tech. Dig. - Int. Electron Devices Meet. IEDM*, 2015, vol. 2015-Febru, pp. 33.2.1-33.2.4.

91 Y.W. Oh, K.D. Lee, J.R. Jeong, and B.G. Park: *J. Appl. Phys.*, 2014, vol. 115, pp. 2014–7.

92 S. Peng, M. Wang, H. Yang, L. Zeng, J. Nan, J. Zhou, Y. Zhang, A. Hallal, M. Chshiev, K.L. Wang, Q. Zhang, and W. Zhao: *Sci. Rep.*, 2015, vol. 5, p. 18173.

93 S. V. Karthik, Y.K. Takahashi, T. Ohkubo, K. Hono, H.D. Gan, S. Ikeda, and H. Ohno: *J. Appl. Phys.*, 2012, vol. 111, p. 083922.

94 H. Sato, S. Ikeda, S. Fukami, H. Honjo, and S. Ishikawa: *Jpn. J. Appl. Phys.*, 2014, vol. 53, p. 04EM02.

95 H. Sato, S. Ikeda, S. Fukami, H. Honjo, S. Ishikawa, M. Yamanouchi, K. Mizunuma, F. Matsukura, and H. Ohno: *Jpn. J. Appl. Phys.*, 2014, vol. 53, p. 04EM02.

96 Y.-J. Chang, A. Canizo-Cabrera, V. Garcia-Vazquez, Y.-H. Chang, and T. Wu: *J. Appl. Phys.*, 2013, vol. 113, p. 17B909.

97 K. Yakushiji, H. Kubota, A. Fukushima, and S. Yuasa: *Appl. Phys. Express*, 2015, vol. 8, p. 083003.

98 H. Okamoto, L. Kacprzak, and P.R. Subramanian: *Binary Alloy Phase Diagrams*, ASM international Materials Park, OH, 1996.

99 Y. Huai, J. Zhang, G.W. Anderson, P. Rana, S. Funada, C.-Y. Hung, M. Zhao, and S. Tran: *J. Appl. Phys.*, 1999, vol. 85, pp. 5528–30.

100 W. Skowroński, T. Nozaki, Y. Shiota, S. Tamaru, K. Yakushiji, H. Kubota, A. Fukushima,

S. Yuasa, and Y. Suzuki: *Appl. Phys. Express*, 2015, vol. 8, p. 053003.

101 K.-M. Lee, J.W. Choi, J. Sok, and B.-C. Min: *AIP Adv.*, 2017, vol. 7, p. 065107.

102 Jian-Gang Zhu: *Proc. IEEE*, 2008, vol. 96, pp. 1786–98.

103 W. Zhang, V. Vlaminck, J.E. Pearson, R. Divan, S.D. Bader, and A. Hoffmann: *Appl. Phys. Lett.*, 2013, vol. 103, p. 242414.

104 Q. Hao and G. Xiao: *Phys. Rev. Appl.*, 2015, vol. 3, p. 034009.

105 J.-S. Lee, J. Cho, and C.-Y. You: *J. Vac. Sci. Technol. A Vacuum, Surfaces, Film.*, 2016, vol. 34, p. 021502.

106 L. You, R.C. Sousa, S. Bandiera, B. Rodmacq, and B. Dieny: *Appl. Phys. Lett.*, 2012, vol. 100, p. 172411.

107 J.G. Simmons: *J. Appl. Phys.*, 1963, vol. 34, pp. 1793–803.

108 B. Zhou, B.S.D.C.S. Varaprasad, Z. Dai, D.E. Laughlin, and J.-G. Zhu: *Appl. Phys. Lett.*, 2018, vol. 113, p. 082401.

109 M.H. Nguyen, M. Zhao, D.C. Ralph, and R.A. Buhrman: *Appl. Phys. Lett.*, 2016, vol. 108, p. 242407.

110 L. Zhu, D.C. Ralph, and R.A. Buhrman: *Phys. Rev. Appl.*, 2018, vol. 10, p. 1.

111 E. Derunova, Y. Sun, C. Felser, S.S.P. Parkin, B. Yan, and M.N. Ali: *Sci. Adv.*, 2019, vol. 5, pp. 1–8.

112 S.Z. Rahaman, I.-J. Wang, T.-Y. Chen, C.-F. Pai, D.-Y. Wang, J.-H. Wei, H.-H. Lee, Y.-C. Hsin, Y.-J. Chang, S.-Y. Yang, Y.-C. Kuo, Y.-H. Su, Y.-S. Chen, K.-C. Huang, C.-I. Wu, and D.-L. Deng: *IEEE Electron Device Lett.*, 2018, vol. 39, pp. 1306–9.

113 M. Wang, W. Cai, D. Zhu, Z. Wang, J. Kan, Z. Zhao, K. Cao, Z. Wang, Y. Zhang, and T. Zhang: *Nat. Electron.*, 2018, vol. 1, p. 582.

114 S.H.C. Baek, V.P. Amin, Y.W. Oh, G. Go, S.J. Lee, G.H. Lee, K.J. Kim, M.D. Stiles, B.G. Park, and K.J. Lee: *Nat. Mater.*, 2018, vol. 17, pp. 509–13.